Magnetism and superconductivity in iron pnictides and iron chalcogenides

by

Jack Wright

Worcester College

A thesis submitted for the
degree of Doctor of Philosophy
at the
University of Oxford

Trinity Term 2013

Declaration of Authorship

I, Jack Wright, declare that this thesis, titled ‘Magnetism and superconductivity in iron pnictides and iron chalcogenides’, and the work presented in it are my own. I confirm that:

- This work was done wholly while in candidature for a research degree at this University.
- Where I have consulted the published work of others, this is always clearly attributed.
- Where I have quoted from the work of others, the source is always given. With the exception of such quotations, this thesis is entirely my own work.
- I have acknowledged all main sources of help.
- Where the thesis is based on work done by myself jointly with others, I have made clear exactly what was done by others and what I have contributed myself.

Signed:

Date:

Magnetism and superconductivity in iron pnictides and iron chalcogenides

Jack Wright, Worcester College, Trinity Term 2013

Abstract of Thesis submitted for the degree of Doctor of Philosophy

This thesis presents a study on several series of unconventional Fe-based superconductors; namely, derivatives of NaFeAs and LiFeAs, as well as molecular-intercalated FeSe. Primarily using muon spin rotation (μSR), but also x-ray diffraction (XRD) and magnetic susceptibility measurements, the nature of both magnetic and superconducting phases within these systems is studied. Particular attention is focussed on how these states compete or coexist with one another.

The aforementioned experimental techniques are first used to explore the phase diagram of $\mathrm{NaFe}_{1-x}\mathrm{Co}_x\mathrm{As}$. This phase diagram includes regions of long-range antiferromagnetism and short-range order, that both coexist with superconductivity. Magnetism is gradually destroyed, primarily through a diminishment of the size of the ordered moment, as superconductivity is enhanced by Co substitution. This interplay is explored in detail. By contrast, superconductivity in LiFeAs cannot be enhanced by transition metal substitution, suggesting that it is intrinsically optimally-doped. I investigate this conclusion by studying the evolution of the penetration depth in superconducting compositions of $\mathrm{LiFe}_{1-x}\mathrm{Co}_x\mathrm{As}$ and $\mathrm{LiFe}_{1-x}\mathrm{Ni}_x\mathrm{As}$, and comparing these data to those from other electron-doped systems. I also study an unusual and emergent magnetic phase in $\mathrm{Li}_{1-y}\mathrm{Fe}_{1+y}\mathrm{As}$. This work suggests that LiFeAs supports a superconducting phase that resembles those in other Fe-pnictides, but is uniquely close to an additional magnetic instability.

I then move on to the study of a recently discovered series, based on FeSe intercalated with ammonia and various metals. I study both the penetration depth and the intrinsic magnetic phases in these systems using μSR and compare them with other compounds based on FeSe. I find that these intercalated systems support spacially separated regions of dynamic magnetism and superconductivity and I discuss how much these phases depend on the precise chemical details of the intercalated layer. Finally, I return to the experimental study of $\mathrm{NaFe}_{1-x}\mathrm{Co}_x\mathrm{As}$, extending the range of techniques employed by using high-field magnetometry and high-pressure μSR. These studies reveal new features of this system that were not accessible using low-field and ambient-pressure methods. In particular, I show that the magnetic moment size in NaFeAs unexpectedly increases with pressure, suggesting that the electronic structure of this compound may be unique amongst known Fe-based superconductors.

Acknowledgements

I would not have been able to carry out the work presented here without the help and support of others. Firstly, thanks must go to my supervisors, Stephen Blundell and Simon Clarke, who both provided me with a fantastic working environment in the Oxford Physics and Chemistry departments respectively. Their patience, insight and willingness to teach me things I really should have already known will not be forgotten. To this end, I must also thank Tom Lancaster and Dinah Parker, who also acted as outstanding mentors, especially in the early days of this project.

I must also acknowledge my experimental collaborators. All of the instrument scientists I have worked with provided not only great technical assistance, but were also quite willing to share and discuss interpretations of data; I found this invaluable. In particular, I thank Peter Baker, Francis Pratt and Rustem Khasanov for this help.

Aside from their immeasurable professional support, all those mentioned above were friendly and personable throughout my project, making these last four years a highly enjoyable time. Likewise, for their willingness to help me with science but also, where necessary, to talk about anything else I thank the following:

- Isabel Franke, Andrew Steele, Johannes Möeller, Francesca Foronda and Rob Williams, who all made muon experiments far more fun than they would have otherwise been.
- Sungkyun Choi, Alun Biffin, Danielle Kaminsky and David Keen, for making Room 106 the incredible office space it is.
- Alex Corkett, Michael Pitcher, David Free, Stefan Sedlmaier and Simon Cassidy for making S16 the just-as-incredible office space that it is.
- The too-numerous-to-mention members of the Correlated Electron Systems group in the Clarendon Laboratory, who always provided tea-time company, amusing conversation and, in the case of Bill Hayes in particular, first class anecdotes.

Finally, I thank my family and friends and particularly Ruth, whose extreme patience and encouragement was a constant source of inspiration throughout this work.

Contents

List of Figures

List of Tables

For my parents.

Chapter 1

Introduction

It is now over 100 years since Heike Kamerlingh Onnes' original discovery of a state of zero electrical resistance in mercury below 4.19 K, and yet superconductivity remains one of the most mysterious, surprising and intensely studied phenomena in condensed matter physics. There is no escaping the fact that, though the last century has seen huge advances in the application of superconductivity to various technologies, a theoretical consensus on the microscopic interactions that govern this state in many superconducting materials remains as elusive as ever.

At one time, many physicists had believed the problem to be solved. Fritz London had shown [33] in 1935 that the Meissner effect[1], the second unique feature of a superconductor besides zero resistance, was a manifestation of a macroscopic quantum state. Bardeen, Cooper and Shrieffer (BCS) had then demonstrated in 1957 [35] that such a state could emerge through the condensation of bosonic pairs of electrons (Cooper pairs), glued together by their mutual interactions with the lattice. The BCS theory explained

---

[1] This is the expulsion and exclusion of applied magnetic fields below T_c, first observed in 1933 [34].

almost every feature of superconducting materials known at that time, hence the conclusion that this phenomenon was fully accounted for. However, the phonon coupling scheme led to a prediction that superconductivity was impossible above around 30 K, so the discovery of "Possible high-T_c superconductivity in the Ba-La-Cu-O system" in 1986 [36] shattered this conclusion. To date, the highest recorded transition temperature in any superconductor at ambient pressure is the $T_c = 133\,\mathrm{K}$ achieved by the cuprate $\mathrm{HgBa_2Ca_2Cu_3O_8}$ [37], and it is such "unconventional superconductors" that remain so poorly understood.

An important feature of unconventional superconductors, aside from their frequently high values of T_c, is their almost ubiquitous proximity to a magnetic phase. For example, the parent compound $\mathrm{La_2CuO_4}$ is an antiferromagnet below $T_N \simeq 300\,\mathrm{K}$, but substituting a few percent of La for Ce or Sr results in the suppression of T_N and the promotion of superconductivity [38]. This is in crucial contrast to the predictions of BCS theory, in which electrons pair up in singlet states that can be destroyed in the presence of strong magnetic interactions. A similar proximity of superconducting and magnetic phases has been observed in the heavy fermion compounds [39] and the Fe-based systems that are discussed in this thesis.

Following these observations, many have suggested that magnetic interactions may form the basis of the pairing mechanism in unconventional superconductors (see Reference [40] for a recent review). At the time of writing, the exact pairing mechanism is not confirmed, but one could imagine that electrons can be glued together through mutual interactions with spin excitations, just as they can be through lattice excitations in conventional superconductors[2]. Motivated by this idea, much experimental and theoretical

---

[2] That is, those that satisfy the predictions of BCS theory.

work is devoted to understanding the nature of these magnetic and superconducting phases, both in isolation and at points of crossover on the phase diagram.

Throughout this project, I have followed this path and analysed these phases in three series of Fe-based superconductors; based on NaFeAs, LiFeAs and ammonia-intercalated FeSe. In general, a magnetic phase can be characterised by its structure, the extent and onset temperature of any order, the presence of dynamic fluctuations and any relevant moment sizes. Superconducting states are described in terms of their volume fraction, values of the penetration depth and coherence length and, again, the transition temperature. The aim of this project was to study these properties in my three series, providing a detailed data set on which a theoretical understanding of these materials may be based.

To begin this thesis, I present a more detailed introduction to Fe-based superconductivity in Chapter 2. Common features of the structures and phase diagrams of these systems are highlighted, as well as details of the most widely accepted theoretical model for them. The electronic structure and Fermi surface turn out to be of significant importance, and this chapter provides the basis for interpreting my results in these terms. Following this, I present a description of the techniques behind the synthesis and study of my three systems. My discussion of the preparation of samples is quite general in Chapter 3, and I give more specific details about the synthesis of these compounds in relevant subsequent chapters. The main technique used to study the physics of these systems is muon spin rotation (μSR) which, as I demonstrate, can probe both magnetic and superconducting states and so is an ideal tool with which to analyse their interplay. In Chapter 4, I discuss my work on establishing the phase diagram of $\mathrm{NaFe}_{1-x}\mathrm{Co}_x\mathrm{As}$ using μSR and complimentary techniques. Co substitution is shown to provide a means of smoothly driving the system from a fully magnetic to a fully superconducting phase, with an interesting region of coexistance in between. Chapter 5 describes contrasting results in derivatives of LiFeAs, which demonstrate no magnetically ordered phase but an unusual and emergent spin-frozen state. In addition, I also demonstrate how studying the penetration depth using μSR reveals a great deal about the electronic structure of LiFeAs and, by extension, Fe-based superconductors in general.

Motivated by this, I have performed similar experiments on a range of FeSe samples which have been intercalated with ammonia and various Group I and Group II metals. These systems were only discovered in the last year and have already attracted great interest due to their impressive transition temperatures ($\simeq$ 40 K). As these samples may never be prepared in single crystal form, for reasons I explain, a direct analysis of the electronic structure will be difficult to perform. This makes the results from μSR, which provide an indirect probe of the Fermi surface, even more important and I describe them in Chapter 6. Finally, I return to the NaFeAs system in Chapter 7, where I describe experiments designed to probe magnetic and superconducting phases in the Co-doped series deeper still by utilising high magnetic field magnetometry and high-pressure μSR. These experiments compliment those described in Chapter 4 and reveal information about the Fermi surface of NaFeAs that is inaccessible to ambient pressure and low-field techniques. Each chapter ends with a discussion of how the presented results fit into the field at large and I summarise these conclusions in Chapter 8.

Chapter 2

Iron-based superconductors

This chapter outlines the common structural, magnetic, superconducting and electronic properties of Fe-based superconductors. I draw particular attention to the Fermi surfaces of these systems, as it appears that the topology of the Fermi surface is a key ingredient for both magnetic and superconducting states and forms the basis of the most widely-accepted theoretical model for them. Subsequently, most of the results presented in this thesis are interpreted in terms of an evolving Fermi surface. The content of this chapter is discussed in more detail in References [2, 26, 41, 42].

2.1 Structural features

All of the most well-characterised Fe-based superconductors share a common structural motif: The Fe atoms sit at the center of tetrahedra formed by four pnictogen (As, P) or chalcogen (Se, Te) atoms, and these edge-sharing tetrahedra comprise FeX layers that may be separated by various other species. The simplest case is that of FeSe, which actually contains no spacer layer and whose structure is shown in Fig. 6.1.

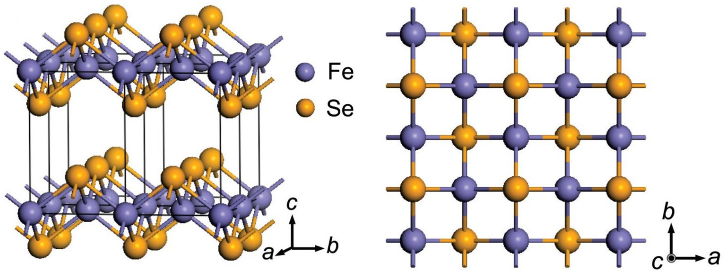

FIGURE 2.1: The structure of (tetragonal, superconducting) FeSe, taken from Reference [1].

It is common to group the Fe-based superconductors into families that are defined by the stoichiometry of the spacer layer relative to the FeX layer. There are three principle families (along with the so-called "11" family that contains only FeSe and FeTe), and they are

- The **111** family, containing (Li, Na)FeAs.
- The **122** family, containing (Ca, Sr, Ba, Eu, K)Fe_2As_2.
- The **1111** family, containing (La, Ce, Pr, Nd)OFeAs.

For clarity, I have only listed the so-called "parent" compounds in these families. In most cases, atoms can be partially or even fully substituted with others from nearby groups or rows in the periodic table (and indeed this is often required to induce superconductivity). Thus, there are many more compositions available in each family. There are also some more exotic families, typically containing much larger spacer layers, but they are less well-characterised and so I do not discuss them further.

Figure 2.2 shows the full structures of these families, and emphasises how similar they are to one another. At room temperature, all of the aforementioned parent compounds adopt a tetragonal symmetry; the 11, 111 and 1111 compounds crystallise into the $P4/nmm$ space group [1, 13, 43–45] while the 122s occupy $I4/nmm$ [46]. On cooling,

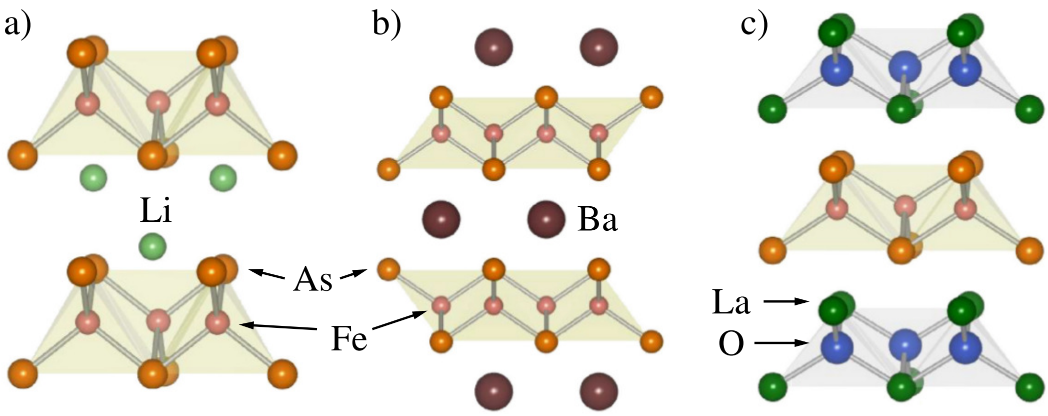

FIGURE 2.2: The structures of a) LiFeAs, b) $BaFe_2As_2$ and c) LaOFeAs. These are representative members of the 111, 122 and 1111 families respectively, and all contain similar layers of $FeAs_4$ tetrahedra. This figure is adapted from Reference [2].

most of these parent compounds undergo a structural transition to an orthorhombic space group (typically *Cmma*) at somewhere between 55 K and 200 K, depending on the compound [12, 47–49].

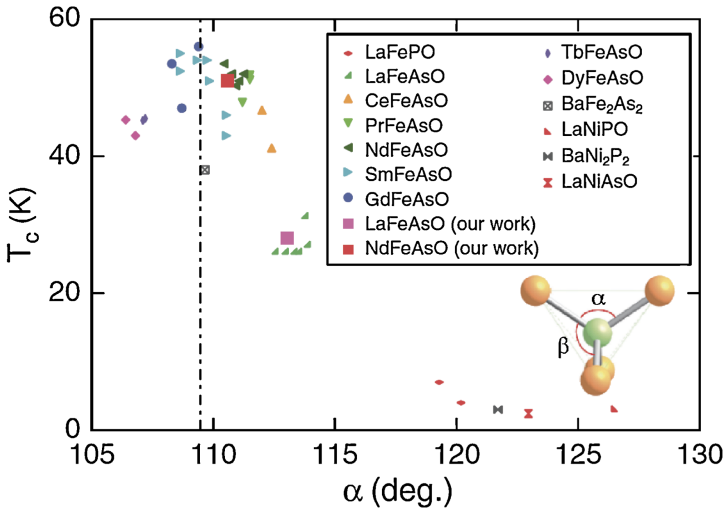

FIGURE 2.3: The correlation between T_c and the As–Fe–As bond angle within the $FeAs_4$ tetrahedra of various systems. This figure is adapted from Reference [3].

It was quickly observed that the precise geometry of the $FeAs_4$ tetrahedra appeared to have an important effect on the superconducting transition temperature, T_c, in the pnictides: T_c is maximal in compounds where the As–Fe–As bond angles are closest to the ideal tetrahedral angle value of 109.5°. This is shown in Fig. 2.3, which is adapted from Reference [3], and the implication of this correlation will be discussed shortly.

2.2 Phase diagrams

As suggested in the previous section, most of the aforementioned parent compounds are not intrinsic superconductors. Instead, they develop antiferromagnetic order on cooling, and the ordering temperature is either coincident with or just below that of the structural transition. Whether the two transitions are simultaneous or not again depends on the family; they occur at the same temperature in the 122 parent compounds [5], but are separated (typically by $\sim 10\,\mathrm{K}$) in the 1111 family [2] and in NaFeAs [13].

The concurrence of magnetic and structural transitions strongly implies that the two are intimately related, and the structure of the magnetic phase supports this conclusion: The moments (sitting on the Fe site) are always aligned in the *ab*-plane antiferromagnetically along the long basal direction and ferromagnetically along the short basal direction, suggesting that orthorhombic crystal symmetry is vital for this kind of magnetic order. The coupling in the c direction is also antiferromagnetic, as shown in Fig. 2.4. This magnetic structure is conventionally described by the propagation vector $(\pi, \pi, 2\pi)$, with respect to the tetragonal reciprocal lattice. As I perform a specific analysis of the structural transition in $\mathrm{NaFe}_{1-x}\mathrm{Co}_x\mathrm{As}$ in Chapter 4, more details on the theory describing its relationship to the magnetic transition are given there. Note that in certain 1111 compounds, moments on the rare earth site also order [2], but this is not thought to be related to any aspect of the superconducting phase and so I say no more about it.

The sizes of the ordered Fe moments in these magnetic phases is intriguing. While again they do vary from one compound to the next, they are all close to or less than $1\,\mu_{\mathrm{B}}$ per Fe

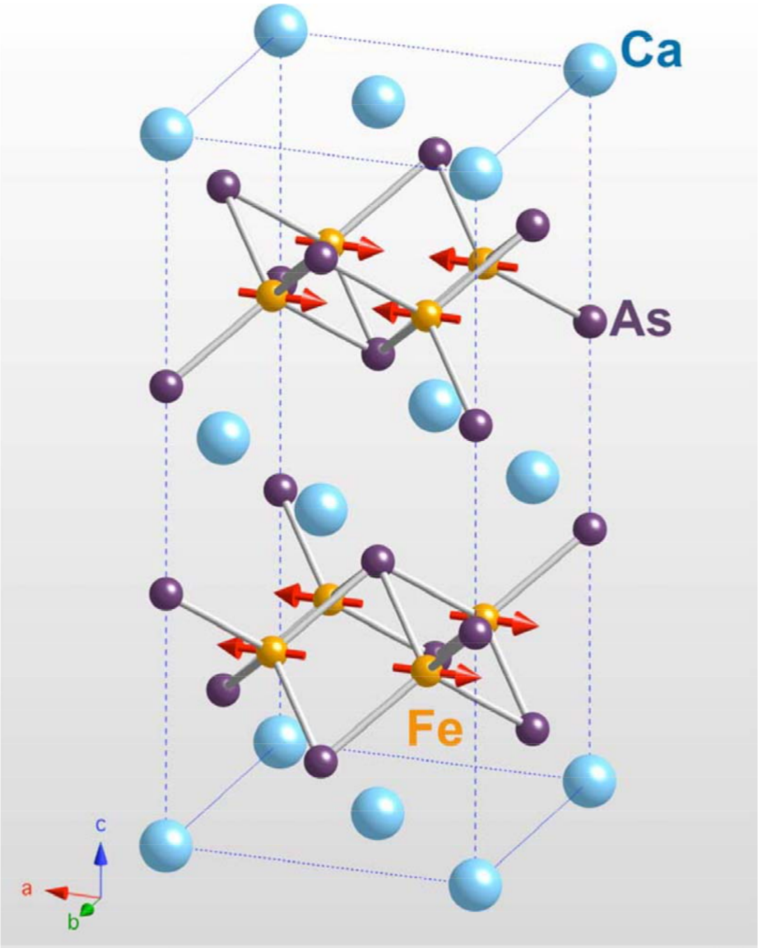

FIGURE 2.4: The magnetic structure of $CaFe_2As_2$, which is shared by most parent compounds. This structure is conventionally described by the propagation vector $(\pi, \pi, 2\pi)$, with respect to the tetragonal reciprocal lattice. The image is taken from Reference [4].

[4, 8, 50–53] and, in the case of NaFeAs, closer to $0.1\,\mu_B$ per Fe (see Chapter 4). These low and non-integer values strongly imply that the magnetism in these compounds is itinerant, and I shall discuss the probable origin of this itineracy in the next section.

For superconductivity to occur, one must tune the system away from this magnetic phase. This is most readily achieved by chemical substitution. Electron doping can be attempted in all compounds by substituting Fe for Co or Ni, which will formally add 1 or 2 electrons to the band structure respectively. Alternatively, some compounds are open to both electron and hole doping by making substitutions away from the Fe plane, such as by replacing Ba with K in $Ba_{1-x}K_xFe_2As_2$ (hole doping) or O with

F in LaFeAs($O_{1-x}F_x$) (electron doping). Such changes have been shown to suppress the magnetic and structural transitions and promote superconductivity, giving phase diagrams like those shown in Fig. 2.5.

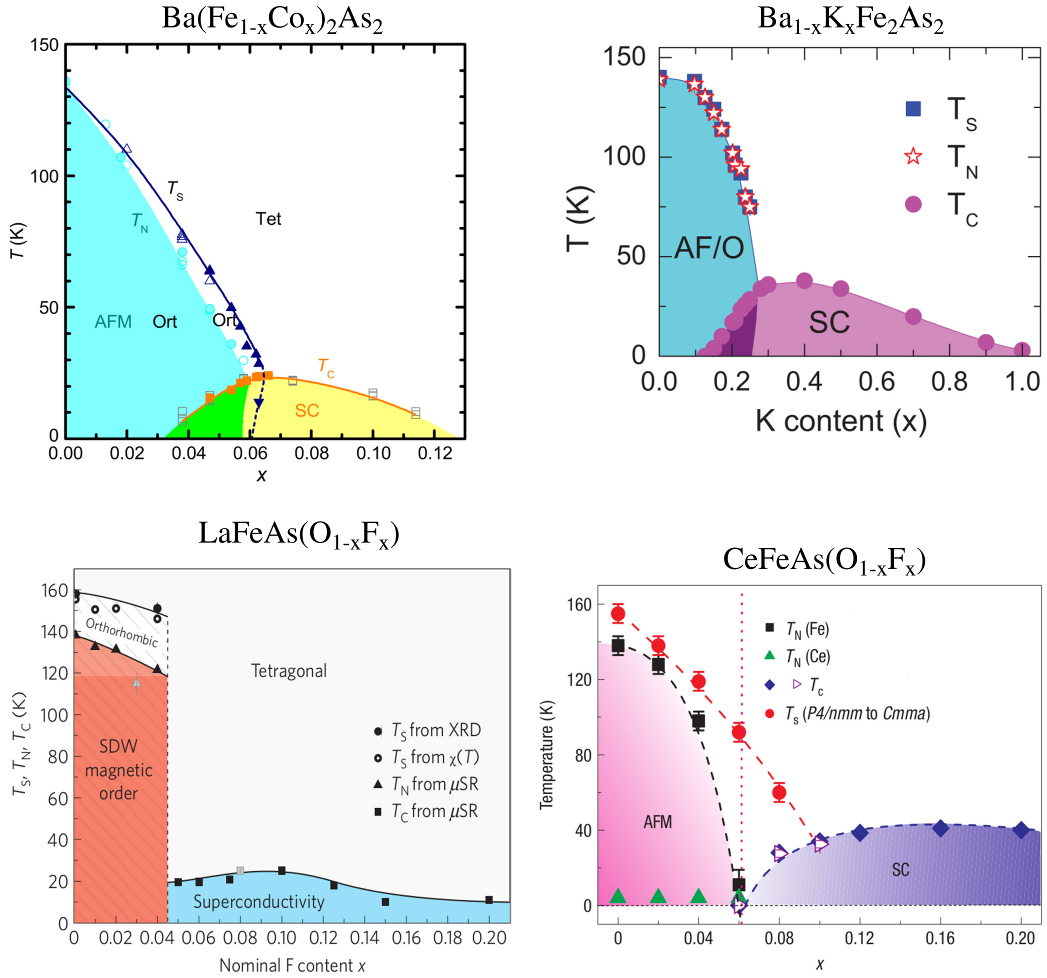

Figure 2.5: Phase diagrams for Ba($Fe_{1-x}Co_x$)$_2$$As_2$ [5], $Ba_{1-x}K_xFe_2As_2$ [6], LaFeAs($O_{1-x}F_x$) [7] and CeFeAs($O_{1-x}F_x$) [8]. All systems exhibit structural, magnetic and superconducting transitions.

In addition to substitutions intended to add or remove electrons, isoelectronic changes can also be made that have a similar effect in tuning systems from magnetism to superconductivity. This is achieved either through applied pressure [54, 55] or isovalent chemical substitution [56, 57] (which can be thought of as exerting "chemical pressure").

This suggests that the structural changes one makes when trying to dope parent compounds are just as important in driving the system towards superconductivity as band filling. The debate about exactly what any chemical substitution does to a system is worthy of explicit discussion, and I return to this in Section 2.4.

The apparent regions of coexisting superconductivity and magnetism seen in derivatives of $BaFe_2As_2$ provide another source of intense debate. Such coexistence is not typically seen in the cuprate phase diagram [58], giving the Fe-based superconductors unique importance from a theoretical point of view. It was surprising enough, in light of BCS theory, to find magnetic and superconducting phases even close to one another in cuprates and heavy fermion compounds, so the possibility of superconductivity persisting within a magnetic phase in Fe-based systems is very intriguing indeed. Of particular concern is the exact nature of this coexistence: do samples accommodate isolated regions of each phase or do magnetism and superconductivity coexist on an atomic scale? Experimental evidence for both possibilities exists but, as I present some results in Chapter 4 which add to the debate, I shall discuss this evidence in more detail there.

Finally, it is worth mentioning some interesting compounds that do not show all of these features. The most relevant to this thesis is LiFeAs, which is superconducting in its stoichiometric form and undergoes no structural or magnetic transition at any temperature (see References [14, 43, 44] and Chapter 5). Also, it is worth noting that FeSe exhibits no magnetically ordered phase dispite undergoing a structural transition [47]. The non-superconducting FeTe does order, but develops a very different magnetic structure to that observed in the pnictides [59], suggesting that its magnetic phase is not driven by the same physics.

2.3 Electronic structure and theoretical ideas

Unlike the cuprate parent compounds, which are Mott insulators, Fe-based superconductors are all metallic in the normal state. Thus, most theoretical models designed to explain the properties of these systems focus on calculated or measured details of the electronic band structure and Fermi surface. Of course there are many unresolved questions surrounding the origin of superconductivity in these materials, as there are for all high-T_c superconductors, but the theoretical model outlined in this section has gained a broad acceptance and provides the best platform on which to base the interpretation of the results presented in later chapters.

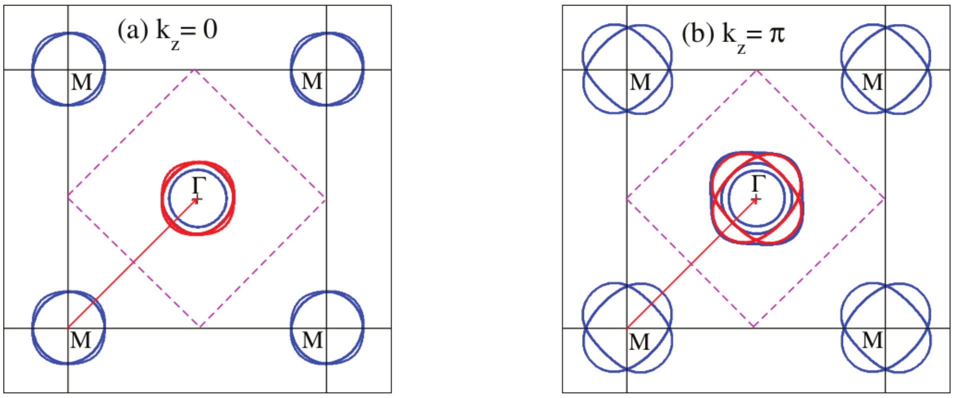

FIGURE 2.6: The calculated Fermi surface for LaFeAs($O_{1-x}F_x$) at (a) $k_z = 0$ and (b) $k_z = \pi$, taken from Reference [9]. The red lines indicate parts of the Fermi surface that have been shifted by the antiferromagnetic wavevector $(\pi, \pi, 2\pi)$, and highlight significant nesting.

Based on the measured crystal structure of LaFeAs($O_{1-x}F_x$), which was the first high-T_c Fe-based superconductor to be discovered [45], its nonmagnetic band structure was calculated by several groups [9, 60]. These indicated that there are five bands intersecting the Fermi level, originating from the five-fold degenerate Fe 3d orbitals, varyingly hybridized with the As 4p orbitals. Figure 2.6 shows the resulting Fermi surface topology for this system, composed of two electron pockets around the M point and three hole pockets[1] around the Γ point in the first Brillouin zone. As is shown in Fig. 2.6, these pockets are highly two-dimensional (cylindrical), with only some slight warping of these cylinders in k_z. Interestingly, their relative sizes mean that one can map the electron pockets onto the hole pockets almost perfectly by translating through the vector $(\pi, \pi, 2\pi)$. This is the same as the vector that characterises the magnetic structure shown in Fig. 2.4, so it is suggested that the formation of the apprently itinerant magnetic phase is driven by this so-called "nesting" of the Fermi surface [61]. Similar calculations were performed for other parent pnictide compounds [62, 63], with largely identical results that indicate the role of multi-orbital physics in these materials and the apparent ubiquity of a nested Fermi surface in the insulating parent compounds.

The formation of superconductivity is taken to result from some disruption of this nesting. Such a change in the electronic structure could be driven by altering the chemical structure or the band filling, which applied pressure or chemical substitutions would be expected to achieve. Crucially, it was demonstrated that, although the nesting condition is suppressed on electron doping, it is not removed entirely by this process [9, 60]. That is, the parts of the Fermi surface that can be mapped onto one another get smaller but do not vanish as one alters the band structure. This then allows for the existence of antiferromagnetic fluctuations that, while no longer strong enough to drive the system to order, could mediate superconductivity. Igor Mazin and colleagues proposed that this would result in a novel $s^{\pm}$ superconducting gap structure, accompanying singlet-pairing[2]. In such a structure, isotropic gaps are opened up on different parts of the Fermi surface, and are of opposite sign [60].

---

[1] The number of hole pockets depends on the doping level, with the central hole pocket vanishing on electron doping away from the parent compound [60].

[2] Triplet-pairing is also a possibility in centrosymmetric superconductors, but would probably require ferromagnetic fluctuations to mediate it. I return to this topic in Chapter 5

Since then, much experimental evidence for this model has been built up (see Reference [26] for a recent review). Early results from angle-resolved photoemission spectroscopy (ARPES) observed a nearly-nested Fermi surface in the parent compound $BaFe_2As_2$ [64, 65], with isotropic gaps opening up on different Fermi surface pockets in superconducting derivatives [64]. Phase-sensitive inelastic neutron scattering (INS) studies of the resonance mode[3] then confirmed the sign-change of the gap across these pockets [67]. Finally, the singlet-pairing state has been explicitly confirmed in several systems through measurements of the NMR Knight shift [68–70].

However, there are some aspects of this model around which consensus is not universal: There is some evidence that certain kinds of doping can alter the gap structure [71], which would challenge the pairing scenario I have discussed. Also, some have challenged the interpretation that nesting drives the formation of the magnetic phase, which also may not be entirely itinerant [72–74]. However, most agree that nesting plays a role in magnetic ordering and that spin excitations mediate the superconductivity in these compounds. The observed correlation between T_c and the As–Fe–As bond angle shown in Fig. 2.3 is then understood as an indication of the structure that optimises the details of the Fermi surface for the formation of a superconducting phase.

2.4 The doping controversy

In practice, chemical substitution is the simplest way to tune parent compounds away from magnetic order and towards a superconducting state. However, it is very difficult to explain precisely how it achieves this in Fe-based systems. Many researchers have interpreted the changes they observe on, say, replacing Fe with Co as being the result

---

[3] a build-up of intensity below T_c, interpreted as the renormalisation of spin exitations in a spin excitation-mediated superconductor [66].

of electron doping; with every Co atom introduced simply adding its extra electron to the hybridized FeX bands, thus raising the Fermi level. However, there is growing theoretical and experimental evidence that the situation is more complex and I briefly present some of this evidence in this section. It turns out that the interpretation of most of my results is not directly affected by the precise details of what chemical substitutions do, but as two of my chapters (Chapters 4 and 5) present studies of the effects of such substitutions, it is worth highlighting the complexity behind this process.

A key observation supporting the simple band filling argument came from my own research group: The authors of References [12] and [14] noted that while Ni substitution appeared to have the same effect as Co substitution on the structures of NaFeAs and LiFeAs respectively, it had twice the effect on T_c. So, for example, $NaFe_{0.975}Ni_{0.025}As$ has the same transition temperature as $NaFe_{0.95}Co_{0.05}As$ ($T_c \simeq 21\,K$). For every Fe atom replaced, Ni would be expected to contribute two electrons if acting simply as a donor, compared to a single electron added by every extra Co atom, so this effect on T_c is easily explained by the band filling scheme.

However, from calculating the electron density of such substituted atoms, the authors of Reference [75] concluded that these extra electrons are not delocalised from Co or Ni atoms and so do not add to the bands. Instead, they remain bound to their host atoms which then act as impurity scatterers. That Ni substitution has twice the effect on T_c as Co substitution was suggested to result from the intimate details of these atoms' electron distibutions.

One can see that both band filling and impurity scattering would disrupt the nesting condition: filling bands with electons or holes would raise or lower the Fermi level and alter the relative sizes of the pockets, whereas the presence of impurity scatterers would simply wash out parts of the Fermi surface altogether. The two cases must therefore be distinguished by direct experimental probes of the electronic structure.

Measuring the effects of doping on the Fermi surface is not trivial. In order to observe quantum oscillations, the most well-established way of probing the Fermi surface topology, one requires a sample free of any significant defects. Even if they primarily act as electron donors or acceptors, transition metals substituted onto the Fe site will act as just such defects, and so quantum oscillations have not yet been observed in systems containing transition metal substitution. ARPES does not suffer from this constraint (though one still requires single crystal samples with very clean surfaces) so some ARPES studies of the effects of Co substitution on the Fermi surface of $\mathrm{BaFe_2As_2}$ have been made [76, 77]. These appear to confirm the shrinking and growth of hole and electron pockets respectively, consistent with the band filling picture, and no evidence for a washed-out Fermi surface has been found. ARPES measurements on the formally hole-doped $\mathrm{Ba_{1-x}K_xFe_2As_2}$ series also appear to support the band filling picture [78].

This is not the end of the debate, however. One would expect Ru to be isovalent to Fe and have no effect on magnetism or superconductivity under the band filling scheme, and yet the phase diagram of $\mathrm{Ba(Fe_{1-x}Ru_x)_2As_2}$ looks remarkably similar to that of $\mathrm{Ba(Fe_{1-x}Co_x)_2As_2}$ [56] (though note that one needs much more Ru than Co to induce superconductivity: $x_{\mathrm{Ru}} \sim 0.3$ gives the optimal T_{c} as opposed to $x_{\mathrm{Co}} = 0.06$ [5]). Unsurprisingly, measurements of the Fermi surface confirm no significant change in topology with increasing Ru concentration [79], and so the phase diagram has been explained as a consequence of diluting the net magnetic moment on the Fe site. P substitution in $\mathrm{BaFe_2(As_{1-x}P_x)_2}$ would also not be expected to alter the band filling, and yet it too induces superconductivity [57]. ARPES measurements on this compound conclude that, while the changes it makes to the electronic structure are driven purely by its impact on the chemical structure, the hole pockets are, in fact, found to expand more than the electron pockets [80] as more P is added. Thus, the chemical pressure exerted by this substitution causes an effective hole doping.

The only conclusion one can draw from all this is that chemical substitutions have a very complicated effect on the electronic structure of a compound. There is plenty of evidence that supports a band filling scenario, but the structural changes induced by the substitution also play an important role, as do the magnetic properties of the substituted atom. A recent report [81] demonstrates that the situation varies depending on the species and locations of the atoms involved in substitution. From x-ray absorption data on $BaFe_2As_2$, these authors conclude that substituting K for Ba and Co for Fe do give rise to hole and electron doping respectively, whereas impurity scattering plays a role when Fe is replaced with other transition metals. As most of this thesis is concerned with Co-substituted systems, and the results often compared to those from $Ba(Fe_{1-x}Co_x)_2As_2$ or $Ba_{1-x}K_xFe_2As_2$, I shall therefore use the term “doping” rather freely. However, one should be aware that each use of this term comes with the caveats discussed in this section.

Chapter 3

Synthesis, characterisation and experimental techniques

3.1 Introduction

This chapter introduces the techniques used to prepare and study samples of the compounds described in this thesis. Following an introduction to the general principles governing the growth of both polycrystalline and single crystal samples, I move on to introduce the three main experimental techniques I used to analyse them: x-ray diffraction (XRD), magnetometry and muon-spin rotation (μSR). As μSR measurements were performed on every system I subsequently discuss, I save a detailed introduction to this powerful technique for the final part of this chapter. Before that, XRD and magnetometry are given briefer introductions, in which I primarily focus on the equipment I used (though some relevant background is presented where necessary). I also describe how both XRD and low-field magnetometry were used to assess the quality of new samples, before such samples were used in larger and more time-consuming experiments.

3.2 Synthesis

3.2.1 Polycrystalline samples: high-temperature synthesis

Novel systems are often initially studied in polycrystalline form. Compared to single crystals, powders can often be easier to make to a high purity and are easier to analyse, as I shall explain. The majority of powder samples are made by simply heating a stoichiometric mixture of the constituent elements to a sufficiently high temperature; high enough to overcome the kinetic energy barriers impeding reaction and allowing a thermodynamically favourable product to form. If the desired compound is the only such product possible for a given set of reagents, and they have been mixed in the correct molar ratio, then the resulting sample will be single-phase.

To achieve a successful synthesis, one must be sure to apply enough heat to overcome these kinectic energy barriers while maximising the reaction rate in an efficient a manner as possible. The exact value of the heating temperature is usually determined by trial and error, although intelligent guesses can be made based on the procedures used to make structurally or chemically similar compounds. The best way to optimise the reaction rate is to maximise the surface contact area of the constituent elements. Many transition metals (as well as their oxides, chlorides, flourides etc) can be purchased as high-purity powders and ground to a very fine grain size using an agate pestle and mortar. In addition, finely ground mixtures are routinely pressed into pellets, increasing the contact area of reagents still further.

3.2.2 Intercalated systems: soft chemistry

The traditional way of making powder samples (described in the previous section) is not always appropriate, even if the desired product is thermodynamically stable. For example, Chapter 6 describes my work on a series of samples made by intercalating ammonia and metal atoms in between layers of FeSe, and they decompose above ∼ 100°C [82]. In order to make these compounds, one must use a low-temperature route like that described in this section.

Intercalation involves the incorporation of guest atoms or molecules into a host lattice, usually onto interstitial sites between atomic layers, while preserving the symmetry of that host lattice. Typically, this takes place in solution. The starter material (the host) is placed into a container with a liquid in which the guest atoms have been dissolved. If the bonds between layers in the host can be strengthened by incorporating spacer atoms, these guest atoms will move into the host lattice even at room temperature. This process may be speeded up by heating the mixture over a hot plate, or by using a magnetic stirrer to combine the reagents more effectively.

Such intercalation of guest atoms often occurs inhomogeneously. In addition, as these atoms are incorporated they inevitably exert stress on the host lattice that may break up any significantly-sized crystallites of the host material. It is therefore rarely possible to make single crystals of an intercalated compound in solution.

3.2.3 Single crystals: flux growth

Although typically harder to make, for reasons that shall become apparent, single crystal samples offer significant advantages to the physicist over polycrystalline samples. The most obvious of these is the ability to measure physical properties along specific crystallographic directions. Anisotropic quantities, such as superconducting critical fields, can only be characterised directly using single crystal samples. Additionally, grain boundaries constitute major defects for the purposes of some measurements, such as resistivity. In performing such measurements on even very pure powders, one is then not only restricted to measuring spacially averaged quantites, but also confronted with a significant source of experimental uncertainty.

There are many different ways of making single crystals, each with their own advantages. One of the simplest and cheapest, certainly compared to floating zone or bridgeman methods, is the so-called "flux method". One may hope to make a crystal by first melting a powdered sample and then very slowly freezing it, but the problem here is that most inorganic compounds of interest have higher melting points than typical furnaces allow (i.e. $T_{\mathrm{melt}} > 1500°\mathrm{C}$). Using the flux method one gets around this problem by dissolving the reagents in a liquid flux, typically a metal with a relatively low melting point, and precipitating the crystal out of this flux during a slow cooling process.

The establishment of a heating and cooling regime for single crystal growth is, again, a process largely governed by trial and error. However, even in the case of entirely novel systems where little or no literature is available for guidance, one can make an intelligent estimate of the correct temperature regime based on binary alloy phase diagrams. Such diagrams plot the evolution of the solid-liquid phase boundary for mixtures of two elements in varying ratios, and show which ratios form stable compounds. An example of this, for the Na-Sn system, is shown in Fig. 3.1. Reliable ternary phase diagrams are rare (and quarternary diagrams non-existent) so the growth of such single crystals can never be mapped out entirely using binary phase diagrams. That said, analysing diagrams relating to all pairs of reagents, and those for each reagent and the selected

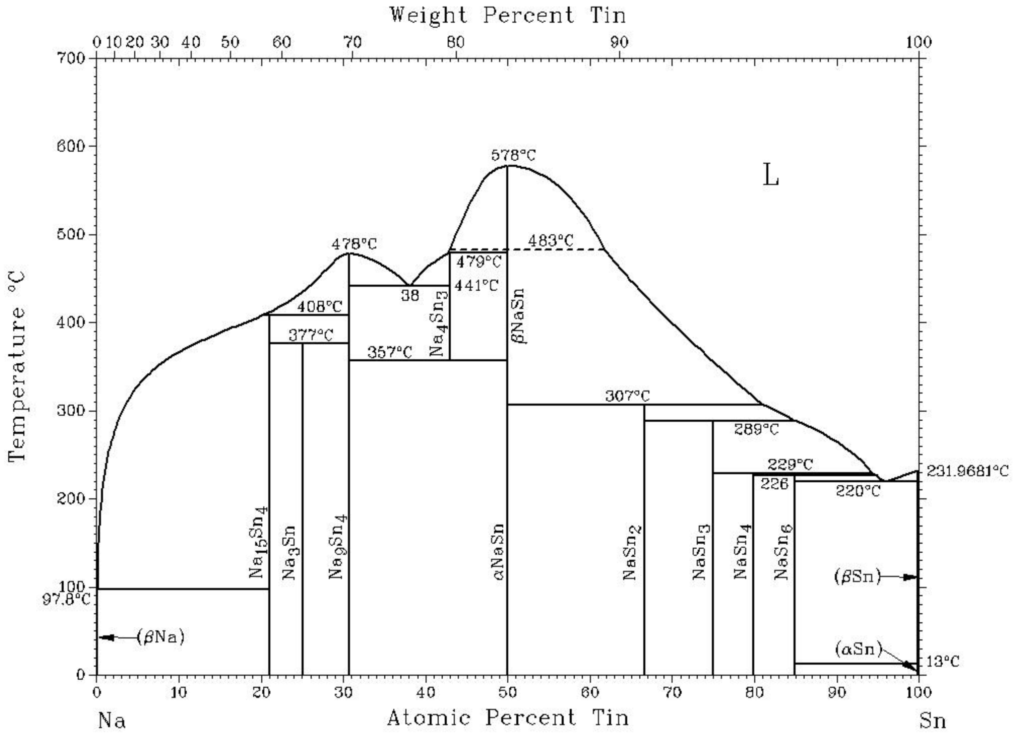

FIGURE 3.1: Binary alloy phase diagram for Na–Sn, showing the evolution solid-liquid (L) phase boundary as the ratio of constituent elements is altered. Also shown are the ratios of these elements that form stable compounds.

flux material, allows one to build up a good sense of the temperature regime most likely to work.

Once a crystal has been grown, it must be removed from the flux in a way that does not damage or pollute the crystal. One may do this mechanically, using a solvent or by decanting off the liquid flux while the reaction vessel is still hot. The best approach is directed by the properties of both the crystal and the flux and one can often only perfect this procedure with practice.

The selection of flux is also potentially troublesome. Although its chief characteristic must be its low melting temperature (typically well below 1500°C), the way it reacts with the constituent elements must also be considered. Even if there are no competing stable products of reagents and flux trying to form, one may still find atoms of the flux material incorporated into the target crystal, either on interstitial sites or by substituting themselves for reagent atoms (see, for example, Reference [83]). One way to avoid this is by using a flux material composed entirely of one or more of the constituents, and this variant of the method is called the "self-flux technique". I make use of this technique to grow single crystals of $NaFe_{1-x}Co_xAs$, as described in Chapter 7.

3.2.4 General concerns

For the synthesis of any high quality sample, one must be in control of the reaction at every stage. This means starting with the purest reagents and keeping them in an inert environment throughout the process. Many elements can be purchased in highly pure forms[1] and, to keep these starter materials in good condition, the handling of non air-stable substances is often carried out in a glove box. During this project, all work was carried out in a Glove Box Technology argon-filled drybox equipped with BASF copper catalyser and a circulating argon flow to keep the O_2 and H_2O levels below 2 ppm at all times. On heating the sample, one must ensure that the reagents are held in close enough proximity to react, while undergoing no unwanted reactions with their surroundings. Alumina crucibles and arc-welded Ar-filled Nb tubes were used routinely to encapsulate reagents, and these were themselves housed in evacuated silica ampoules (where appropriate) to prevent Nb oxidation.

---

[1] although it can sometimes be more cost-effective to purify cheaper, low quality reagents in the lab.

3.3 Experimental Techniques

Following the synthesis of a sample, one immediately wants to assess the purity of that sample and confirm its composition. The samples described in this thesis were characterised by using a combination of x-ray diffraction and low-field magnetometry, and these techniques are now described. As both were also used in more detailed experimental studies, I give a general introduction to these techniques before specifically explaining how they were used as characterisation tools. I also present introductions to the two other techniques I made use of: pulsed-field magnetometry and muon spin rotation.

3.3.1 X-ray diffraction

In order to fully understand the physical properties of a compound, accurate information about its atomic structure must be obtained. Over the last century, analysing the characteristic patterns produced when crystalline compounds diffract incoming waves or particles has been established as the most reliable way of obtaining this information. In particular, x-ray diffraction (XRD) was used to study the structures of all compounds described in this project. In this section I describe the equipment I used for this work, and the numerical methods used to analyse diffraction data. A complete account of this technique is outside the scope of this thesis (more information can be found in Reference [84]) but I do present some relevant technical details in support of this section in Appendix A.

A diffraction pattern consists of a series of high-intensity peaks or spots superimposed on a low-intensity background. Each peak corresponds to a different set of crystal planes, labelled by Miller indices[2] $\{h, k, l\}$, and the relative positions of these peaks

---

[2] defined such that planes intersect the crystallographic axes a, b and c at a/h, b/k and c/l respectively.

depend on the spacings of the crystal planes. The positions of the atoms within these planes, including information about the atomic species, site occupancy and thermal displacement, can be extracted from the intensity of the peaks.

In order to extract this information, one typically uses a proposed model structure to generate a theoretical diffraction pattern that can be numerically fit to the data using a least-squares optimisation routine. This is the basis of Rietveld refinement, for which one proposes a model containing the crystallographic space group, lattice parameters, atomic locations within the unit cell, occupancy factors and thermal displacement parameters. The refinement procedure then attempts to account for both peak position and peak intensity by adjusting the structural quantities in the model accordingly.

Alternatively, if one is interested only in the lattice parameters of a compound, Pawley refinement can be used. In this method, the input model contains no information about atomic locations or occupancy factors, and therefore the fitting routine incorporates peak intensity as an arbitrary quantity that can be directly adjusted to fit the data. Only the lattice parameters are adjusted in the input model, so only the positions of the peaks in the diffraction pattern are physically accounted for. Both Rietveld and Pawley refinement were used during this project. When carrying out the former, I used the GSAS software package [85] with the EXPGUI interface [86], while TOPAS [87] was used for the latter. More information on both Rietveld and Pawley methods can be found in Reference [88].

Throughout this project, I used three diffractometers to obtain diffraction data, each with different capabilities. These are the PANalytical X'Pert Pro, the Oxford Diffraction SuperNova and the ID31 Beamline at the ESRF, Grenoble, France. The first two of these are small, relatively low-resolution diffractometers, used to analyse polycrystalline

(X'Pert) and single crystal (SuperNova) samples in the laboratory. The ESRF employs a synchrotron x-ray source, meaning that the ID31 Beamline is capable of obtaining structural data on powder samples at much higher resolutions than is possible using the X'Pert. More information on all of these pieces of equipment can be found in Appendix A.

3.3.2 Magnetometry

In this section I describe two techniques used to measure magnetic susceptibility; a quantity of great interest in the study of any superconducting or magnetic system. Frequently one is satisfied by measuring the response to low fields ($< 7\,\mathrm{T}$), for which one can use a SQUID. In Chapter 7, I present a study of the response to much higher field (up to 45 T) which was achieved using a pulsed-field system.

3.3.2.1 The SQUID

Throughout this project, measurements of the low-field DC susceptibility (the response of a system to a static applied field) were made using a Quantum Design Magnetic Properties Measurement System (MPMS). At the heart of this system is a Superconducting QUantum Interference Device (SQUID), which is based upon a current loop containing two Josephson junctions, as shown in Fig. 3.2.

One can show [89] that the critical current of this loop is related to the flux, Φ, passing through it by

$$I_{\mathrm{c}}(\Phi) = I_0 \left| \cos\left(\frac{\pi\Phi}{\Phi_0}\right) \right| . \tag{3.1}$$

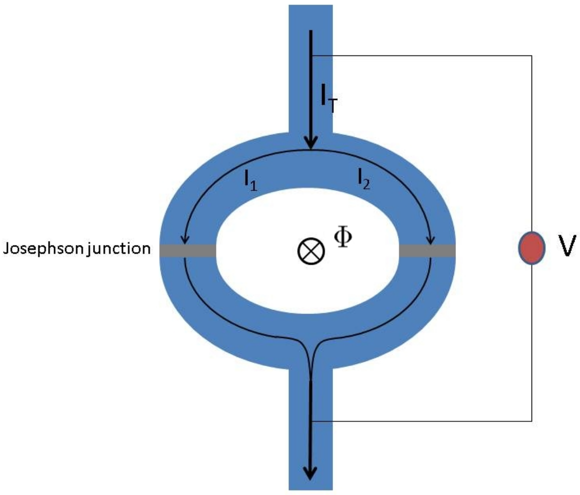

FIGURE 3.2: A schematic diagram of the Superconducting QUantum Interference Device (SQUID). Interference between I_1 and I_2 gives rise to oscillations in the critical current of the loop, I_c, whose frequency is related to the flux, Φ, passing through the loop.

The MPMS then measures the I–V characteristic of this loop (potentially at variable temperatures, fields and pressures) and infers $\Phi(T, B, P)$ from the behaviour of $I_\mathrm{c}(T, B, P)$. The magnetisation, M, of the sample will have a strong effect on the resulting flux through the loop, and so can be extracted from it. Subsequently, the susceptibility is given by

$$\chi = \left.\frac{\partial M}{\partial H}\right|_{H\to 0} . \tag{3.2}$$

The precision of these measurements is set by the size of the flux quantum $\Phi_0 = 2 \times 10^{-15}$ Wb. For typical loop sizes this corresponds to flux densities of around 10^{-10} T, making a SQUID an incredibly sensitive device.

3.3.2.2 Pulsed-field magnetometry

For this project, high-field susceptibility data were taken at the Nicholas Kurti High Magnetic Field Laboratory in Oxford. This laboratory makes use of a pulsed-field system, in which a large current stored in a capacitor bank is discharged through a resistive coil over a millisecond time-scale. The combination of a short pulse time and a liquid nitrogen cooling system minimises damage to the coil caused by both Joule heating and the mechanical strain induced by the generated fields. These fields can reach up to 45 T.

While there are many ways of making use of such fields, for this work a technique based on a Proximity Detector Oscillator (PDO) circuit was used. The sample is placed in a coil connected in parallel to a capacitor (and effective resistors) to form an LCR circuit, with resonant frequency $\omega_0 = 1/\sqrt{\mathrm{LC}}$. The inductance of the coil, L, is then altered by changes to the sample's susceptibility which are picked up by measuring changes to the resonant frequency. A more complete discussion of the PDO circuit can be found in Reference [90].

3.3.3 Aside: a note on characterisation

Before taking on a large-scale experimental study, either at a facility or in the lab, one must be sure of the quality of the samples one intends to use. For this project, I was concerned with both the purity of samples and also their stoichiometry: much of my work analysed the effects of chemical substitutions, so knowing that the nominal amount of a substituted element had been successfully incorporated during synthesis was vital. To gain an immediate impression of the quality of these samples I, along with my collaborators, frequently used XRD and SQUID magnetometry as characterisation tools.

Phase purity was most readily checked using XRD, as the presence of any unwanted phases was revealed by peaks in the diffraction pattern that could not be accounted for by the main phase. Additionally, small magnetic impurities (such as elemental Fe) can be picked up during susceptibility measurements, so these were also performed to asses purity. Stoichiometry was confirmed by comparing data from new compositions in a series with published data from other members of that series. For instance, one would expect to find a monatonic variation in the lattice parameters of a compound as incremental amounts of one element are substituted for another. Published plots of, say, unit cell volume against Co concentration in $\mathrm{NaFe}_{1-x}\mathrm{Co}_x\mathrm{As}$ can then be used to find the true value of x in a newly synthesised compound if one measures its lattice parameters. A good example of carrying out this procedure can be found in Chapter 4.

In this way, a series of samples with well-known compositions could be prepared, allowing one to study the effects of chemical substitution with confidence.

3.3.4 Muon spin rotation

I now present a more detailed introduction to the technique most used during this project: muon spin rotation (μSR).

A μSR experiment involves implanting a spin-polarised set of muons into a sample and tracking the precession of the spins of these muons in the local magnetic fields they encounter [11, 91]. μSR is then a local probe of a system's magnetic configuration, which makes it an invaluable tool in analysing long-range magnetic order (be it either intrinsic or field-induced[3]), inhomogeneous, localised or fluctuating magnetic order, and spin-glass phases. The muon is sensitive enough to respond even to nuclear dipole

---

[3] such as the vortex lattice of a Type-II superconductor.

moments, meaning that dynamic structural processes, such as ionic diffusion, can also be studied.

In all the aforementioned cases the muon is assumed to be an innocent observer of these processes, playing no part in them directly. The muon will of course act as a small perturbation to the system but in most cases this can be ignored. There are a whole range of techniques, however, where the muon is itself the subject as well as the probe of investigation. Muons can themselves diffuse, tunnel through potential barriers and form bound states with electrons called "muonium". All of these processes, each a different response to the muon environment, can reveal intimate details about the host sample but, as they play no part in the studies undertaken here, no more is said about them[4]. More details on these applications of the muon technique can be found in Reference [11].

3.3.4.1 Basic principles

The practicalities of generating a beam of spin-polarised muons that can be implanted into a sample, as well as a description of what happens to the muon when it enters the sample, is given in Appendix B. In this section, I describe the essence of the technique.

μSR relies on a single property of the muon above all others: the asymmetry of its decay. With a lifetime of $2.2\,\mu s$, muons decay into positrons and neutrinos. Parity is violated in this weak process and, it turns out, the positron is emmitted preferentially along the direction in which the muon was pointing at the moment of decay. The angular distribution of positron emmission is shown in Fig. 3.3.

Muons are timed as they enter the sample, and the detection of the emerging positrons is also timed. Armed with this and the decay asymmetry, one can see how a careful

---

[4] I speculate that muonium formation may affect data presented on the ammonia-intercalated FeSe systems discussed in Chapter 6, but experiments to characterise this directly have not been carried out.

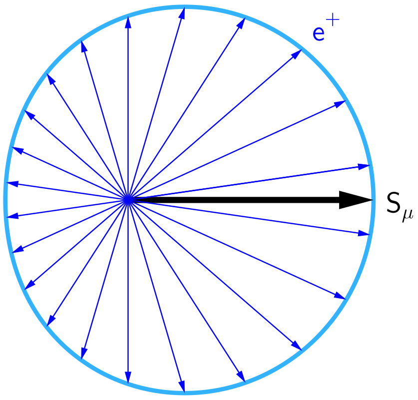

Figure 3.3: The asymmetric angular distribution of positron emission. Positrons are emitted preferentially along the instantaneous direction of the muon spin, S_μ, at the time of decay.

arrangement of positron detectors would allow one to track muon precession within the sample and thus probe the internal field distribution. The remainder of this section defines the experimentally recorded quantity, the so-called "asymmetry spectrum".

Following implantation, each unit cell will contain several muons, in fixed stopping sites and initially with their spins fully polarised. These spins precess in whatever local field they experience with a frequency $\nu_\mu = \gamma_\mu B_{\text{local}}$, before each muon decays. The exact time of decay is random but the distribution is centered around $\tau_\mu = 2.2\mu$s. After a muon has decayed, another muon from the beam will occupy its stopping site, precess and decay after a different time, only to be itself replaced, and so on. This means that, rather than thinking of an ensemble of individual muons, it is equivalent to simply consider a positron emitter at every muon site; continually precessing and emitting positrons at random, in directions governed by the asymmetric distribution in Fig. 3.3.

A single such positron emitter, initially polarised along the z-direction and at an angle θ to the local field, is shown in Figure 3.4. The z component of the spin polarisation, $\sigma_z(t)$, is given by:

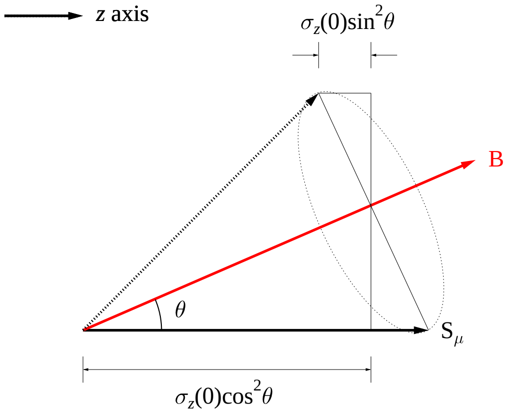

FIGURE 3.4: Muon spin precession around a local internal field **B**.

$$\sigma_z(t) = \sigma_z(0)\left(\cos^2\theta + \sin^2\theta \cdot \cos(\gamma_\mu|\mathbf{B}|t)\right). \tag{3.3}$$

Considering only powder samples containing static internal fields (conditions that apply to the majority of experiments carried out during this project), the time-dependent polarisation of the full muon ensemble is obtained by taking a spacial average over all the angles the polarisation could make with this local field, as well as an average over all field values. This gives

$$G_z(t) = N\int \mathrm{d}|\mathbf{B}| \int_{\text{sphere}} \mathrm{d}\hat{\mathbf{B}}\left(\cos^2\theta + \sin^2\theta \cdot \cos(\gamma_\mu|\mathbf{B}|t)\right) \cdot P(|\mathbf{B}|), \tag{3.4}$$

where $P(|\mathbf{B}|)$ is the sample's internal field distribution and N is a constant normalisation factor. If $P(|\mathbf{B}|)$ is normalised to unity then N can be chosen to simplify Eq. 3.4 to

$$G_z(t) = \frac{1}{3} + \frac{2}{3} \cdot F\{P(|\mathbf{B}|)\}(t), \tag{3.5}$$

where $F\{P(|\mathbf{B}|)\}(t)$ is the Fourier cosine transform of $P(|\mathbf{B}|)$. It should be stated that this formula is only strictly applicable in the case where no external field is applied – i.e. $P(|\mathbf{B}|)$ is intrinsic to the sample – but a similar relationship applies to experiments in-field [11].

Positrons are emitted preferentially in parallel to this precessing polarisation and one now requires a careful arrangement of detectors to track it effectively. In practice, there are two different geometrical arrangements of detectors used in μSR experiments, known as longitudinal-field (LF) and transverse-field (TF) modes. The names describe the direction of an applied field with respect to the initial muon polarisation and it should be noted that in experiments with no applied field [a zero-field (ZF) experiment] one arranges the detectors in LF mode.

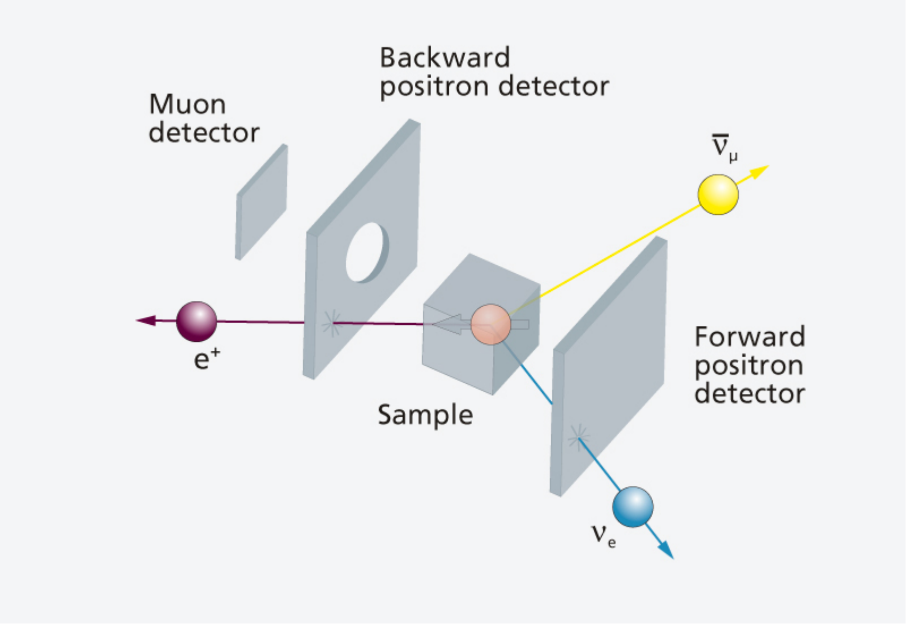

Figure 3.5: A schematic representation of the detector arrangement for a zero-field or longitudinal-field μSR experiment. Figure taken from Reference [10].

Figure 3.5 shows the essential detector arrangement in a LF-μSR experiment: one places a detector (or perhaps a bank of detectors) both in front of and behind the sample with respect to the muon momentum. These are known as the backward (B) and forward (F) detectors respectively. Given a time-dependent polarisation $G_z(t)$ as defined in Eq. 3.4, the number of positrons counted in the forward and backward detectors will be

$$N_{\mathrm{F,B}}(t) = N_0 v_{\mathrm{F,B}} \exp(-t/\tau_\mu)[1 \pm a_{\mathrm{F,B}} G_z(t)]. \tag{3.6}$$

Here, $v_{\mathrm{F,B}}$ is defined as the detector efficiency and $a_{\mathrm{F,B}}$ is the intrinsic detector asymmetry that accounts for the fact that positrons are not emitted solely along a direction parallel to $G_z(t)$, but have trajectories that obey an angular distribution (Fig. 3.3). $G_z(t)$ is then measured by taking the normalised difference between the counts in the forward and backward detectors. Making the typically valid assumption that $a_{\mathrm{F}} = a_{\mathrm{B}} = a$, and defining $\alpha = v_{\mathrm{F}}/v_{\mathrm{B}}$, the so-called “Asymmetry function” is given by:

$$A(t) = aG_z(t) = \frac{N_{\mathrm{F}} + \alpha N_{\mathrm{B}}}{N_{\mathrm{F}} - \alpha N_{\mathrm{B}}}, \tag{3.7}$$

and it is this quantity, directly related to the sample’s internal field distribution via Eq. 3.5, that is measured in a μSR experiment.

In a ZF experiment, this field distribution is intrinsic to the sample. In the case of applied field experiments (LF or TF), one is measuring the convolution of this intrinsic distribution with that from the applied field (a delta function). I shal now briefly outline some of the different physical phenomena one can employ ZF, LF, or TF-μSR to examine.

Aside: To analyse data from any μSR experiment, one typically proposes a model for the internal field distribution and uses a least-squares optimising routine to fit the resulting asymmetry function to the data. Throughout this project, such fitting was carried out using the WiMDA package [92].

3.3.5 Typical applications of μSR

This section gives a brief introduction to the different physical phenomena I studied using the three different modes of a μSR experiment. Important practical and theoretical considerations are given, where appropriate, such that the data presented in subsequent chapters requires no preliminary explanation. Again, more details on all of what follows can be found in Reference [11].

3.3.5.1 Zero-field μSR

If a sample is paramagnetic, an internal magnetic field can only come from the magnetic dipoles of the atomic nuclei. These will generally be quasi-static and randomly orientated, so the resulting field distribution can be well-described by a Gaussian function [11]. It can be shown [11] that the Cosine fourier transform of this distribution gives rise to an asymmetry spectrum that is described by a so-called Kubo-Toyabe (KT) function, shown in Figure 3.6(a). This function resembles a damped oscillation followed by a flat tail at 1/3 of the initial asymmetry value, which comes from the constant 1/3 term in Equation 3.5.

If the 1/3 tail is not flat but decaying, this is often a signature of dynamic phenomena. Processes such as the diffusion of light ions within the sample, or indeed muons through it, can often be described by the "strong collision approximation" [11]. Here, one assumes that, after a time t, the field distribution will change with a probability $P(t) \propto \exp(-\nu t)$ where ν is the fluctuation rate. Both before and after this "collision", the asymmetry spectrum is described by a KT function. These pre- and post-collision KT functions are unrelated, as this is a Markov process. When incorporating successive collisions, the overall asymmetry is then the combination of the initial parts of many separate

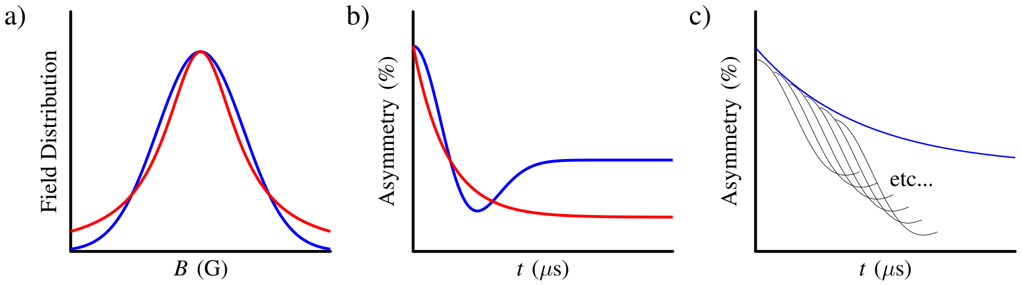

FIGURE 3.6: a) Gaussian (blue) and Lorentzian (red) field distributions, along with (b) the asymmetry spectra they give rise to. (c) An exponential asymmetry can also be the result of dynamic processes within the strong collision approximation [11]: the black lines are the relaxations embarked upon after each successive "collision", or dynamic shift in $P(B)$, and the blue (exponential) line is the combined result.

KT functions, and this combination resembles an exponential decay [11], as shown in Fig. 3.6(c).

Of course, observing an exponential decay is not a definite signature of dynamics (as I shall demonstrate in later chapters). If some static magnetic effect broadens the field distribution so that it becomes more Lorenztian than Gaussian [Fig. 3.6(b)], the cosine Fourier transform will lead to an exponential relaxation function also. Localised or incommensurate order, as well as spin-glass phases, can all give rise to exponential relaxation functions [11], and these may or may not involve dynamic effects.

Therefore, observing an exponential (or non-KT) relaxation is often highly ambiguous as many different phenomena can give rise to superficially similar asymmetry spectra. To distinguish between these cases, one can frequently gain more information from LF- or TF-μSR (see subsequent sections), but one also often requires the results from complimentary techniques, such as magnetometry or neutron scattering.

One phenomena that can be unambiguously verified using ZF-μSR is commensurate, long-range magnetic order (LRO). In this case, muons at crystallographically equivalent

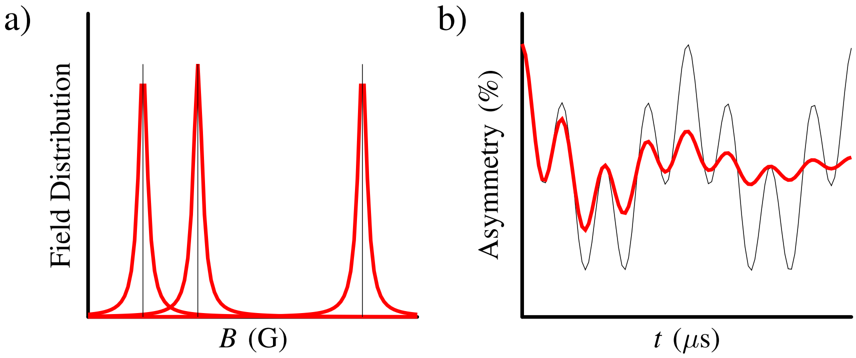

FIGURE 3.7: a) The field distribution and (b) asymmetry spectra for a sample with long-range commensurate magnetic order and three muon stopping sites per unit cell. The black lines show the ideal case, while the red lines include the effects of inevitable sample inhomogeneities or magnetic fluctuations that broaden $P(B)$ and damp $A(t)$.

sites in different unit cells will experience the same field right across the sample, and thus precess at the same rate. The field distribution will then be a series of delta functions at these fields, one for each muon site, and the resulting asymmetry will be a corresponding superposition of cosine functions. In practice, sample inhomogeneities or magnetic fluctuations always act to broaden these delta functions slightly, and thus damp the oscillations in the asymmetry function, as shown in Fig. 3.7. Of course, if the magnitude of the field at a given site is too large, perhaps due to a large ordered moment, the resulting precession will be too fast for the detectors to track. In this case, one loses some asymmetry below the ordering temperature. Thankfully, such a loss of asymmetry is often another unambiguous piece of evidence for LRO, unless one suspects the formation of muonium occurs in the sample [11]. If oscillations are observed, their frequencies will be directly proportional to the value of the ordered moment and will therefore act as order parameters for the magnetic state. The value of the moment is generally not directly calcuble from these oscillation frequencies without knowledge of the muon site, but I shall demonstrate a solution to this problem in Chapter 4.

3.3.5.2 Longitudinal-field μSR

In this project, LF-μSR had one main application: to help distinguish between some of the many cases discussed in the previous section that can give rise to similar asymmetry functions. Applying a field in the same direction as the initial muon polarisation will act to suppress their subsequent precession, and lead to a flat asymmetry. If some relaxation is observed in LF, it reveals something about the strength of the coupling between muons and the spins within the sample. Typically, one would observe how the spectra changes with applied field and at which point the field is strong enough to overcome the effects of these spins. Dynamic processes are routinely characterised in this way; they are often affected less by a longitudinal field than static processes and the LF method also provides a way to measure the fluctuation rate, ν [11].

3.3.5.3 Transverse-field μSR

This variant of the muon technique involves applying a magnetic field perpendicular to the initial muon polarisation, so the field distribution is a delta function that is broadened by any magnetism in the sample itself. One then measures the increased width of this distribution by relating it to the damping of the oscillating asymmetry function. There may be several sources of this broadening beyond the nuclear dipole field distribution, but one case deserves special mention as it was studied frequently throughout this project.

If the field is applied to a Type-II superconductor, and satisfies $B_{\mathrm{c1}} < B_{\mathrm{applied}} < B_{\mathrm{c2}}$, then a significant contribution to the width of the distribution will come from the vortex lattice. The structure of the vortex lattice depends partly on the penetration depth, λ, so it is unsurprising that there exists a direct relationship between λ and the damping of the oscillating asymmetry. I now proceed to explain this briefly, and more detailed accounts can be found in References [11, 93, 94].

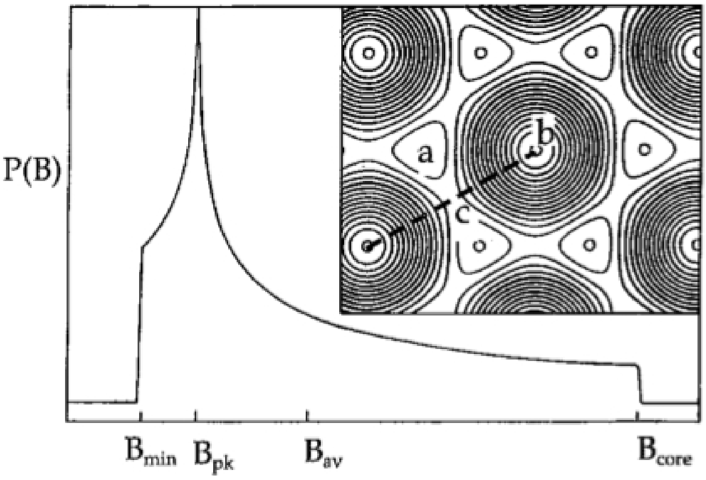

FIGURE 3.8: The theoretical internal field distribution experienced by muons implanted into the vortex lattice of a Type-II superconductor. B_{min} corresponds to muons at site (a), B_{pk} to site (b) and B_{core} to site (c) (see text). Figure taken from Reference [11].

Figure 3.8 shows the theoretical field distribution experienced by muons in an ideal[5] vortex lattice. In general, the distances between vortices will be much larger than crystallographic lattice parameters, and the vortex lattice geometry will not be directly related to the crystal structure. Therefore, muons sit at random locations within the vortex lattice and experience the entire range of fields across the resulting distribution. The lowest field within the sample will occur at points equidistant from three neighbouring vortices [this is site (a) in Fig. 3.8] and the maximum field occurs at the vortex core [site (b)]. The field drops off quickly as one moves away from the core such that the spacial region containing fields close to B_{core} is small, hence the long tail in $P(B)$. However, there is a much larger spacial region containing fields close to B_{pk}, which corresponds to site (c), hence the peak in the distribution observed at this field. In real samples, these features are smeared out somewhat by sample imperfections and, in the case of powder

---

[5] a triangular arrangement of vortices in a paramagnetic sample which sits in a field $B_{\mathrm{c1}} \lesssim B_{\mathrm{applied}}$, such that we can ignore core overlap.

samples, an asymmetric Gaussian distribution is a reasonable approximation to $P(B)$, as shown in Fig. 3.9(a).

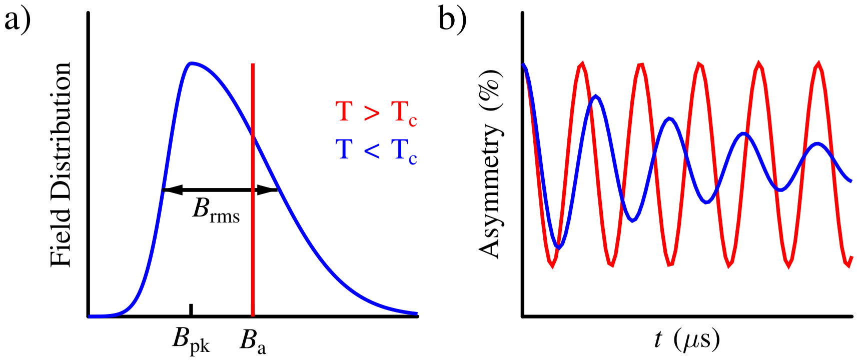

FIGURE 3.9: a) the field distribution for a superconductor above and below T_{c}. The ideal field distribution in Fig. 3.8 is shown here in a more realistic, smeared out form approximated by an asymmetric Gaussian. This gives rise to the asymmetry spectra shown in (b).

Figure 3.9(b) shows the corresponding asymmetry function; a damped oscillation at a frequency $\gamma_\mu B_{\mathrm{pk}}$. Note that, as the superconductor partially screens the applied field, $B_{\mathrm{pk}} < B_{\mathrm{applied}}$ and so the frequency of this oscillation drops below T_{c}. This is called the "diamagnetic shift" and its observation helps one confirm the broadening of the field distribution is at least partly due to the vortex lattice. The damping of the oscillation is described by a Gaussian envelope, $\exp(-\sigma^2 t^2/2)$. The width of the field distribution, $B_{\mathrm{rms}} = \langle (B - \langle B \rangle)^2 \rangle$, is then simply related to the damping factor by $\sigma = \gamma_\mu B_{\mathrm{rms}}$. To find the dependence of B_{rms} on λ, one must solve the modified London equation appropriate for a lattice of vortices, at positions $\mathbf{r}_n$ and each carrying a quantum (Φ_0) of flux:

$$\mathbf{B}(\mathbf{r}) + \lambda^2[\nabla \times \nabla \times \mathbf{B}(\mathbf{r})] = \Phi_0 \sum_n \delta(\mathbf{r} - \mathbf{r}_n). \tag{3.8}$$

This is solved for $\mathbf{B}(\mathbf{r})$ (usually using Fourier analysis) so that B_{rms} can be calculated. For powder samples of anisotropic superconductors, such as cuprates and pnictides, it can be shown [94] that

$$B_{\text{rms}} = \frac{\sqrt{0.00371}\Phi_0}{(3^{\frac{1}{4}}\lambda_{ab})^2}, \tag{3.9}$$

Note that this expression contains the *in-plane* penetration depth, λ_{ab}, rather than an isotropic value λ. In anisotropic superconductors, the out-of-plane penetration depth, λ_c, will be much larger than λ_{ab} and will make a negligible contribution to B_{rms}.

Typically, the field distribution will not be solely due to the vortex lattice but will also contain (at least) a contribution from the nuclear dipole field. It is assumed that contributions to B_{rms} add in quadrature, so the behaviour of B_{rms} as a function of temperature is routinely fitted to a function such as

$$B_{\text{rms}}(T) = \left\{ B_0^2 \left[1 - \left(\frac{T}{T_{\text{c}}} \right)^{\alpha} \right]^2 + B_{\text{dip}}^2 \right\}^{\frac{1}{2}}, \tag{3.10}$$

where B_{dip} is the temperature-independent contribution from the nuclear dipole field. Equations 3.9 and 3.10 allow one to obtain $\lambda_{ab}(T)$, and the absolute value, $\lambda_{ab}(0)$. In addition, the functional form of $\lambda_{ab}^{-2}(T)$ can be related to the symmetry of the superconducting gap [95, 96], a fact I make use of in subsequent chapters.

Finally, it is worth noting that applying a field perpendicular to the inital muon polarisation usually requires some adjustment to the experimental setup compared to the ZF or LF cases. It is practically sensible to mount the coils that generate the applied field on the same plane as the detectors (see Figure 3.5) so, to apply a transverse field, one must either rotate the detectors by 90°, and therefore the coils also, or rotate the initial beam polarisation before it reaches the sample. Either way, the detectors end up on either side of the sample (with respect to beam direction) rather than in front of and behind it. That said, the asymmetry function is still defined as the normalised difference between the counts in these detectors.

3.3.5.4 Muon sources and spectrometers

During this project, I carried out μSR expperiments at two facilities: the ISIS Muon Facility at the Rutherford Appleton Laboratory, Oxfordshire, UK and the Swiss Muon Source (SμS) at the Paul Scherrer Institut (PSI), Villigen, Switzerland. These facilities offer different capabilities as they make use of pulsed and continuous sources respectively. I explain the difference between these in more detail in Appendix B, but it suffices to say here that a pulsed source offers a longer time window and a higher data collection rate than a continuous source, while a continuous source provides higher time resolution. Therefore, I chiefly studied intrinsic magnetic effects, such as magnetic order or spin fluctuations, at PSI as these phenomena tend to produce faster muon precession frequencies. By contrast, the long time window available at ISIS meant that I typically studied vortex lattice effects in superconductors at this facility, as I could resolve oscillations out to longer times here and so was able to obtain a more accurate value of the damping rate.

Principally, I used the MuSR spectrometer at ISIS and the GPS spectrometer at PSI for this work, though I also used the GPD spectrometer at PSI to study samples under pressure (Chapter 7). GPD makes use of decay muons (see Appendix B) which have higher energies than those used in the MuSR or GPS systems, and this allows them to penetrate larger samples, such as those housed in pressure cells.

This concludes my introduction to all the techniques used to prepare and study samples of the compounds discussed in this thesis. My work on $\mathrm{NaFe}_{1-x}\mathrm{Co}_x\mathrm{As}$, in particular, made use of most of these techniques and so it is to this system that I now turn.

Chapter 4

The gradual destruction of magnetism in $\mathrm{NaFe}_{1-x}\mathrm{Co}_x\mathrm{As}$

4.1 Introduction

The 111 compound NaFeAs is only a weak superconductor ($T_\mathrm{c} = 9\,\mathrm{K}$, with a volume fraction of less than 10%) in its stoichiometric form, but the presence of long-range magnetic order below $T_\mathrm{N} = 45\,\mathrm{K}$ and a tetragonal-to-orthorhombic structural transition at $T_\mathrm{s} = 55\,\mathrm{K}$ [13] make it a typical pnictide parent compound (see Chapter 2). As is the case, for instance, in $\mathrm{BaFe_2As_2}$, it was found that substituting small amounts of Fe for Co or Ni suppressed the magnetic state in NaFeAs and promoted superconductivity, raising T_c up to a maximum of 21 K [12]. The authors of Reference [12] also proposed a phase diagram for the $\mathrm{NaFe}_{1-x}\mathrm{Co}_x\mathrm{As}$ system, and this is reproduced here in Fig. 4.1.

This chapter describes my work in adding to this phase diagram by greatly increasing the number of samples studied. In particular, I focussed on the early part of the series ($0 \leq x \leq 0.025$) as this is where the magnetic and superconducting phases interact.

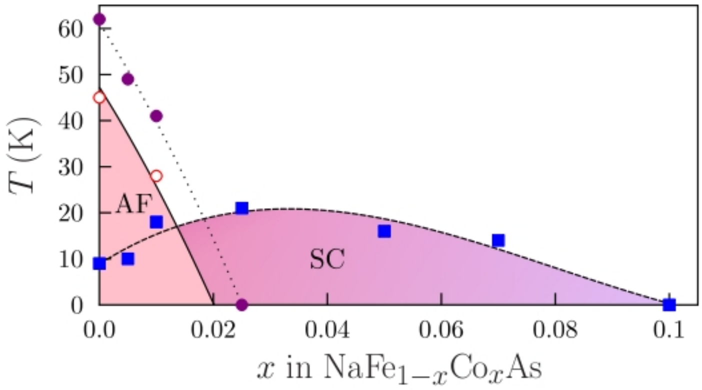

FIGURE 4.1: The original phase diagram of $\mathrm{NaFe_{1-x}Co_xAs}$, showing regions of superconductivity (marked by filled squares), magnetism (open circles) and the structural transition (filled circles). Figure taken from Reference [12].

As I have established, the exact nature of the interplay between these phases – whether they compete, coexist or exclude one another – is an important issue across the field of unconventional superconductivity in general.

Following a brief description of how such samples are synthesised, I will discuss the mapping out of the superconducting phase using SQUID magnetometry (something that also helped in sample characterisation). Once the evolution of the superconducting phase, parameterised by the transition temperature and volume fraction, was understood as a function of x, μSR was used to analyse the corresponding evolution of the magnetic phase. As the structural transition in pnictides is generally thought to be magnetically-driven (see Chapter 2), synchrotron XRD was then used to explore its dependence on Co substitution and learn more still about the relationship between magnetism and superconductivity. The chapter ends with an updated description of the phase diagram (Fig. 4.13) and a summary of my main findings. The work described in this chapter is published in Reference [97].

4.2 Synthesis and characterisation of powder samples

To begin, the suite of samples belonging to this family had to be extended, with particular exphasis placed on increasing the number of available samples with $0 < x \leq 0.025$. All synthetic work was carried out according to the method published in Reference [12]: First, lumps of Na were freshly cut and mixed in the stoichiometric molar ratio with ground Fe, Co and As powders. This mixture was first sealed under Ar in a Nb tube (using an arc-welder) and heated to 300°C, being held at this temperature for a few hours. This initial reaction melts the Na with the As to form the NaAs alloy, which can then be re-ground with the other metals on removing from the tube. The resulting mix, now fully ground into a powder, was pressed into a pellet and sealed in a second Nb tube which was in turn sealed into an evacuated silica ampoule. This ampoule was heated up to 750°C and held here for 2 days, before being cooled to room temperature by switching off the furnace.

For this second heating stage, the furnace temperature was raised to 750°C at a typical rate of 1°C/min. Arsenic sublimes at around 600°C, so it was feared that heating too quickly may cause this sublimation to happen before any reactions had a chance to take place. Sealing under Ar, so the reaction took place under some pressure from the inert gas, minimised this risk. Cooling the product at the natural rate of a switched-off furnace was found to promote good crystallinity. This is generally advantageous for diffraction experiments; giving sharper Bragg peaks and more precise lattice parameters.

Resulting samples were found to be highly crystalline, lustrous black powders. Purity was confirmed using laboratory XRD, specifically using the PANalytical XPert Pro, described in Chapter 3. The diffraction patterns for new samples were compared with that published in Reference [13] and reproduced in Fig. 4.2. Common impurities (such

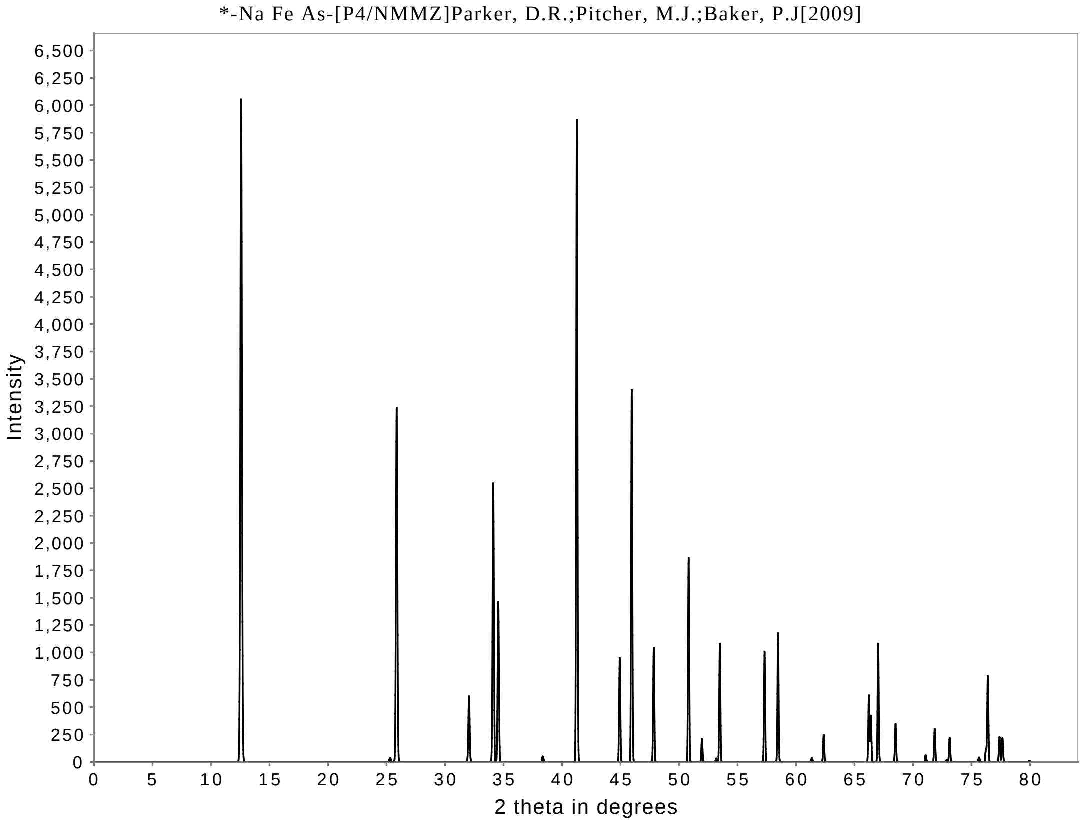

FIGURE 4.2: The powder pattern for NaFeAs, taken from the data published in Reference [13]. This pattern can be referred to when assessing the purity of newly synthesised members of the $NaFe_{1-x}Co_xAs$ family. For large values of x, one may notice a shift in peak position (corresponding to a lattice paramater shift) but no extra peaks will be observed unless there is an impurity.

as FeAs, CoAs, Na_3As) could be easily identified from any peaks not accounted for by the main phase, though none were observed in the samples subsequently discussed.

The Co concentration in pure samples was confirmed by comparing magnetic susceptibility and structural data from new compounds to the equivalent data published by Parker *et al.* [12]. An example of this characterisation method is demonstrated in Fig. 4.3, in which susceptibility data taken using the SQUID and lattice parameters obtained by Rietveld refinement against diffraction patterns taken using the XPert Pro diffractometer are shown in parts (a) and (b) respectively. In both parts of this figure, published data from the original series are represented by open circles, while data for a new composition (nominally $x = 0.015$) are represented by filled triangles. The data for the new composition fit well in amongst the published data, suggesting that an amount of Co close to the nominal value has indeed been incorporated into this new sample.

Using these synthesis and characterisation methods, a vastly expanded suite of high-quality samples with well-known compositions in the range $0 < x \leq 0.025$ was obtained. For this study, I prepared samples with $x = 0.0075$ and $x = 0.015$ and Dinah Parker (Inorganic Chemistry Laboratory, Oxford) prepared the remainder.

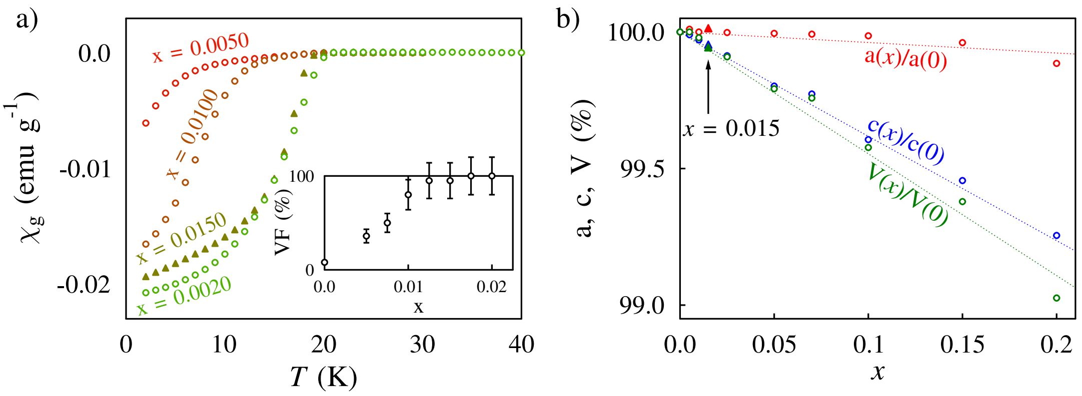

FIGURE 4.3: (a) The magnetic mass susceptibility, $\chi_g(T)$, data for selected members of the NaFe$_{1-x}$Co$_x$As series, measured using the SQUID in an applied field of 50 G. All samples were cooled in zero-field. T_c is measured as the onset of diamagnetism and the volume fraction (*Inset*) is estimated by taking the $x = 0.02$ sample to be fully superconducting, and comparing the values of $\chi_g(T \to 0)$ across the series. The data represented by open circles are taken from Reference [12], while the data represented by filled triangles are from a new compound (synthesised for this study) with $x = 0.015$. (b) The evolution of lattice parameters with x for the NaFe$_{1-x}$Co$_x$As series. Once again, data represented by filled triangles are for the $x = 0.015$ composition. By confirming that the susceptibility data and lattice parameters for the new compound lay on the trends established by published data, the stoichiometry of this compound was confirmed as far as available laboratory-based techniques allowed.

4.2.1 Mapping out the superconducting phase with SQUID magnetometry

In addition to confirming the stoichiometry of newly synthesised compounds, the values of both T_c and the superconducting volume fraction that I obtained for these compounds allowed me to update the superconducting region of the phase diagram. This is shown in

Fig. 4.4, which combines data from the original series with those from new compositions. The value of T_c was taken, in all cases, to correspond to the onset of diamagnetism in susceptibility data, and the size of the points in Fig. 4.4 are representative of the size of the error in this value. This figure demonstrates the growth of superconductivity with x in the low doping regime in far more detail than was given in Fig. 4.1, particularly as I have included information on the enhancement of the volume fraction, which is shown to be of great significance later in this chapter.

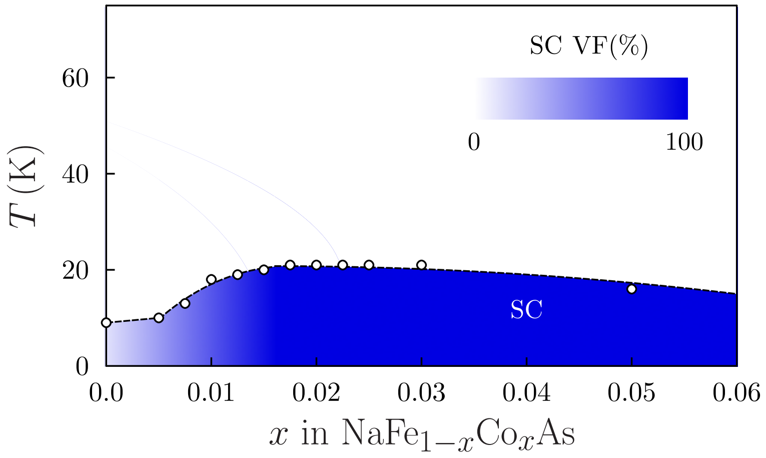

FIGURE 4.4: The updated superconducting region of the phase diagram, marked by data from the newly extended $NaFe_{1-x}Co_xAs$ series.

4.2.1.1 Aside: A note on superconducting volume fractions

A superconductor is expected to expel any and all applied fields from its interior as it is cooled below T_c. It does this by setting up surface currents to create a field that exactly opposes the applied field, giving a magnetic susceptibility equal to -1. Therefore, one may hope to estimate the superconducting volume fraction by comparing the value of $\chi(T \to 0)$ to -1. This approach fails, however, due to the so-called "demagnetising field". If a sample has non-zero bulk magnetisation, a field will be set up by effective north and south poles on opposite surfaces that opposes this magnetisation [98]. The effects of this are difficult to quantify as they intimately depend on the geometry of the sample. For arbitrarily shaped superconductors, the value of the moment measured by the SQUID (from which the susceptibility is calculated) will be different from the true value within the sample and so comparing the susceptibility to -1 is meaningless.

In practice, a sensible solution is to plot magnetic susceptibility data for a series of samples on the same graph, normalising by dividing each sample's susceptibility by its mass. If one can reasonably assume that the sample with the lowest (most negative) value of $\chi_{\mathrm{g}}(T \rightarrow 0)$ is fully superconducting, then one can estimate the volume fractions of the remaining samples by comparison. There is still uncertainty in this approach so a simple color gradient, rather than numerical values, is used to label volume fraction in Fig. 4.3(b). This graph then gives an indication of how the volume fraction grows on adding Co to NaFeAs, reaching 100% around $x = 0.015$.

4.3 Probing the magnetic phase with μSR

The zero-field muon asymmetry spectrum for undoped NaFeAs was found by Parker *et al.* to consist entirely of a set of oscillations at different frequencies [12]. This is clear evidence of long-range magnetic order (LRO) persisting throughout the entire sample [12, 13]. The critical exponent of the order parameter (any of these precession frequencies) was characteristically two-dimensional, and the estimated value of the ordered moment was low enough to explain the absence of magnetic Bragg peaks in the neutron diffraction data that had been obtained up to that point. They had also found that this moment, as well as the homogeneity of the order, was reduced in Co-substituted samples, but had only checked this with one concentration, $x = 0.01$. It was an aim of the present work to fully map out this phase using μSR.

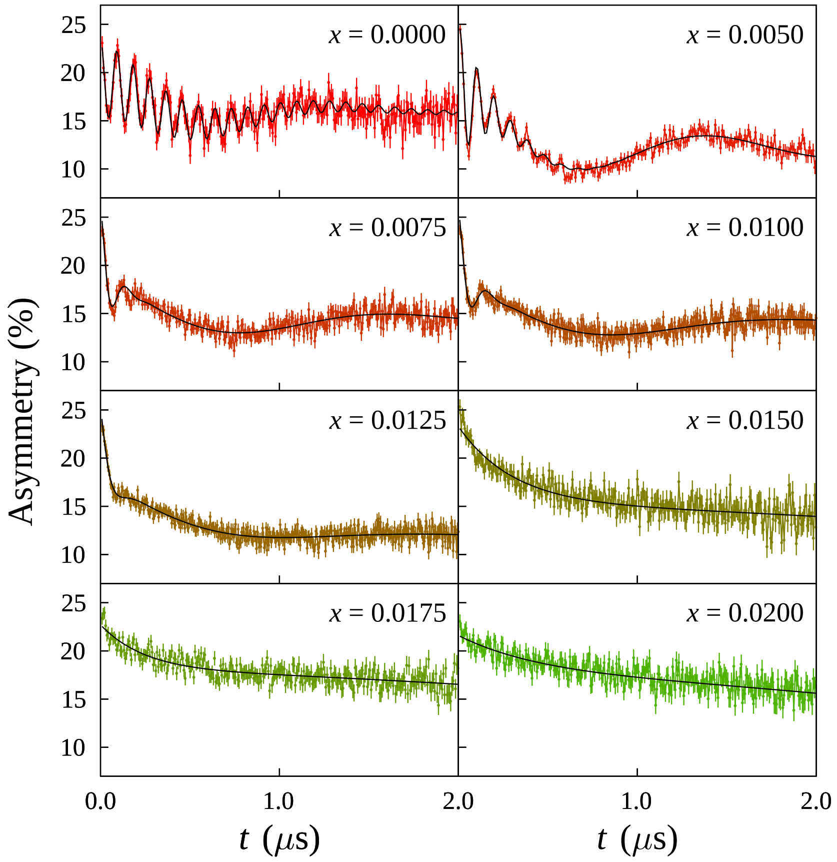

FIGURE 4.5: The ZF-μSR asymmetry spectra for all studied members of the NaFe$_{1-x}$Co$_x$As series, measured at 1.5 K. Oscillations, signatures of commensurate LRO, become more heavily damped, and have a lower frequency, as Co is added. They are absent beyond $x = 0.0125$, but a fast relaxation at early times persists up to $x = 0.02$.

Figure 4.5 shows the ZF data obtained at 1.5 K for eight samples with $0 \leq x \leq 0.02$. These data were taken using the GPS Spectrometer at PSI. A number of observations can be made by eye:

- The damping of the oscillations, due to disorder in the system, smoothly increases with x.

- The frequency of the oscillations, proportional to the ordered moment, smoothly decreases with x.

- Beyond $x = 0.0125$ no oscillations can be seen at all, suggesting that LRO is destroyed beyond this level of Co substitution.
- There is still an x-dependent signal, however, even beyond this concentration: a fast exponential relaxation at early times is visible for $0.015 \leq x \leq 0.02$, which again decreases in size as more Co is added.

Beyond $x = 0.02$ this fast relaxation at early times has also vanished, leaving an asymmetry spectrum best described by a temperature-independent Kubo-Toyabe function [see Fig. 3.6(b)]. This suggests that the system is paramagnetic beyond $x = 0.02$.

4.3.1 Long-range order: $0 \leq x \leq 0.0125$

To analyse data from the samples in question, two regimes were identified: the ordered ($0 \leq x \leq 0.0125$) and the disordered ($0.015 \leq x \leq 0.02$). For samples in the former, the data were fitted to

$$A(t) = \sum_i A_i \cos(\nu_i t) \mathrm{e}^{-\lambda_i t}, \tag{4.1}$$

where $\nu_i = \gamma_\mu (B_{\mathrm{local}})_i$. As the spectra in Fig. 4.5 suggest, at least two frequencies, one fast and one slow, were observed in each sample. This suggests that the structure accommodates two muon sites, as appears to be the case in other pnictides [99]. In undoped NaFeAs ($x = 0$), a second slow frequency was observed that was not present in the samples containing Co, suggesting that the undoped sample accommodates a third muon site. The absence of this in Co-doped samples may be because the third site becomes unstable following the structural changes induced by Co substitution, combined with increased magnetic disorder making a third frequency difficult to resolve. It should be noted that, in all cases in this ordered regime, the function in Eq. 4.1 accounted for the entire signal, so these samples are ordered over their entire volume. The fact that a significant superconducting volume fraction was also seen, particularly in the $x = 0.01$ and 0.0125 samples, implies a microscopic coexistence of these phases.

The questions surrounding possible coexistence of magnetic and superconducting phases – if it is possible and over what length scale – are some of the most hotly debated in the field of Fe-based superconductivity, and the situation seems to vary from system to system. For instance, there appears to be a sharp, first-order boundary between the two phases in $\mathrm{LaFeAsO}_{1-x}\mathrm{F}_x$ [7] while in $\mathrm{Ba}_{1-x}\mathrm{K}_x\mathrm{Fe}_2\mathrm{As}_2$ there appears to be a mesoscopic phase separation between regions of short-range or incommensurate magnetism and regions of superconductivity [100]. In the latter report, the authors make their arguments based on volume fractions calculated from μSR data, as we have done to argue for coexistence on an atomic scale in $\mathrm{NaFe}_{1-x}\mathrm{Co}_x\mathrm{As}$. However, the authors of Reference [101] point out, the muon is sensitive to the dipolar fields produced by moments in neighbouring unit cells, meaning that one cannot argue for true atomic-scale coexistence from μSR data alone. That said, they do argue for atomic-scale coexistence of incommensurate magnetism and superconductivity in $\mathrm{Ba(Fe}_{0.94}\mathrm{Co}_{0.06})_2\mathrm{As}_2$ based on NMR data.

Figure 4.6 plots the evolution of the largest frequency in each of the ordered samples with temperature. Proportional to the ordered moment, muon precession frequencies act as order parameters for the magnetic phase and so the ordering temperature, T_{N}, is defined as that at which this frequency goes to zero. This, along with the volume fraction estimates, allowed me to add regions of magnetic order and coexistence to the phase diagram and this is shown in Fig. 4.7. Note that the magnetic state has been labelled as antiferromagnetic (AF – hence the Néel temperature, T_{N}). Neutron scattering studies

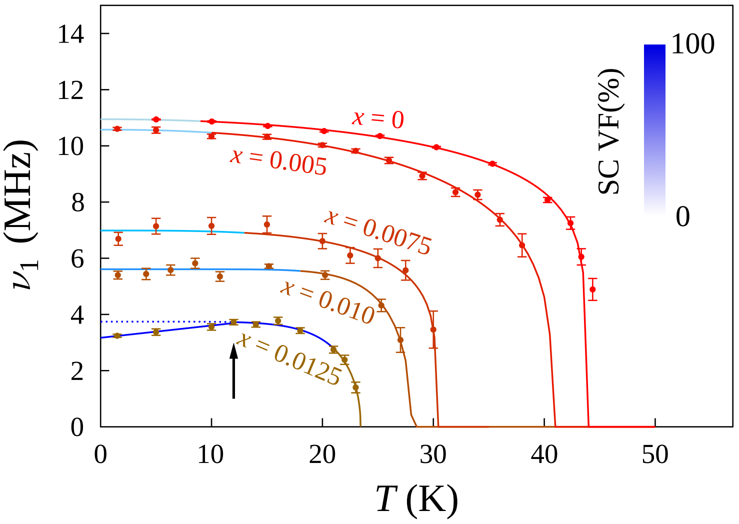

FIGURE 4.6: The evolution of the largest muon precession frequency with temperature across the ordered regime. Both T_N and $\nu_1(T \to 0)$ are reduced as x increases. The temperatures at which the samples exhibit superconductivity are shown in blue, and the shade of blue indicates the corresponding volume fraction. Note the suppression of the moment below T_c (black arrow) in the sample with the largest superconducting volume fraction.

[102] suggest that NaFeAs exhibits the same kind of stripy antiferromagnetic order as the other pnictides (see Fig. 2.4), albeit with a smaller moment on the Fe site: The authors of Reference [102] extract $\mu_{Fe} = 0.09(4)\,\mu_B$ for NaFeAs, compared with $\mu_{Fe} = 0.87(3)\,\mu_B$ for $BaFe_2As_2$ [48].

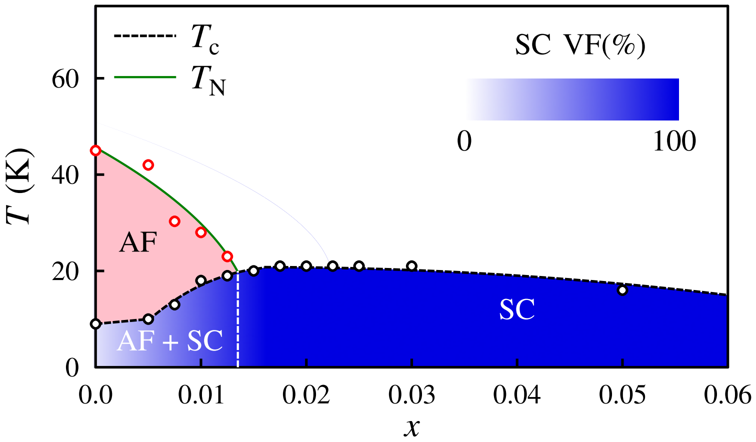

FIGURE 4.7: The ordered magnetic and superconducting regions of the phase diagram, along with a region of probable coexistence.

Figure 4.6 also clearly shows the aforementioned reduction in muon precession frequency [specifically $\nu_1(T \to 0)$] as Co concentration is increased, and this corresponds to a reduction in the size of the ordered moment. It is desirable to extract, from the behaviour of $\nu_1(T \to 0)$, a quantitative relationship between the ordered moment and x. This is directly calculable if one knows where the muons are in the cell: the values of the local fields they experience (calculated from their precession frequencies) enable one to infer the magnetic structure, or at least come up with some possible candidate structures that could produce those fields at those locations. However, the locations of the muon sites are generally unknown. While one can model the electrostatic interactions likely to occur within a given unit cell, this can be time-consuming and the results are hard to verify directly.

To proceed, then, I took a probabilistic approach. The object of interest is the conditional probability, $P(\mu|\{\nu_i\})$, of obtaining a certain ordered moment, μ, given the set of observed frequencies, $\{\nu_i\}$. While incalculable directly without knowing the muon locations, one can use Bayes' theorem to obtain this probability if one first finds $P(\{\nu_i\}|\mu)$ [103]. This second probability was found by assuming a stripy antiferromagnetic structure in accordance with the results of the aforementioned neutron scattering experiments [102]. The unkown muon locations were constrained to avoid occupied atomic sites, and to preferentially sit close to the negatively-charged (formally As^{3-}) anions. A moment size of $1\,\mu_{\mathrm{B}}$ was initially placed on each Fe site to facilitate the dipole field summation that produced $P(\{\nu_i\}|\mu)$. Using Bayes' theorem with the actual measured frequencies then allowed me to obtain $P(\mu|\{\nu_i\})$, and this distribution is shown in Fig. 4.8(a)*(Inset)*. From this, the size of the ordered moment on the Fe site was estimated to be $\mu_{\mathrm{Fe}} = 0.10(3)\,\mu_{\mathrm{B}}$, which agrees with the value of $0.09(4)\,\mu_{\mathrm{B}}$ given in Reference [102].

Having found a way of converting precession frequencies into a value for the ordered

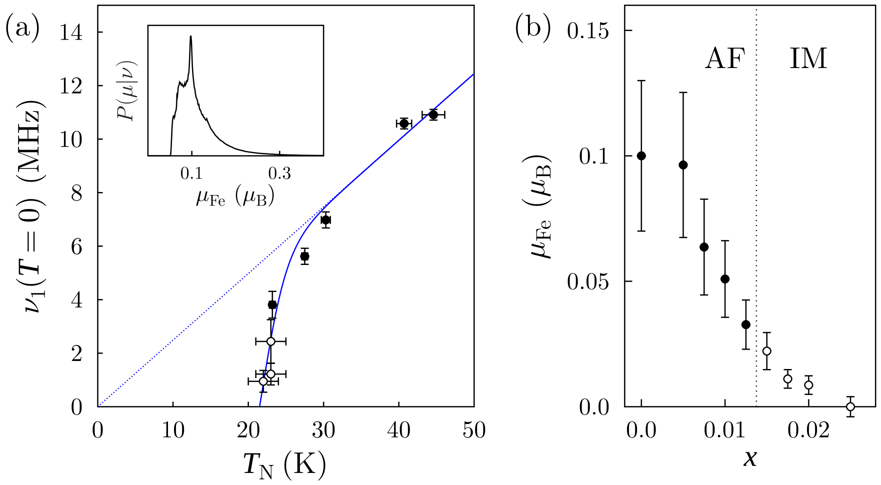

FIGURE 4.8: The gradual destruction of magnetism in $NaFe_{1-x}Co_xAs$ through a suppression of the ordered moment: (a) the precession frequency $\nu_1(T \to 0)$ vs Néel temperature T_N for ordered samples (filled circles). Also shown is the behaviour of an effective precession frequency, estimated from the magnetic contribution to the damping of oscillations in a transverse-field experiment, for the samples with $0.015 \le x \le 0.02$. For these samples, "T_N" is the onset temperature of this magnetic contribution. *Inset*: the probability distribution of possible moment sizes, given the observed set of frequencies in NaFeAs, calculated by dipole field summation. (b) A quantitative estimate of the moment size reduction with x, obtained using the precession frequency behaviour and $P(\mu|\{\nu_i\})$.

moment in NaFeAs, it was now straightforward to calculate the moment size in all ordered samples, and this is shown in Fig. 4.8(b). It seems that a suppression of the moment size is responsible for the destruction of the magnetic state, as emphasised by the fact that $\nu_1(T \to 0)$ tends to zero quicker than T_N [Fig. 4.8(a)].

Figure 4.8 also includes the results of the analysis of samples with no LRO ($0.015 \le x \le 0.02$), but before discussing those it is worth noting one more feature of the data for $NaFe_{0.9875}Co_{0.0125}As$. Of all the ordered samples, this is the one with the highest superconducting volume fraction and transition temperature (see Fig. 4.7), so it is interesting to note a suppression of the precession frequency in this sample when it is in a superconducting state. This is highlighted by the black arrow in Fig. 4.6. This suppression of the magnetic order parameter is an indication of the direct competition between magnetism and superconductivity, and further suggests that they must coexist at some level in order to compete. It is also reminiscent of what is seen in other Fe-based superconductors (see, for instance, Reference [104]).

4.3.2 Inhomogeneous magnetism: $0.015 \leq x \leq 0.02$

Returning to the ZF asymmetry spectra in Fig. 4.5, one notices that even when no oscillations can be resolved (i.e. $x > 0.0125$), there is still a fast exponential relaxation at early times that gets weaker as x is increased. This is superimposed upon the slow Gaussian Kubo-Toyabe relaxation that remains beyond $x = 0.02$, so the samples with $0.015 \leq x \leq 0.02$, although not ordered, do display an emergent magnetic state.

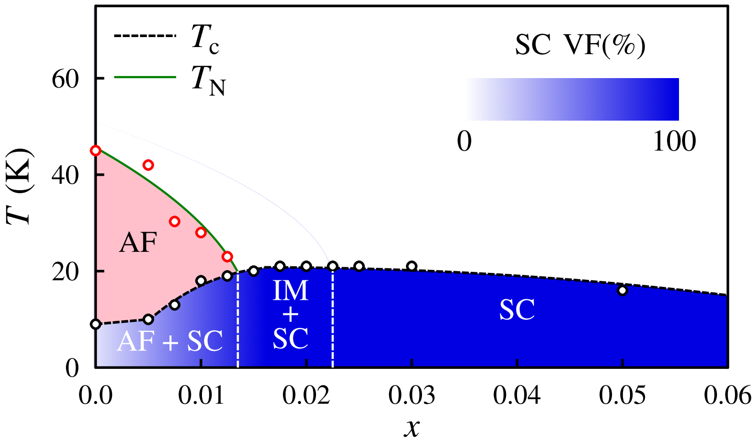

FIGURE 4.9: Phase diagram showing regions of ordered and inhomogeneous magnetism, as well as superconductivity.

The spectra for the three samples in this regime were best decribed by the function

$$A(t) = A_{\rm slow} G_{\rm KT}(\Delta, t) + A_{\rm fast} \exp(-\lambda_{\rm f} t), \tag{4.2}$$

where $A_{\rm fast}$ and $\lambda_{\rm f}$ are the amplitude and rate of the additional relaxing component respectively. Two components adding in this way indicates that while a fraction of muons $[A_{\rm fast}/(A_{\rm fast}+A_{\rm slow})]$ experience the effects of this magnetic state, the remainder feel only the nuclear dipole field. Thus, the sample has separated into mesoscopic regions of both local order and paramagnetism. The fraction of muons sitting in regions of local order decreases as x increases (from around 3/4 for $x = 0.015$ to 1/4 for $x = 0.02$) suggesting that the extent of these regions is being diminished as more Co is added. Samples are fully superconducting throughout this regime, again suggesting that these phases coexist. These observations allowed me to add a region of inhomogeneous magnetism (IM) to the phase diagram, as shown in Fig. 4.9.

In order to extract more information about this phase, transverse-field (TF) μSR was used to measure the breadth of the field distribution, B_{rms}, directly (see Chapter 3). In this case, three contributions to B_{rms} were expected: from the vortex lattice, the nuclear field and the IM phase. The second of these is assumed to be small and temperature-independent, but the others should change with both T and x, and in very different ways. It was hoped that their contributions could be separated, allowing the interaction of these phases to be monitored directly.

Figure 4.10 shows the evolution of B_{rms} with temperature for all three samples in the IM regime, as well as that for the paramagnetic superconductor NaFe$_{0.975}$Co$_{0.025}$As. These data were taken using the MuSR Spectrometer at the ISIS Facility. For the $x = 0.015$ sample, a peak in B_{rms} was observed at around 17 K that coincides with a peak in the amplitude, A_{fast}, of the IM signal observed in zero-field (see Eq. 4.2). This confirms that B_{rms} does indeed contain a contribution from the IM phase. The size of this contribution is clearly reduced as x increases and the extent of the local ordered regions decreases.

Assuming the SC and IM contributions to B_{rms} add in quadrature, and the SC contribution does not vary with x, one can isolate the width of the IM field distribution. The relationship between field and frequency ($\Delta\nu = \gamma_\mu B_{\text{rms}}$) was then used to estimate the

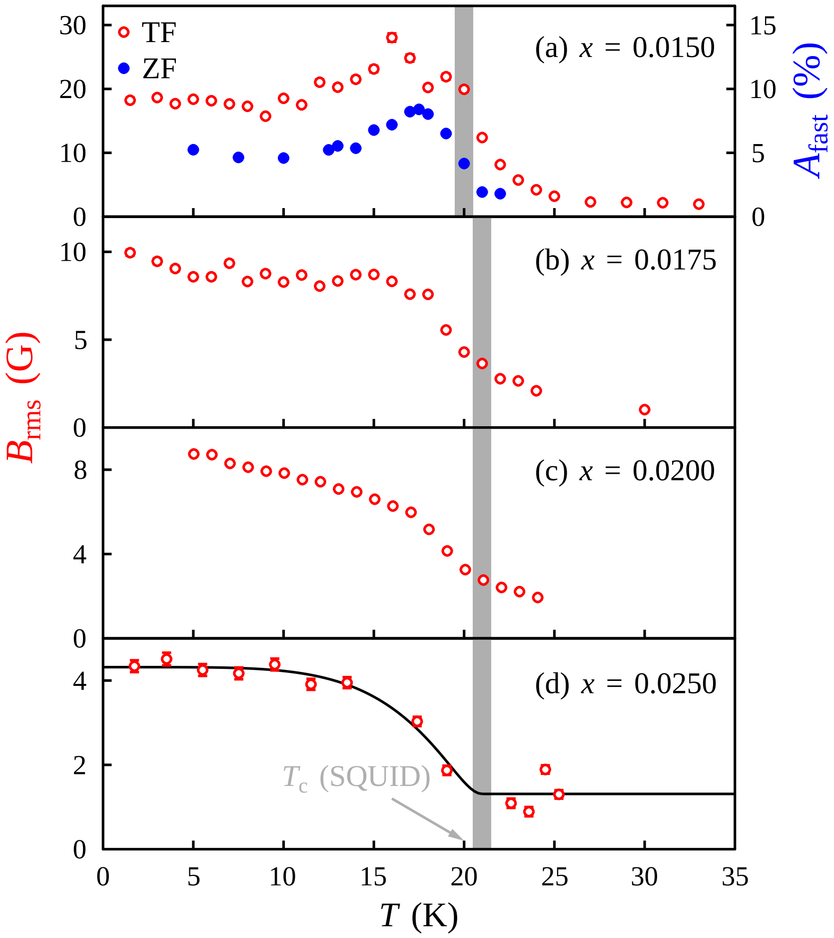

FIGURE 4.10: TF-μSR data for samples in the IM phase [(a)–(c)], as well as for a fully superconducting, non-magnetic sample (d). All data were taken in an applied transverse field of 100 G The local order clearly contributes to B_{rms} and is diminished as x increases.

rate at which muons would have precessed if these samples had been fully ordered; these are plotted as open circles in Fig. 4.8. For this graph, the value of the ordering temperature was simply taken as the onset of the magnetic contribution to B_{rms} from Fig. 4.10. In Fig. 4.8(b) the relationship between frequency and moment has been used to estimate the size of the latter in the IM phase. The size of this now disordered moment continues to decrease as Co is added, continuing the trend established in the ordered phase.

4.4 The structural distortion

In accordance with what is seen in other systems, the authors of Reference [12] had observed a tetragonal-to-orthorhombic ($P4/nmm$ to $Cmma$) structural distortion in NaFeAs and NaFe$_{1-x}$Co$_x$As samples up to $x = 0.025$. Once again, the aim here was to extend their work and study more samples in this early part of the phase diagram. As the structural distortion is believed to be magnetic in origin (see Chapter 2), I hoped to learn more about the magnetic states in these systems, and their relationships to the superconducting phase, by studying the structural distortion in detail. This work was carried out on the ID31 Beamline at the ESRF.

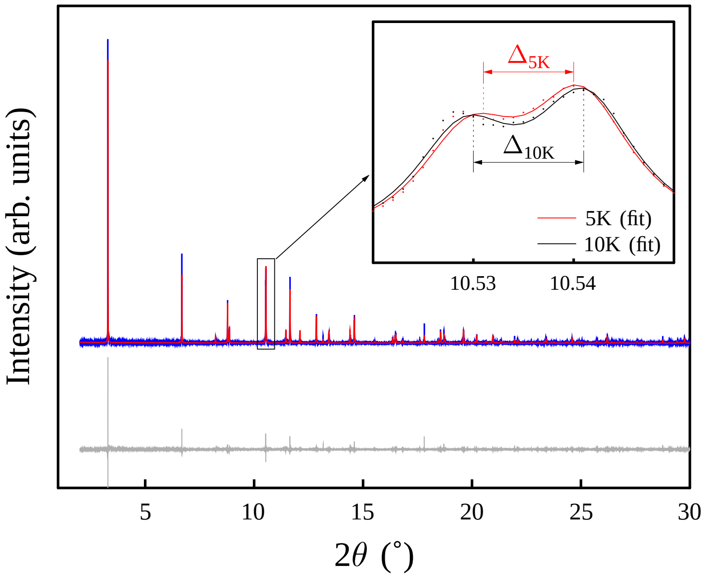

FIGURE 4.11: The synchrotron XRD data for NaFe$_{0.98}$Co$_{0.02}$As with a fit obtained from Pawley refinement. *Inset:* A comparison of the 022 and 202 peaks in $Cmma$ at 5 K and 10 K. On undergoing the orthorhombic distortion, the 122 peak in $P4/nmm$ splits into these two peaks, so the difference in their 2θ values, Δ_T, is a structural order parameter. $\Delta_{5\,\mathrm{K}} < \Delta_{10\,\mathrm{K}}$, meaning that the distortion is suppressed on cooling in this sample.

A typical data set, in this case for NaFe$_{0.98}$Co$_{0.02}$As, is shown in Fig. 4.11. The orthorhombic unit cell parameters are related to their tetragonal counterparts like so:

$a_{\text{orth}} = \sqrt{2}a_{\text{tet}} + \delta$, $b_{\text{orth}} = \sqrt{2}a_{\text{tet}} - \delta$, $c_{\text{orth}} = c_{\text{tet}}$. The parameter δ goes to zero at the structural transition temperature, T_{s}, when the two unit cells become equivalent descriptions of the same tetragonal symmetry. The behaviour of δ with temperature was obtained using a model-independent Pawley refinement[1] (see Chapter 3 and Appendix A). Fig. 4.12 shows the evolution of $\delta(T)$ for all samples measured.

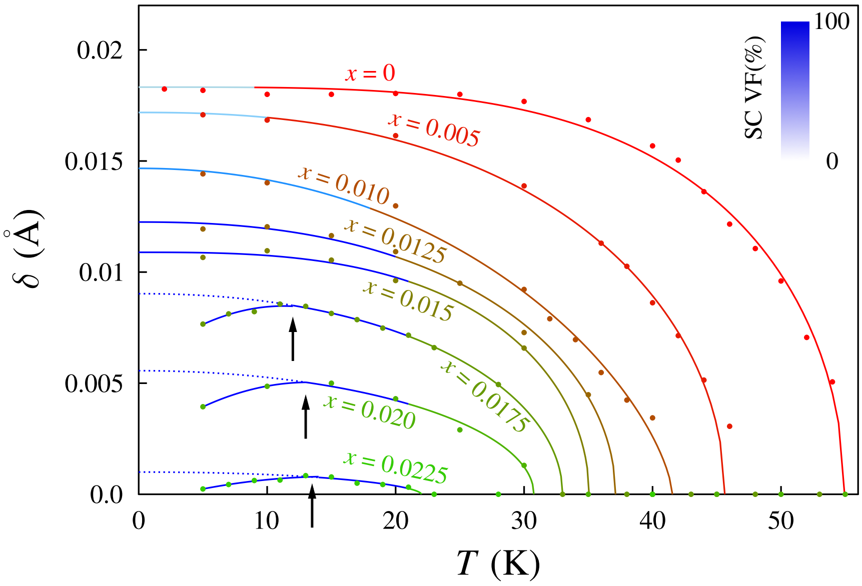

FIGURE 4.12: The evolution of the structural order parameter, δ (defined in the text), with temperature for all samples studied. $\delta(T \to 0)$ and the transition temperature, T_{s}, go down with x, and I observe a suppression of δ at low-T in fully superconducting samples below T_{c} (black arrows).

The size of the structural distortion (the magnitude of δ) clearly decreases as x increases, following the destruction of the magnetic phase. In addition, a low-T suppression of δ was observed in the most superconducting samples. This is noticeable even by eye, as shown in the inset to Fig. 4.11: the splitting of the tetragonal 122 peak into the orthorhombic 022 and 202 peaks is reduced on cooling to 5 K from 10 K. This is reminiscent of the suppression of the magnetic order parameter in $NaFe_{0.9875}Co_{0.0125}As$ (see Fig. 4.6) and similar behaviour is observed in other systems [5]. It is also worth noting that a clear

---

[1] The preferred orientation of plate-like crystallites in $NaFe_{1-x}Co_xAs$ powder gives the $(00l)$ peaks extra intensity that can be difficult to model during Rietveld refinement. As only the lattice parameters were of interest anyway, Pawley refinement was thus chosen over Rietveld refinement to avoid this problem.

structural distortion is observed even in samples which are not fully ordered magnetically, although only in those that contain some emergent magnetic phase. Thus, the structural distortion must be driven by magnetic fluctuations, rather than magnetic order.

A theoretical picture that accounts for these observations is provided by Fernandes *et al.* [105]. Motivated by the stripy structure of the AFM phase, these authors propose the emergence of a so-called "nematic" phase which biasses the magnetic fluctuations above T_N along a particular stripe orientation. Crucially, the nematic order parameter couples to the lattice and causes the bonds between neighbouring (anti)parallel spins to (expand) contract. Thus the nematic phase "sets the scene" for the magnetic phase it anticipates and the structural transition is something of a side-effect. Because the nematic phase does not require magnetic order, requiring only a finite spin correlation length, the structural transition can also occur in samples with no ordered phase and at temperatures significantly above T_N.

This scheme also accounts for the low-T suppression of magnetic and structural order parameters in the most superconducting samples. Specifically, the onset of superconductivity is predicted to lead to a reduction in the static part of the magnetic susceptibility [105] which weakens the magnetic order and spin correlations. Again I emphasise that suppression only occurs in samples with a (near) full superconducting volume fraction and at temperatures well below the superconducting T_c, where a strong superconducting order parameter is established.

Finally, the data in Fig. 4.12 were fitted to $\delta(T) = (1 - (T/T_\mathrm{s})^\alpha)^\beta$ to obtain estimates for T_s. This allowed me to complete the updated phase diagram shown in Fig. 4.13.

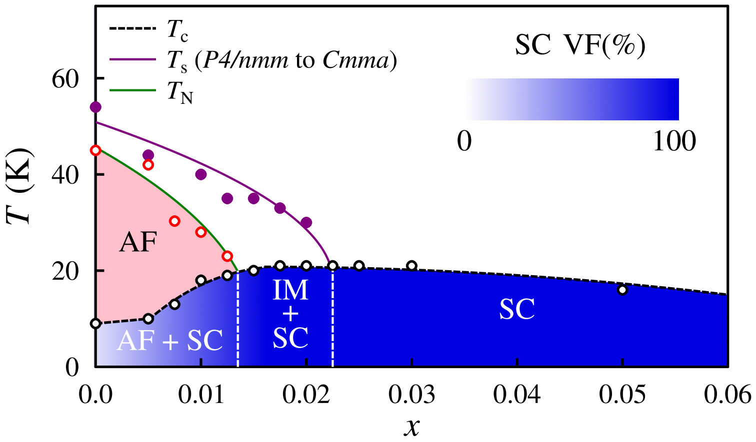

FIGURE 4.13: The updated phase diagram of $NaFe_{1-x}Co_xAs$, showing regions of superconductivity, magnetism and coexistence, as well as the structural transition.

4.5 Discussion: the phase diagram revisited

The approach of studying superconducting, magnetic and structural properties systematically on an extensive suite of $NaFe_{1-x}Co_xAs$ has greatly enriched the understanding of this system. This work has revealed how the superconducting state is steadily enhanced, both in transition temperature and volume fraction, as Co is substituted for Fe. Correspondingly, the magnetic state is gradually destroyed, primarily through a suppression of the ordered moment. It is suggested that the growing superconducting state also weakens spin correlations [105], explaining how the ordered state breaks up into mesoscopic regions of local magnetic order beyond $x = 0.0125$. Adding more Co further suppresses the moment size even in these locally ordered regions, which also become successively smaller. The structural distortion is driven by a nematic phase coupling to magnetic fluctuations, so I find a reduction in both T_s (following the reduction in T_N) and the size of the distortion. The competition between coexisting magnetic and superconducting phases is revealed most clearly by the low-T suppression of magnetic and structural order parameters in the most superconducting samples, and is again a consequence of the superconducting state weakening spin correlations.

As discussed in Chapter 2, the precise mechanism by which Co substitution drives these changes is under debate. The authors of Reference [106] find that the Fermi surface of NaFeAs is at least qualitatively similar to that of $BaFe_2As_2$ [65], and the phase diagram [5] of $Ba(Fe_{1-x}Co_x)_2As_2$ is also very similar to that in Fig. 4.13 (also see Fig. 2.5). Because of this, I suggest that Co acts as an electron donor in $NaFe_{1-x}Co_xAs$ as it seems to in the 122 compound [81]. Band filling disrupts the nesting condition that drives magnetic order by altering the relative sizes of the electron and hole pockets on the Fermi surface, and this allows superconductivity, mediated by the residual spin fluctuations, to emerge in its place.

There is one unresolved part of this picture that is worth highlighting: the possibility of incommensurate (IC) order emerging on doping away from the parent compound. Neutron scattering measurements suggest a crossover from commmensurate to incommensurate (IC) AFM just as superconductivity emerges in $Ba(Fe_{1-x}Co_x)_2As_2$ [107] and $Ba(Fe_{1-x}Ni_x)_2As_2$ [108]. NMR measurements also support the idea of coexistence between superconductivity and IC-AFM in the former system [101]. No such equivalent experimental evidence currently exists for $NaFe_{1-x}Co_xAs$, probably due to the small moment size in this system making magnetic structure determination difficult. When interpreting my muon data, I did not elaborate on specific changes to the magnetic structure, merely noting an increase in disorder as Co is added. By this, I simply meant that the internal field distribution (a series of delta functions in the ideal commensurate case) is broadened by some magnetic inhomogeneity, and this could be a signature of incommensurate order. If the incommensurate propagation vector is as close to commensurate as the authors of Reference [107] suggest, then this picture becomes particularly plausible, and indeed similar muon spectra seen in $Ba_{1-x}K_xFe_2As_2$ have been interpreted as evidence for IC order [100]. If IC order were to be confirmed in $NaFe_{1-x}Co_xAs$ the only part of this investigation that would be affected is the magnetic structure assumption that went into the dipole field calculations. One would have to do a separate calculation for each sample, rather than using the same constant of proportionality between $\nu(T \rightarrow 0)$ and μ_{Fe} across the series, as I have done here. This procedure was carried out to quantify the dependence of the moment size on x, but the conclusion I drew from it – that magentism is destroyed primarily through a diminishment of this moment – was obvious from the dependence of $\nu(T \rightarrow 0)$ on x, and so this conclusion would remain true even in an IC picture. The only likely change would be in the precise form of $\mu_{\mathrm{Fe}}(x)$, and this change would probably be very minor.

In this chapter, I have described an extremely detailed set of data on an extensive series of samples. By successfully synthesising, along with my collaborators, compounds with compositions separated by very fine steps in Co concentration, I have been able to monitor the gradual evolution from a fully magnetic to a fully superconducting state in $\mathrm{NaFe}_{1-x}\mathrm{Co}_x\mathrm{As}$. Using a diverse but complimentary range of experimental techniques, and particularly μSR, I have observed how these states compete and coexist with one another as one moves across the phase diagram. From this work, I can conclude that $\mathrm{NaFe}_{1-x}\mathrm{Co}_x\mathrm{As}$ appears to resemble the more widely-studied members of other series, and notably $\mathrm{Ba(Fe}_{1-x}\mathrm{Co}_x)_2\mathrm{As}_2$. The theoretical picture based on a Fermi surface evolving (via band filling) away from the nesting that leads to magnetic order and towards a topology that supports spin fluctuation-mediated superconductivity is supported by my observations, as is the suggestion that the structural transition is driven by a nematic phase that also couples to spin fluctuations. To provide an interesting contrast, I now turn to a system that, unlike NaFeAs, routinely confounds theoretical predictions and seemingly stands alone amongst Fe-based superconductors: the isostructural LiFeAs.

Chapter 5

Superconducting and magnetic states in derivatives of LiFeAs

5.1 Introduction to LiFeAs

LiFeAs was first synthesised in 1968 [109], but only shown to be a superconductor (with $T_\mathrm{c} = 17\,\mathrm{K}$) 40 years later [43, 44, 110]. As well as being fully superconducting in its stoichiometric form, it was also quickly established that T_c can not be raised by substituting Fe for Co or Ni [14], as is the case in other systems. Instead, it appears that stoichiometric LiFeAs is "optimally electron-doped" with regards to superconductivity. Applied pressure has also been shown only to reduce T_c [111].

Furthermore, LiFeAs undergoes neither a structural transition nor one to a magnetically ordered phase [44], defying the predictions of early theoretical work [112–114]. However, inelastic neutron scattering (INS) measurements on superconducting [115, 116] and non-superconducting (apparently Li-deficient) [117] samples have demonstrated that LiFeAs does exhibit similar magnetic fluctuations to those seen in other systems; namely, antiferromagnetic (AFM) fluctuations close to the wave-vector $Q = (\pi, \pi, 2\pi)$. This reinforces the idea that LiFeAs resembles the optimally doped members of other pnictide families, and suggests that successfully hole doping LiFeAs may induce an ordered magnetic state.

No such state has yet been observed, and a range of anomalous experimental results [15, 118–124] have led some to propose that LiFeAs is a separate and fundamentally different system from other Fe-based superconductors. Most of these ideas concern the pairing symmetry of the superconducting state. The authors of Reference [125], for instance, suggest that LiFeAs may exhibit triplet pairing driven by ferromagnetic (FM) fluctuations, as opposed to the antiferromagnetic fluctuations that appear to govern superconductivity in related compounds. Despite the INS results, such ideas about triplet pairing persist in the literature, fuelled by unusual Knight shift results [120, 121] and calculations that place LiFeAs close to both AFM and FM instabilities [126].

While the debate surrounding this compound continues, it remains vital to obtain as much detailed experimental information as possible. This chapter describes my work on three derivatives of LiFeAs: $\mathrm{LiFe}_{1-x}M_x\mathrm{As}$ (M = Co or Ni) and $\mathrm{Li}_{1-y}\mathrm{Fe}_{1+y}\mathrm{As}$. For the transition metal substituted series', TF-μSR was used to track the evolution of the penetration depth with doping, and I demonstrate how this can be related to the corresponding evolution of the Fermi surface. For the Fe-rich series, low-field DC magnetometry and μSR were used to explore some unusual emergent magnetic properties that may be intimately connected to the aforementioned multiple magnetic instabilities in LiFeAs.

The results of these investigations, along with key results from the literature, are summarised in Table 5.2. This table attempts to capture the key parts of the ongoing controversy concerning LiFeAs, demonstrating just how much apparently conflicting evidence the study of this compound has produced, and the challenge any successful theory of LiFeAs must overcome in order to reconcile these conflicts. The question is: Is LiFeAs equivalent to the optimally electron-doped pnictides, or is it fundamentally different? I will conlude this chapter by discussing how my results may inform the answer to this question.

5.2 Synthesis and characterisation of powder samples

All of the samples discussed in this chapter were made and characterised by Michael Pitcher and co-workers in the Inorganic Chemistry Laboratory, Oxford. In Reference [14] the authors present a detailed account of how this was achieved, so only a brief summary of the procedure is given here.

Polycrystalline samples of LiFeAs derivatives were prepared as follows: Freshly cut lumps of Li were mixed with a ground combination of transition metals and As in a stoichiometric ratio. This mixture was sealed under Ar in an arc-welded Nb tube and heated to 225°C, being held there for a few hours and then removed from the furnace. The resulting mix of LiAs alloy and transition metals was then further ground before being pressed into a pellet and sealed in a second Nb tube under Ar. This was sealed in an evacuated silica ampoule and heated up to 800°C at a rate of 1°C/min. After being held there for 2 days the furnace was switched off and allowed to cool naturally to room temperature. This procedure is very similar to that of the isostructural NaFeAs derivatives and is motivated by similar concerns, which are discussed in Chapter 4.

The compositions of the resulting samples were confirmed using a combination of laboratory and synchrotron XRD, and well as high-resolution neutron powder diffraction (NPD). In addition to the usual lattice parameter study, NPD allowed Pitcher *et al.* [14] to model the concentration of substituted atoms explicitly in their Rietveld refinements. Studies of substitution-dependent T_c were carried out using the SQUID, like those I performed for my NaFe$_{1-x}$Co$_x$As samples, and measurements of field-dependent magnetisation at room temperature were obtained to rule out the presence of magnetic impurities. This extensive combination of techniques allowed for the creation of three very well-characterised series' of samples: LiFe$_{1-x}M_x$As (M = Co, Ni; $x \leq 0.2$) and Li$_{1-y}$Fe$_{1+y}$As ($y \leq 0.04$).

5.3 The penetration depth of superconducting LiFe$_{1-x}M_x$As (M = Co, Ni)

In 1989, Y. J. Uemura *et al.* [127] found a correlation between the measured values of T_c and the quantity $\lambda_{ab}^{-2}(T = 0)$ for sixteen different cuprate samples, where λ_{ab} is the London penetration depth in the crystallographic *ab*-plane. This was interpreted as a scaling between T_c and n_s/m^* (superconducting carrier density over effective carrier mass), following the London relationship $\lambda_{ab}^{-2} \propto n_s/m^*$. Two years later [128], they added results for compounds belonging to other classes of unconventional superconductors to this so-called "Uemura plot" and found that they also shared this correlation, while conventional superconductors did not. This revealed that there must be some common feature shared by non-BCS systems that any successful theory of these materials must account for. It has since become common practice to place novel systems on the Uemura plot in an attempt to classify them and, more recently [17], the same group demonstrated that some Fe-based superconductors obey Uemura scaling.

In this section, I describe my own μSR studies of the penetration depth of members of the $\mathrm{LiFe}_{1-x}M_x\mathrm{As}$ (M = Co, Ni) series. Working with some of Michael Pitcher's early LiFeAs samples, colleagues in my research group had previously found that the undoped system did not lie on the Uemura trend established by the hole-doped cuprates, but rather followed a slightly different line established by the electron-doped cuprates [15]. This may be another result that suggests a fundamental difference between LiFeAs and other Fe-pnictides. I was interested in exploring this result further by examining the effects of Co and Ni substitution on the penetration depth, and how these substitutions affected the Uemura scaling in LiFeAs derivatives.

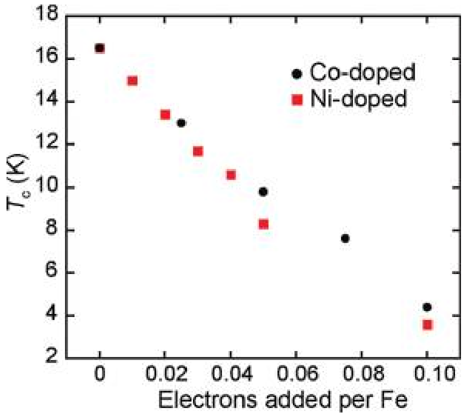

Figure 5.1: The evolution of T_c with added electron concentration, assuming Co adds one electron to the band structure for every Fe replaced and Ni adds two. Figure taken from Reference [14].

Our samples were synthesised as described above and Fig. 5.1 (taken from Reference [14]) shows the evolution of T_c with the concentration of additional electrons added by these substitutions. As I did for $\mathrm{NaFe}_{1-x}\mathrm{Co}_x\mathrm{As}$, I suggest that the band filling scenario discussed in Chapter 2 is relevant for these LiFeAs derivatives, and Fig. 5.1 emphasises how the evolution of T_c can be understood as a consequence of simple electron doping: Ni substitution (which formally adds two electrons for every Fe atom replaced) has the same effect on the structure of LiFeAs as Co substitution (which adds one electron), but twice the effect on T_c [14]. Incidentally, the TF-μSR data described in this section are also published in Reference [14].

5.3.1 Transverse-field μSR measurements

All data presented in this section were taken on the MuSR Spectrometer at the ISIS Facility. Figure 5.2 shows the asymmetry spectra for the superconducting sample $\mathrm{LiFe_{0.99}Ni_{0.01}As}$ and this is a typical response; one can clearly see the damping below T_c (13.5 K) due to the vortex lattice broadening the field distribution. The applied field was 100 G and above T_c one sees oscillations at the corresponding frequency. Below T_c, one can see the oscillations are of a slightly lower frequency, and this is the diamagnetic shift that confirms the broadening is due to the vortex lattice and not some other magnetic effect (see Chapter 3).

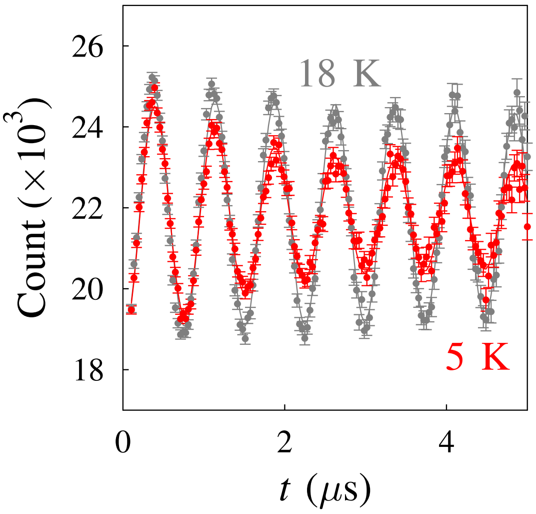

FIGURE 5.2: The asymmetry spectra for superconducting $\mathrm{LiFe_{0.99}Ni_{0.01}As}$ above and below $T_c = 13.5\,\mathrm{K}$. The decay-corrected positron count is shown on the y-axis, rather than an explicitly calculated asymmetry, due to a technicality of the data processing procedure that is not discussed, but it is equivalent to asymmetry here.

Similar spectra were obtained for all samples measured and were fitted to

$$A(t) = A_{\mathrm{bg}} \cos(\gamma_\mu B_{\mathrm{a}} t) \mathrm{e}^{-\sigma_{\mathrm{bg}}^2 t^2/2} + A_{\mathrm{s}} \cos(\gamma_\mu B_{\mathrm{pk}} t)\, \mathrm{e}^{-\sigma^2 t^2/2}. \tag{5.1}$$

The first component accounts for muons that have stopped in the sample holder; B_{a} is the applied field and is fixed throughout, along with the background depolarisation rate, σ_{bg}. The second component is from muons stopping in the sample; with $\sigma = \gamma_\mu B_{\mathrm{rms}}$ containing contributions from the vortex lattice and the nuclear dipole field.

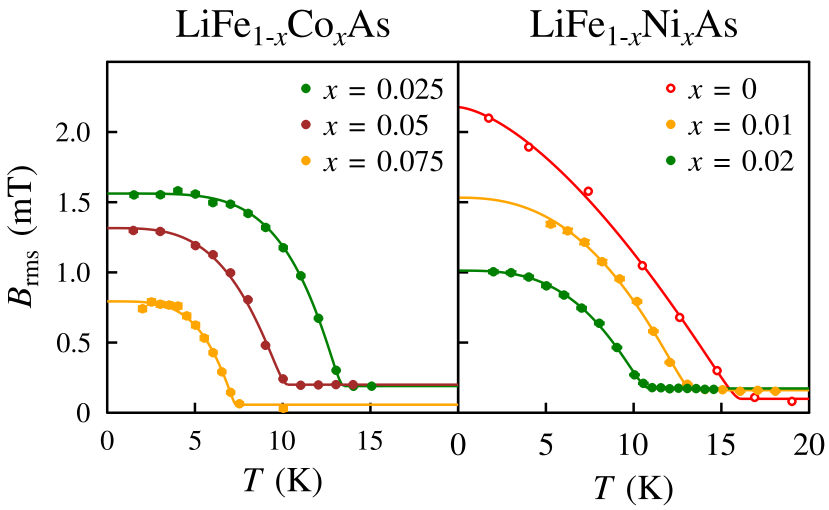

FIGURE 5.3: The temperature evolution of the vortex lattice broadening of the field distribution, B_{rms}, for all Co and Ni doped samples studied in the present work. The Figure is adapted from [14]. Also shown is the data for stoichiometric LiFeAs taken from [15]. From the variation in $B_{\mathrm{rms}}(0)$ with x, I have extracted the corresponding evolution of λ_{ab} using Eq. 3.9 (see Table 5.1). Also note that $B_{\mathrm{rms}}(T)$ saturates at low temperature in the doped compounds, but not in undoped LiFeAs.

Figure 5.3 shows the temperature dependence of B_{rms} obtained from the behaviour of the damping, σ, for all samples studied. Also shown for comparison is the data for undoped LiFeAs, taken from [15]. In all cases, these data were fitted to the phenomenological function given in Eq. 3.10 and these fits are also shown in Fig. 5.3. Using Eq. 3.9, the values of the penetration depth were then calculated, and these are given in Table 5.1. The values of $\lambda_{ab}^{-2}(0)$ are plotted against the corresponding values of T_{c} in the Uemura plot shown in Fig. 5.4. This unambiguously confirms that the entire LiFe$_{1-x}M_x$As series

(M = Co or Ni) lies some way off the Uemura line established by the hole doped cuprates, and instead lies closer to that established by electron-doped cuprates. Also highlighted in the Uemura plot is the observed reduction in $\lambda_{ab}^{-2}(0)$ as x is increased in both series, and I shall discuss what this reveals about the evolution of the Fermi surface with doping in the following section.

Sample	T_c (K)	$\lambda_{ab}(0)$ (nm)	$\lambda_{ab}^{-2}(0)$ (μm^{-2})
LiFeAs	17 (1)†	195 (2)	26.3 (3)
$\mathrm{LiFe_{0.975}Co_{0.025}As}$	13.52 (12)	218 (2)	21.1 (2)
$\mathrm{LiFe_{0.95}Co_{0.05}As}$	10.0 (1)	240 (8)	17.4 (6)
$\mathrm{LiFe_{0.925}Co_{0.075}As}$	7.35 (5)	303 (6)	10.9 (2)
$\mathrm{LiFe_{0.99}Ni_{0.01}As}$	13.41 (8)	218 (9)	21.0 (9)
$\mathrm{LiFe_{0.98}Ni_{0.02}As}$	10.93 (4)	273 (4)	13.4 (2)

TABLE 5.1: The results of fitting $B_{\mathrm{rms}}(T)$ data for doped samples to Equation 3.10. The results for stoichiometric LiFeAs are taken from [15]. †Estimated from susceptibility data.

Before moving on, however, there is one other observation to note from the TF-μSR data shown in Fig. 5.3: In all doped samples, $B_{\mathrm{rms}}(T) \propto \lambda_{ab}^{-2}(T)$ saturates and becomes flat below around $T_c/3$, whereas this is not the case in undoped LiFeAs. The forms of $B_{\mathrm{rms}}(T)$ observed for the doped compounds are consistent with a single s-wave gap structure [95] but, as the authors of Reference [15] point out, the form observed in undoped LiFeAs suggests that a more complex, multi-gap s- or d-wave gap structure exists in this compound. While chemical substitutions have been shown to affect the gap structure in other systems [71], the apparent recovery of a single s-wave gap structure from something more complicated is unprecedented.

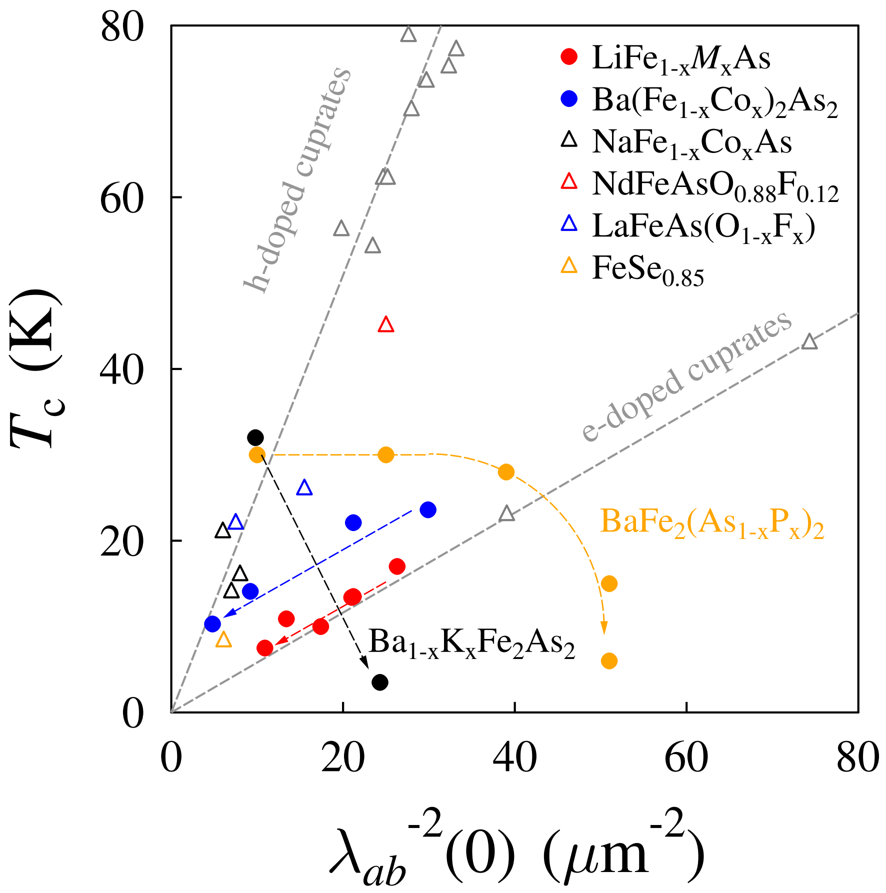

FIGURE 5.4: The Uemura plot comparing the scaling of T_c with λ_{ab}^{-2} for $LiFe_{1-x}M_xAs$ samples with that for other families of unconventional superconductors. Highlighted for particular attention are the data for three derivatives of $BaFe_2As_2$; doped with Co (electrons), K (holes) and P (isovalent). In all cases, the arrows indicate the direction of increased doping and always start from the optimally-doped composition. Data for other pnictide samples are taken from the following sources: $Ba(Fe_{1-x}Co_x)_2As_2$ [16], $NaFe_{1-x}Co_xAs$ [12], $NdFeAsO_{0.88}F_{0.12}$ [17], $LaFeAs(O_{1-x}F_x)$ [18], $FeSe_{0.85}$ [19], $BaFe_2(As_{1-x}P_x)_2$ [20] and $Ba_{1-x}K_xFe_2As_2$ [21, 22]. Data for the hole-doped cuprates come from [23] and those for the electron-doped cuprates come from [24, 25].

5.3.2 Discussion I: Fermi surfaces, gap structure and the Uemura plot

Perhaps the most prevalent explanation for the Uemura plot, certainly before the pnictides were discovered, was that it captured the so-called “BEC-BCS crossover” picture. Uemura himself [128–130] noted that, while a scaling between T_c and n_s/m^* ($\propto \lambda_{ab}^{-2}$) is not expected in BCS theory, the transition temperature for a Bose-Einstein condensate,

T_{B}, depends only on n_s/m^*. Thus, the scaling is expected if the superconducting T_{c} is actually the temperature at which pre-formed Cooper pairs condense. Strictly speaking, a BEC is a phenomenon concerning non-interacting bosons and this explains why T_{c} is always found to be less than the value of T_{B} estimated from the measured value of n_s/m^*; as the interactions between pairs suppress the transition temperature. As n_s grows, and these interactions become more significant, BEC-type physics will cease to become applicable, pair formation and condensation temperatures will converge and BCS-type physics, which contains no scaling, will dominate. Hence, conventional superconductors are all found to lie on the right of the Uemura plot, with high n_s/m^* values and no observed scaling (this is not shown in Fig. 5.4, but see Reference [128]). The Uemura plot then expresses how close to a Bose-Einstein condensate a given superconductor is.

There are a number of problems with the BEC-BCS crossover scheme. Chiefly, it was found for certain cuprates that attempting to raise n_s by carrier doping was unsuccessful [131, 132]. Instead, n_s was found to track T_{c} on the overdoped side and fall, just as I have observed for the LiFe$_{1-x}M_x$As series (see Table 5.1). The normal state carrier density, n_n, was shown to increase as expected but the corresponding reduction in n_s seemed to suggest that this was promoting a more BEC-like system, which was difficult to explain. One would expect n_s to follow n_n and for the system to become more BCS-like on doping as the interactions between carriers were increased. Another problem with the BEC-BCS scheme when applied to pnictides concerns the debatable existence of a pseudogap in these materials. For the cuprates, the pseudogap can be interpreted as the onset of the formation of phase-incoherent Cooper pairs [133], which can then condense at T_{c}. For pnictides, the situation is unclear; some experiments find evidence for a pseudogap [134, 135] but others find none [136].

This leads me to propose a different way of examining λ_{ab}^{-2} data that, while not entirely excluding the possibility that the BEC-BCS crossover picture is valid, may explain some of the features this scheme fails to account for. The starting point is a result from Chandrasekhar *et al.* [96], who demonstrate that the London formula that relates λ_{ab}^{-2} to n_s/m^* is only truly valid for materials with a spherical (3D) or cylindrical (2D) Fermi surface. In general, $\lambda_{ab}^{-2}(0)$ is governed by an integral of the Fermi velocity over the Fermi surface[1]. For Fe-based superconductors, whose Fermi surfaces are composed of nearly cylindrical sections (see Chapter 2), one would expect the London formula to be a good approximation, and indeed many authors parameterise their findings in terms of an effective n_s/m^* accordingly. This is justifiable as long as one accepts that this value will not equate to the true ratio of the carrier density and effective carrier mass, though it may be close. The insight provided by the Chandrasekhar result then leads me to propose that Fermi surface considerations can not only explain my results, but also those for other superconducting systems.

To begin, and as an aside, this approach quickly accounts for the variation in the values of $\lambda_{ab}^{-2}(0)$ found in conventional superconductors as being a consequence of their widely varying Fermi surface topologies [137]. It should also be noted that $T_{\rm c}$ is not expected to depend on details of the Fermi surface in BCS theory as the energy scale of the phonons that mediate pairing in conventional systems is set by the Debye frequency, and thus is far less than the Fermi energy. This was quickly spotted by Uemura [127, 128] who took the scaling seen in cuprates as evidence against phonon-mediated pairing. Instead, he points out, it suggests that the pairing mediator has an energy close to, or above, the Fermi energy.

The Chandrasekhar result can be used to explain the varying values of $\lambda_{ab}^{-2}(0)$ both between and within pnictide series because the Fermi surfaces of these materials are easily

---

[1] To be clear, the value of $\lambda_{ab}^{-2}(0)$ is governed by this integral, and the temperature-dependence of the gap structure determines that of $\lambda_{ab}^{-2}(T)$. See Appendix C for an explicit presentation of this result.

compared. For instance, the difference between the positions of LiFeAs and optimally hole-doped $Ba_{0.6}K_{0.4}Fe_2As_2$ on the Uemura plot (Fig. 5.4) can be accounted for by noting that the Fermi surface of LiFeAs contains a considerably larger hole pocket around Γ (compare the ARPES data for LiFeAs [138] with that for $Ba_{0.6}K_{0.4}Fe_2As_2$ [139]). The authors of References [123] and [21] carry out this analysis explicitly and calculate values of $\lambda_{ab}^{-2}(0)$ for LiFeAs and $Ba_{0.6}K_{0.4}Fe_2As_2$ respectively, to compare with their measured values. The value calculated by Inosov *et al.* [123] for LiFeAs ($172 \pm 20\,\mathrm{nm}$) not only agrees with the value they measure using small-angle neutron scattering (SANS), but also the result from TF-μSR [15]. These accounts confirm the accuracy of the Chandrasekhar result.

While this approach can clearly explain the value of $\lambda_{ab}^{-2}(0)$ measured for a compound in isolation, I believe it is at its most powerful when accounting for variations of this quantity with doping – something the basic BEC-BCS crossover scheme struggles to do. To explain my result for the $LiFe_{1-x}M_xAs$ series, that $\lambda_{ab}^{-2}(0)$ decreases with doping, I would need corresponding information about how the Fermi surface similarly evolved as Co or Ni is added. As yet, this information is unavaliable, most probably due to difficulties in preparing single crystal samples of sufficient quality for ARPES or quantum oscillation experiments. The best I can do is then to compare my results to those from series whose Fermi surface evolution has been mapped out, and also to the results from band structure calculations.

As well as my data for $LiFe_{1-x}M_xAs$, I have also shown values of $\lambda_{ab}^{-2}(0)$ for various derivatives of $BaFe_2As_2$ in Fig. 5.4. These series are highlighted as Fermi surface data are more readily available for these compounds than other pnictides because they are comparitively easy to grow to sufficient quality. The directions of the arrows in Fig. 5.4 show the direction of increasing doping in that series, and these arrows always begin on the optimally-doped compound. It is immediately clear that the electron-doped $Ba(Fe_{1-x}Co_x)_2As_2$ series displays a similar reduction in $\lambda_{ab}^{-2}(0)$ with increasing x to that seen in $LiFe_{1-x}M_xAs$. By contrast, doping the system with holes (through substituting Ba for K) appears to increase $\lambda_{ab}^{-2}(0)$, as does the formally isovalent substitution of As for P.

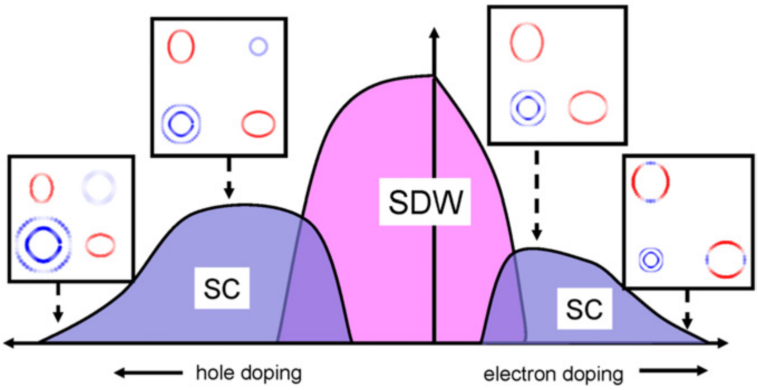

Figure 5.5: Calculated effects of both electron and hole doping on the general Fermi surface. The hole pockets around Γ are clearly the most sensitive to doping. Figure taken from Reference [26].

The contrast between the effects electron and hole doping is easily explained by the band structure calculations given in Reference [26]. In this paper, the authors demonstrate that the sizes of the hole pockets around Γ are far more sensitive to doping than those of the electron pockets. The former then contract (expand) with increased electron (hole) doping leading to a decrease (increase) in the overall Fermi surface volume and thus, through the Chandrasekhar result, to a decrease (increase) in $\lambda_{ab}^{-2}(0)$. These findings are supported by the experimental results described in References [78] ($Ba_{1-x}K_xFe_2As_2$) and [77] [$Ba(Fe_{1-x}Co_x)_2As_2$]. The trend seen in the data for the isovalent P-substituted compound can be accounted for by the detailed quantum oscillation data given in Reference [140], which reports that the size of this Fermi surface also increases with x. Additionally, the authors observe a corresponding reduction and subsequent saturation of the effective mass, which would account for the saturation in $\lambda_{ab}^{-2}(0)$ if the London formula remains valid.

Clearly, then, the Chandrasekhar result can account for the values of $\lambda_{ab}^{-2}(0)$ seen in various series and how they evolve with doping. However, this result cannot explain Uemura scaling in its entirety as it does not explain variations in the values of T_c. To do this, it is most likely that we will have to wait for a confirmation of the pairing mechanism. As mentioned earlier, it is likely that the mediating boson will have an energy close to the Fermi energy so as to allow $T_\mathrm{c} \propto \lambda_{ab}^{-2}(0)$, given that the latter clearly depends on details of the Fermi surface. It should also be said that I have not incorporated changes in the Fermi velocity into this discussion, as not every reference describing Fermi surface data calculates this quantity. Variations in this quantity may help explain why, for example, the value of $\lambda_{ab}^{-2}(0)$ for LiFeAs and optimally doped $\mathrm{Ba(Fe_{1-\mathit{x}}Co_\mathit{x})_2As_2}$ are so similar, despite the former appearing to have a much larger Fermi surface [77, 138].

I now return to the apparent change in gap structure suggested by the forms of $\lambda_{ab}^{-2}(T)$ observed in stoichiometric LiFeAs and all doped samples. In the former, the form of $\lambda_{ab}^{-2}(T)$ is not consisent with a single s-wave gap, for which one would expect a saturation below $\sim T_\mathrm{c}/3$ [95]. There is some debate around both the gap symmetry and gap structure in Fe-based superconductors, but most data for LiFeAs has been interpreted in terms of a two-gap $s^{\pm}$ state [122, 141, 142], where the sign of the gap changes between different sections of Fermi surface. This is consistent with the form of $\lambda_{ab}^{-2}(T)$ that Pratt *et al.* [15] observed. The sizes of the two gaps are estimated, from measurements of $\Delta\lambda(T)$ made using a tunnel diode resonator [143], to be close to 2.76meV and 1.67meV. These values are within the limits imposed by the ARPES data [138], and together these results suggest that the smaller gap is opened on the hole pockets.

The saturation of $\lambda_{ab}^{-2}(T)$ below $\sim T_\mathrm{c}/3$ is seen, however, in all doped samples. It would appear that doping changes the relative contributions of the gaps from different parts of the Fermi surface, perhaps by removing one of the hole pockets altogether and leaving a single s-wave gap behind, although confirming this requires experimental studies of the Fermi surface evolution with doping which are not yet available. In the meantime, carrying out TF-μSR experiments on doped samples closer to the stoichiometric compound than those studied here would be a good suggestion for further work. One could look for a smooth evolution in the form of $\lambda_{ab}^{-2}(T)$ from multi- to single-gap behaviour, perhaps carrying out similar analyses to those in Reference [19], who fit TF-μSR data for $\mathrm{FeSe}_{0.85}$ to different gap-structure models. It would be interesting to see if this evolution was indeed smooth, or if any level of off-stoichiometry caused an abrupt switch in gap structure.

While some peculiarities, such as this gap-structure behaviour, remain, my measurements of $\lambda_{ab}^{-2}(0)$ for the $\mathrm{LiFe}_{1-x}M_x\mathrm{As}$ series do appear to be very similar to those for the electron-doped $\mathrm{Ba(Fe}_{1-x}\mathrm{Co}_x)_2\mathrm{As}_2$. The values for the optimally doped compounds are similar, and in both cases they decrease with increased doping (see Fig. 5.4). Returning to the dichotomy presented at the beginning of this chapter, these results would support the idea that LiFeAs is similar to an optimally electron-doped pnictide. In the next section, I present results that confound this conclusion.

5.4 Magnetic fluctuations and spin freezing in $\mathrm{Li}_{1-y}\mathrm{Fe}_{1+y}\mathrm{As}$

The debate about whether or not LiFeAs simply resembles the optimally electron-doped members of other pnictide families would be almost settled were one to successfully hole-dope it, and induce an ordered magnetic state. Motivated by this, Michael Pitcher attempted a series of $\mathrm{LiFe}_{1-x}\mathrm{Mn}_x\mathrm{As}$ samples [30] but found merely a rapid suppression of superconductivity with no evidence of emergent magnetic order. Others have attempted hole doping by substituting Mn or Cr on the Fe site in other pnictide parent compounds and also found that they do not move one along the phase diagram as expected [144, 145]. It thus appears that such substitutions are doing much more than simple hole doping; probably also introducing strong sources of magnetic scattering. In any case, it seems that simple transition metal substitution cannot achieve controlled hole doping in these systems, and one must be more imaginative.

An intriguing alternative is provided by another of Michael Pitcher's series; the Fe-rich $\mathrm{Li}_{1-y}\mathrm{Fe}_{1+y}\mathrm{As}$, where extra Fe ions sit on vacant Li sites. It is difficult to confirm directly whether or not this achieves hole doping, but, as we shall see, it does produce a novel and emergent magnetic state when superconductivity is destroyed.

Three non-superconducting compositions were used in this study, with $y = 0.01, 0.018$ and 0.04 confirmed by Rietveld refinement of high-resolution NPD data. For comparison, I also studied two non-superconducting (overdoped) $\mathrm{LiFe}_{1-x}\mathrm{Ni}_x\mathrm{As}$ samples, with $x =$ 0.1 and 0.2. The work described in this section is published in Reference [146].

5.4.1 DC magnetic susceptibility

Figure 5.6(a) and (b) show the magnetic mass susceptibility data for the Ni-doped and Fe-rich series' respectively, obtained using the SQUID. In both cases, the data show a Curie-Weiss-type paramagnetic response and a possible spin-glass transition at low temperatures, where the field-cooled and zero-field-cooled signals diverge. From the behaviour of the molar susceptibility, χ_{mol}, one can calculate the effective moment size per formula unit by fitting to a Curie-Weiss function: $\chi_{\mathrm{mol}} = C/(T-\theta)$, where C is a constant that depends on this moment size, and the sign of θ dictates whether correlations are antiferromagnetic ($\theta < 0$) or ferromagnetic ($\theta > 0$) in nature. As

Fig. 5.6(c) shows, while the Ni-doped samples display antiferromagnetic (labelled AFM) correlations at all temperatures, there appears to be a crossover from AFM to FM correlations in the two most Fe-rich samples. Figure 5.6(d) shows the evolution of the size of the effective moment with substitution concentration for both series; clearly substituting Fe for Li results in a higher effective moment than if Fe is replaced with Ni. The fact that these moments vary in size suggests that they are itinerant, and the extra Fe atoms are not simply acting as magnetic impurities.

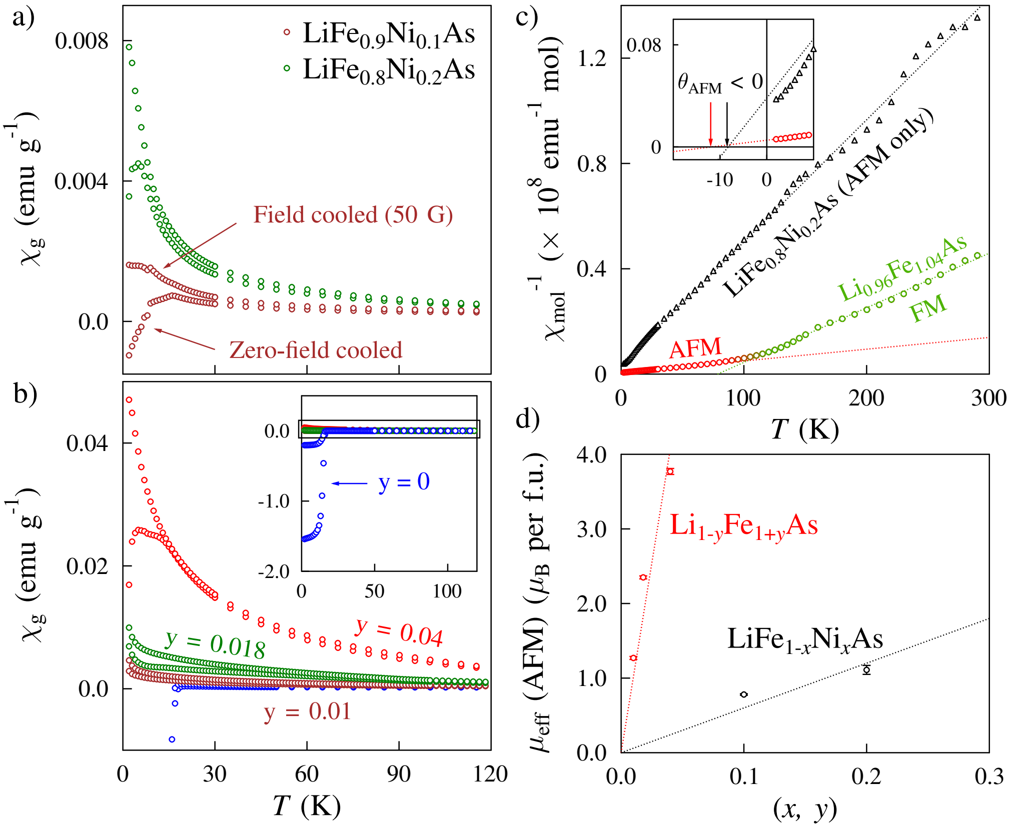

FIGURE 5.6: Magnetic susceptibility data for the $\mathrm{LiFe}_{1-x}\mathrm{Ni}_{1+x}\mathrm{As}$ (a) and $\mathrm{Li}_{1-y}\mathrm{Fe}_{1+y}\mathrm{As}$ (b) series'. Shown in the *Inset* to (b) is the characteristic response of superconducting LiFeAs. All data were taken in an applied field of 50 G. Panel (c) compares plots of the inverse molar susceptibility, χ_{mol}^{-1}, for both series, highlighting the cross-over from AFM to FM behaviour in the Fe-rich series that is not seen in the purely AFM Ni-doped series. Panel (d) compares the AFM moment sizes [per formula unit (f.u.)] for all samples calculated by fitting molar susceptibility data to a Curie-Weiss function.

5.4.2 μSR measurements

In order to further investigate the magnetic state of these compounds, ZF-μSR measurements were performed using the GPS Spectrometer at PSI. As well as the three Fe-rich and two Ni-doped samples, I also include results on the undoped, stoichiometric compound; both for comparison and in relation to the theory of triplet pairing [125]. The susceptibility data suggest that $Li_{1+y}Fe_{1+y}As$ can accommodate FM fluctuations, so I began by searching for evidence of the time-reversal symmetry (TRS) breaking in LiFeAs that may accompany triplet pairing. ZF-μSR has previously been shown sensitive enough to detect the small magnetic fields induced under spontaneous TRS-breaking in unconventional superconductors such as $LaNiC_2$ [147] and Sr_2RuO_4 [148], where small changes in the width of the field distribution appear below T_c. Such an occurance in LiFeAs would lend great support to the triplet pairing hypothesis.

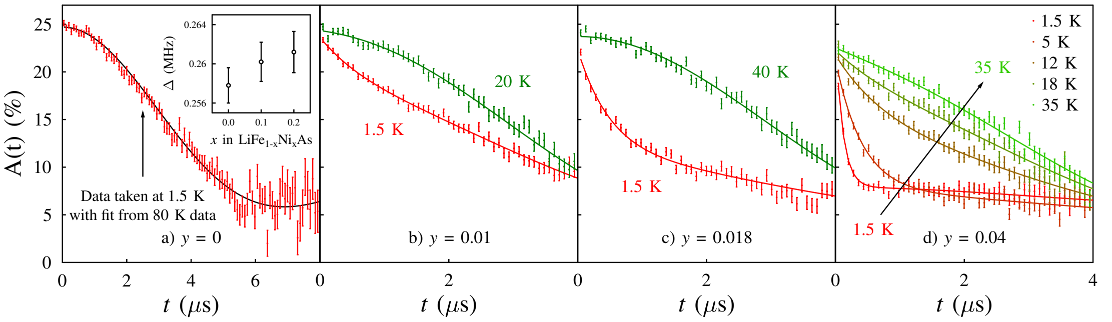

FIGURE 5.7: The ZF-μSR data for all samples studied: (a) the data for LiFeAs taken at 1.5 K, with the fit from the data taken at 80 K superimposed. This data is best described by a Kubo-Toyabe (KT) function with a temperature-independent width, Δ. *Inset*: the variation (with Ni concentration) of the width, Δ, of the temperature-independent KT functions used to describe the data for the Ni-doped samples (not shown). (b)–(d) the data for the three Fe-rich samples, showing KT relaxation at high temperatures that becomes more exponential on cooling. The effect is clearly stronger in samples with a higher Fe concentration.

The data for all samples is summarised in Fig. 5.7. The data shown in Fig. 5.7(a) is for the stoichiometric compound and is best described by a Kubo-Toyabe (KT) function, from the random nuclear dipole field. The figure shows the fit to the data taken at 80 K superimposed on the data taken at 1.5 K, emphasising that no temperature-dependent changes in this relaxation were observed, either around T_c or in any other regime. Thus, no evidence of spontaneous TRS-breaking was found, so these data do not support a triplet pairing hypothesis.

The data for the Ni-doped samples are not shown, as they too are best described by temperature-independent KT functions. The only observable difference between these data and those for LiFeAs are small increases in the width, Δ, of the KT function with increasing Ni concentration. This is expected as the nuclear dipole moment of Ni ($-0.75\,\mu_N$) is significantly larger in magnitude than that of Fe ($0.09\,\mu_N$), so the field distribution from such random nuclear moments is slightly broadened by increasing the amount of Ni. It seems that the AF-correlated moments identified by the SQUID do not order or freeze in any way that μSR can detect.

This is in contrast to what is seen in the Fe-rich series. The relaxation functions describing the data shown in Fig. 5.7(b)–(d) clearly evolve from KT-like at high temperatures, to strongly exponential on cooling. This effect emerges gradually and continuously as the temperature is lowered and is stronger in samples with a higher Fe concentration. At first glance, this looks like a freezing of the spins identified by the SQUID. This is supported by the data shown in the inset to Fig. 5.8. These data are taken from the $Li_{0.96}Fe_{1.04}As$ sample at 10 K in ZF and a longitudinal field (LF) of 1000 G. Such fields have been shown [11] to help one distinguish between static and dynamic magnetic effects, as muons affected solely by the former can be typically decoupled from them by the field, giving rise to a flat asymmetry function. As there is still some, albeit weaker, relaxation seen in the LF spectra, the magnetic effects observed most probably have a dynamic nature. I suggest that these data correspond to a freezing of the dynamically fluctuating, AF-correlated moments identified in the susceptibility data.

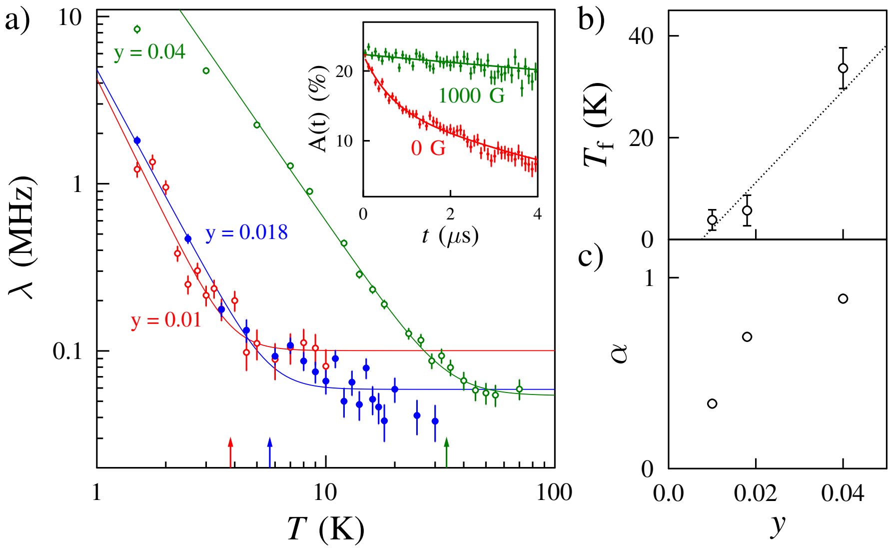

FIGURE 5.8: a) The evolution of $\lambda(T)$ for the $\mathrm{Li}_{1-y}\mathrm{Fe}_{1+y}\mathrm{As}$ series. The spin-freezing temperature, T_f, is defined as the onset of the power law increase in $\lambda(T)$ and these values are marked by arrows. *Inset:* spectra at 10 K in both zero-field and a longitudinal field (LF) of 1000 G. The weak relaxation still present in the LF spectrum indicates dynamic behaviour, pointing to a spin-freezing picture, as opposed to static local order (see text). Also shown is the dependence on extra Fe concentration of T_f (b) and *alpha* (c). The latter is the fractional occupancy of the muon site corresponding to the fast relaxation rate, and is defined in Eq. 5.2.

To analyse the data presented in Fig. 5.7, it was first assumed that the structure of LiFeAs accommodates two distinct muon sites. This is consentent with both my own observations of two main frequencies in the ordered phase of NaFeAs derivatives (see Chapter 4) and sites calculated from the structures of other pnictides [99]. In this $\mathrm{Li}_{1-y}\mathrm{Fe}_{1+y}\mathrm{As}$ series, which is isostructural to NaFeAs, I therefore expected to fit my data to the two-component function

$$A(t) = G_{\mathrm{KT}}(\Delta, t)[\alpha\,\mathrm{e}^{-\lambda t} + (1-\alpha)\,\mathrm{e}^{-\lambda R t}], \tag{5.2}$$

with a fixed relaxation rate ratio, R, and site occupancy fraction, α, and a variable main relaxation rate, $\lambda(T)$. Both muon sites will experience relaxation that combines the effects of these freezing moments with those of the nuclear field, so a KT function with a fixed width (G_{KT}) was included as an overall multiplicative component.

Figure 5.8(a) plots the behaviour of $\lambda(T)$ for the Fe-rich series. At low temperatures, this relaxation rate diverges with a power-law dependence; the onset of which can be used to define a spin-freezing temperature, T_{f}. The values of T_{f} for this series are shown in Fig. 5.8(b) and have been used, along with data taken from [14], to construct a phase diagram for LiFeAs derivatives shown in Fig. 5.9.

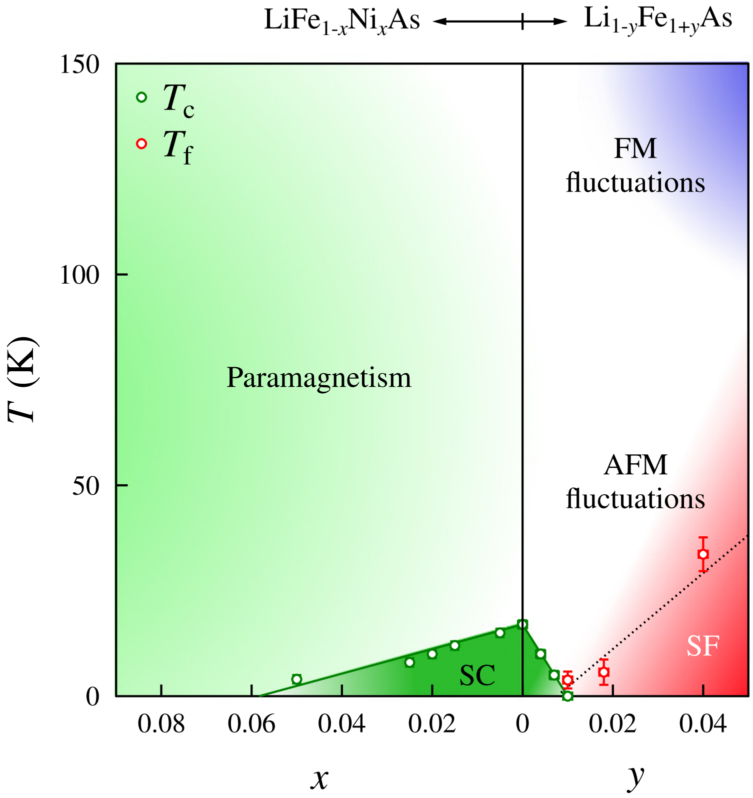

FIGURE 5.9: Phase diagram for the $\mathrm{Li}_{1-y}\mathrm{Fe}_{1+y}\mathrm{As}$ and $\mathrm{LiFe}_{1-x}\mathrm{Ni}_x\mathrm{As}$ series, showing regions of superconductivity (SC), spin freezing (SF) as well as (anti)ferromagnetic fluctuations.

It turned out to be quite difficult to resolve the lower relaxation rate, given by λR in Eq. 5.2. This is not too surprising if the dynamics seen in these samples operate in the fast-fluctuation limit. In this case [11], the relaxation rate experienced by muons on a given site will be given by $\lambda = 2\Delta_{\mathrm{site}}^2/\nu$, where $\Delta_{\mathrm{site}}/\gamma_\mu$ is the local field at that site.

My work on NaFeAs demonstrates that the sizes of these local fields differ by a factor of $\sim$ 10, so we expect the relaxation rates to differ by a factor of $\sim$ 100, making the second very small indeed.

Of course, I cannot rule out the possibility that this lower rate is, in fact, absent, and Eq. 5.2 actually describes mesoscopic phase separation between regions of static, local order and paramagnetism. This is reminiscent of what is seen in the IM phase of $\mathrm{NaFe}_{1-x}\mathrm{Co}_x\mathrm{As}$ samples (Chapter 4) which also show an exponential relaxation at low temperatures. The variation in the fractional amplitude, α, of the two contributions to the asymmetry [shown in Fig. 5.8(c)] is also more readily explained in the phase-separation picture as corresponding to an evolution in the sizes of magnetic regions. However, I suggest that the clear dynamic behaviour suggested by the LF spectra and the glassy behaviour revealed by susceptibility measurements mean that the spin-freezing picture is the most plausible. It could be that the variation in α, that suggests changes in the relative occupancies of the two muon sites in the spin-freezing picture, is simply down to structural evolution making one of the sites less favourable as more Fe is added.

5.4.3 Discussion II: Magnetic instabilities in LiFeAs

I propose that substituting Fe onto the Li site in LiFeAs induces itinerant moments that fluctuate with ferromagnetic correlations at high temperature and that become antiferromagnetic on cooling, before they finally freeze at low temperature. The itinerant nature of these moments is suggested by the variations observed in their size; if the Fe ions on the Li site were acting as random and isolated impurity spins one would expect to calculate a constant moment size, perhaps close to the values predicted by Hund's rules ($\sim 5\,\mu_{\mathrm{B}}$ [84]). In fact, if one assumes that these moments are solely located on the extra Fe atoms, the data for $Li_{0.96}Fe_{1.04}As$ suggest that each extra Fe carries an unphysical moment of 18.8 μ_B.

Exactly how this substitution drives these changes in the magnetic properties of LiFeAs is unclear, and one missing piece of information is the valence of the Fe ions that sit on Li sites. These systems are not truly ionic but it does seem that the formal valences of Li^{1+}, Fe^{2+} and As^{3-} are accurate; for example, the way in which Co and Ni substitutions appear to add electrons suggests that they too are in a 2+ oxidation state. Formally, then, one would expect the extra Fe to be in a 1+ oxidation state but this is currently unconfirmed. One experiment which may be worthwhile would involve a series of x-ray absorption near-edge spectroscopy (XANES) measurements [149] on these compounds to try and measure the valence state of these extra Fe atoms directly.

Even without intimate knowledge of how the extra Fe may affect the electronic structure, it is clear that electron or hole doping is not the only way to affect properties. Isovalent substitutions, such as replacing Fe for Ru, have been shown to destroy magnetic order and promote superconductivity in other systems [150], albeit requiring much higher concentrations than if Co is substituted [151]. Alternatively, applied pressure has been shown to have dramatic effects on the magnetic and superconducting properties of various systems [111, 152, 153]. Clearly, then, one can easily affect the electronic structure of Fe-based superconductors by altering the chemical structure, be it by substitution or pressure, and it could well be that this plays a part in inducing the effects we see in $Li_{1-y}Fe_{1+y}As$. Michael Pitcher [14] showed that Fe substitution has a much greater effect on the structure of LiFeAs than incorporating Co or Ni. It is also worth highlighting the extreme sensitivity to off-stoichiometry exhibited by the properties of other pnictides, such as superconductivity in FeSe [154] and NaFeAs [155].

I believe that my results reinforce the suggestions of Platt *et al.*, that LiFeAs is close to both ferromagnetic and antiferromagnetic instabilites [126]. Substituting Fe onto the Li site appears to induce moments that can exhibit both kinds of correlation, though the latter "win out" on cooling. This would agree with the INS results [115–117], which confirm that, at the energy scales relevant for superconductivity, magnetic fluctuations in LiFeAs and Li_{1-x}FeAs are antiferromagnetic.

This last reference [117] is worth commenting on specifically. The authors claim to be studying a single crystal of $\mathrm{Li}_{0.94}$FeAs, though in my experience Fe is quite willing to sit on the Li site and this can easily happen unintentionally. In my opinion, it is highly likely that they are actually looking at an Fe-rich sample very similar to the ones I have been examining. Hence, their results are of particular relevance. Their DC susceptibility data look very similar to mine and their INS experiments also find ferromagnetic fluctuations at very high neutron energies (though at a fixed low temperature). While I cannot make a direct comparison between our two studies without knowing for sure that the compounds are similar, their results do, once again, suggest the presence of multiple magnetic instabilities in LiFeAs and that removing Li (and probably substituting it for Fe) can access them.

5.5 Comparing LiFeAs to other pnictides

I began this chapter by asking whether or not LiFeAs is essentially equivalent to the optimally electron-doped pnictides, before presenting numerous results on LiFeAs and its derivatives that I now analyse them in the context of this question.

Firstly, I studied the place of the electron-doped $\mathrm{LiFe}_{1-x}M_x\mathrm{As}$ ($M =$ Co or Ni) series on the Uemura plot. Perhaps the most striking result of this is that, despite lying some way off the Uemura line for hole-doped cuprates and other pnictides, $\mathrm{LiFe}_{1-x}M_x\mathrm{As}$ actually behaves in a very similar way to the electron-doped $\mathrm{Ba(Fe}_{1-x}\mathrm{Co}_x)_2\mathrm{As}_2$ series: the optimally-doped compounds have similar values of $\lambda_{ab}^{-2}(0)$ and, in both cases, this quantity is reduced on further electron doping. This would support the former view, that LiFeAs is just like an electron-doped pnictide. However, I also demonstrated that the positions of various pnictides on the Uemura plot can be largely understood in terms of their Fermi surface properties, and so one should really be comparing the electronic structure of $\mathrm{LiFe}_{1-x}M_x\mathrm{As}$ and $\mathrm{Ba(Fe}_{1-x}\mathrm{Co}_x)_2\mathrm{As}_2$ to establish similarity. As good data for the former series don't exist yet, I cannot readily make this comparison.

Secondly, I found an apparent change in gap structure on doping, as revealed by differences between the forms of $\lambda_{ab}^{-2}(T)$ seen in LiFeAs and its derivatives. As mentioned earlier, this kind of evolution – from two-gap $s^{\pm}$-wave to something resembling single-gap s-wave, possibly even BCS-like superconductivity – is unprecedented, and would support the view that LiFeAs may be intrinsically much closer to being conventional than electron-doped $\mathrm{Ba(Fe}_{1-x}\mathrm{Co}_x)_2\mathrm{As}_2$. However, once again it is the evolution of the Fermi surface with doping that is required to understand this properly. Two gaps may remain upon doping, but changes in the relative contributions from shrinking hole pockets may cause the data to appear to follow single-gap temperature-dependence.

Finally, the freezing of itinerant moments induced by substituting Fe onto the Li site is also something not yet seen in any other system. That these moments appear to be ferromagnetically correlated at high temperatures is further evidence of LiFeAs' proximity to a ferromagnetic instability. Thus it appears that, while the superconducting state in undoped LiFeAs is similar to that in optimally electron-doped compounds, some features of the Fermi surface give rise to multiple magnetic instabilities that replacing Li with Fe can access. I suggest that the frequently contradicting body of experimental data on this compound may be a result of researchers examining samples with small and differing levels of off-stoichiometry, where signatures of FM fluctuations are picked up in samples that are slightly Fe-rich. Significant experimental and theoretical effort should now be focussed on elucidating the exact effect this substitution has on the electronic structure. In principle, this should not be a problem as making chemical changes away from the Fe plane in particular does not seem to hinder the growth of samples of sufficient quality for detailed ARPES and quantum oscillation studies [140].

In Table 5.2 I bring together a number of key experimental results on LiFeAs, and assess how each of them conclude whether or not LiFeAs is fundamentally unique among pnictides. This picture is clearly complex, but I believe that my combined TF, ZF and LF-μSR results make a significant contribution towards a possible resolution of the debate surrounding this compound.

Reference(s)	**Technique used and/or quantity measured**	**Result(s) and interpretation**
[43, 44]	$\chi_{\mathrm{dc}}(T)$, $\rho(T)$	LiFeAs is a stoichiometric superconductor, $T_c \simeq 17\,\mathrm{K}$, no evidence of magnetic order.
[14, 111]	$\chi_{\mathrm{dc}}(T,P)$, XRD	Electron doping and pressure suppress superconductivity (SC), no structural distortion.

[138]	ARPES	No nesting, large DoS at Fermi level: Nesting drives SDW, van Hove singularity drives SC. Electronic structure of LiFeAs similar to that of optimally electron-doped pnictides.
[115, 117]	INS on LiFeAs powder and single crystals of (non-SC) $\mathrm{Li_{0.94}FeAs}$	AF fluctuations at $Q_{\mathrm{AF}} = (0.5, 0.5, 0)$, resonance below T_{c}: SC driven by same AF fluctuations as those seen in other pnictides.
[116]	INS on single crystal of LiFeAs	Incommensurate AF fluctuations near Q_{AF}: accounts for inconsistency with ARPES result (no nesting), but preserves AF fluctuation-driven SC picture.
[141, 156, 157]	NMR/NQR on powder and single crystal samples samples	AF fluctuations in normal state, enhanced below T_{c}. Knight shift drops below T_{c} indicating singlet pairing: all consistent with $s^{\pm}$ state.
[142, 143, 158]	Anisotropic $H_{c2}(T)$, $\Delta\lambda(T)$ and thermal transport	2 isotropic gaps needed to account for data: fits with $s^{\pm}$ model.

[123, 124]	SANS [$\lambda_{ab}(T)$], ARPES	Data suggest single, isotropic gap; close to BCS weak coupling limit. Also, phonon signature in Fermionic self-energy: phonon mediated SC?
[159]	Raman scattering	No electron-phonon coupling, no SC-dependent phonon anomalies: phonon mediated SC ruled out.
[118]	$M(H)$	Unconventional vortex dynamics, possible vortex lattice transition.
[119]	STS (measuring quasiparticle interference)	Data best described by complex $s + id$ or p-wave pairing.
[120, 121]	NMR/NQR on single crystals	Extreme sensitivity to off stoichiometry, possible appearence of both singlet and triplet pairing.
[122]	High-field magnetometry	Field-induced chiral SC state; looks $s^{\pm}$ with chiral components in vortex lattice.

[14, 15] (This work.)	TF-μSR on powder samples $[\lambda_{ab}(T)]$	Single gap *s*-wave pairing ruled out for stoichiometric compound. Uemura scaling lies away from hole-doped cuprates and some pnictides, but is similar to that for electron-doped $Ba(Fe_{1-x}Co_x)_2As_2$. Possible change in gap structure on doping; from multi- to single-gap.
This work.	ZF-μSR on $Li_{1-y}Fe_{1+y}As$, χ_{dc}	FM fluctuations at high temperature, AF fluctuations and itinerant spin-freezing at low temperature. Suggestive of multiple magnetic instabilities.

TABLE 5.2: A summary of key experimental results and their interpretations regarding the nature of superconductivity – chiefly the symmetry and mediator of the pairing state – in LiFeAs. The results are colour-coded to indicate basic properties of LiFeAs (black), as well as the evidence for it being similar to optimally electron-doped pnictides (red), the evidence for it being fundamentally different (though still unconventional – green) and evidence for conventional, phonon-mediated pairing (cyan).

Chapter 6

FeSe intercalated with molecular species: a new family of Fe-based superconductors?

6.1 Introduction

The FeSe system, despite its apparent chemical simplicity, actually turns out to be one of the most complicated in the field of Fe-based superconductivity. The binary alloy phase diagram [160] highlights several competing structural phases around the $1 : 1$ stoichiometry; principally a hexagonal, NiAs-type structure and a tetragonal, PbO-type structure (see Fig. 6.1). On cooling, the latter exhibits the same structural transition to an orthorhombic phase as is seen in the pnictides but, interestingly, does not appear to order magnetically [47]. It does, however, exhibit a superconducting transition at $T_\mathrm{c} = 8\,\mathrm{K}$ but this only appears to occur in a narrow range of slightly Fe-rich compositions [154]. Further Fe can be accommodated on interstitial sites between the layers, and this acts to destroy superconductivity [154]. Furthermore, being a binary compound, the scope for controlling properties by chemical substitution is much more limited than in the arsenides: Se can be substituted for Te, and this can raise T_c up to 15 K [161] but transition metal substitution on the Fe site only suppresses superconductivity [162].

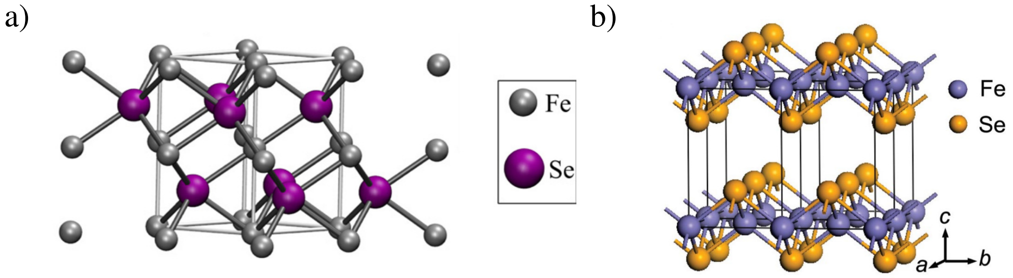

Figure 6.1: The structures of (a) hexagonal, non-superconducting FeSe and (b) tetragonal, superconducting FeSe. Images taken from References [27] and [1] respectively.

FeSe may then have become a compound of little interest if it wasn't for the dramatic increase in T_c that occurs under pressure; T_c rises to 37 K under an applied pressure of around 70 kbar [55]. Clearly able to accommodate an impressive superconducting state, FeSe then became the focus of increased attention as researchers looked for other ways to raise T_c. In 2010, a new series of compounds with $T_c \sim 30$ K were found with FeSe layers separated by K, Rb and Cs [163–165]. However, while their superconducting properties are intriguing, these systems appear to be markedly different from FeSe. For instance, the 1 : 1 stoichiometry of the layers in FeSe is not preserved in these compounds [166], and their nominal composition turns out to be $A_{0.8}Fe_{1.6}Se_2$ ($A =$ K, Rb, Cs). These are therefore often referred to as the "245" compounds, reflecting the apparent molar ratio of their constituents. In addition, superconductivity is difficult to reproduce in these compositions and they are more readily antiferromagnetic, with a magnetic structure associated with Fe/vacancy order and much larger moment ($\mu_{Fe} = 3.31\,\mu_B$) than those observed in other Fe-based parent compounds [167]. Recent NMR studies [168] suggest that samples with this nominal composition actually contain two different chemical phases: a magnetic $A_{0.8}Fe_{1.6}Se_2$ phase and a superconducting $A_{0.3}Fe_2Se_2$ phase.

The chemistry of these phases is poorly understood at present, but it does seem that superconductivity occurs only when the Fe : Se ratio is near 1 : 1. The challenge, then, is to find ways of chemically altering the inter-layer spacing of FeSe, while preserving the stoichiometry of these layers.

This chapter discusses a novel series of compounds that appear to do just that. Using soft-chemistry techniques, Group I and II metals, along with ammonia, can be intercalated between FeSe layers at room temperature. The resulting compounds show superconductivity up to $\sim 45\,\mathrm{K}$ (which is the highest T_c so far reported in an Fe-chalcogenide superconductor) as well as some highly unusual structural and magnetic properties. The work was inspired by a report [169] that appeared in February 2012, which was the first suggestion that intercalated metals enhanced T_c in FeSe (though these authors had misidentified the true composition of their product).

I shall begin by presenting TF-μSR data for four samples, containing Li, Na, Cs and Sr (along with ammonia/amide). All of these samples exhibited a characteristic broadening of the field distribution from the vortex lattice, and so penetration depth estimates were made for each of them. In addition, I shall also present a preliminary estimate of the gap structure by fitting the temperature-dependence of this broadening to the so-called "α-model" [170], described in Appendix C. There are some potential problems with such a fitting procedure, which I will discuss, but the results for these samples are intriguing.

The Li-intercalate was the first to be synthesised and is the best understood from a structural point of view, so I shall pay this compound the most attention. For the remaining compounds, structural information continues to be gathered from ongoing experiments. However, as vortex lattice geometry is only indirectly related to the crystal structure, the interpretation of my TF-μSR results on these compounds should remain valid whatever their exact structures turn out to be.

One must be more careful when interpreting ZF-μSR measurements designed to probe the intrinsic magnetic state of these compounds. Knowing the chemical structure is vital for any complete understanding of the magnetic state, so I shall again focus primarily on the results for the Li-intercalate, and only present a small selection of preliminary results regarding the magnetic state of the remaining compounds.

As the authors of Reference [169] noted, many different metals can be intercalated between FeSe layers and all seem to raise T_c from 8 K to between 30 K and 45 K. Additionally, there is a report of an intercalate of Li and pyridine [171] that also raises T_c to within this range (though this compound has not been characterised as extensively as those used in my experiments). One may be tempted to conclude from this that the precise chemical details of the intercalated layer are not what drive the enhancement of T_c, but rather the act of separating these layers, with anything presumably, will have this effect. I shall begin the discussion that closes this chapter by examining how robust this conclusion is in light of my results. I shall then move on to compare the intercalates (and particularly the Li-intercalate) to other superconductors based on FeSe, to assess whether the superconducting phase in the intercalated compound is directly related to that in the starter material, or is governed by entirely different interactions. Finally, I present a summary of our current data set in Table 6.3. These compounds are, at the time of writing, less than 2 years old and there is still much we do not yet understand. I attempt therefore to identify the most important priorities for future μSR studies of these systems, as it will become clear that this technique has already revealed many of their fascinating features. The TF-μSR results on the Li-intercalate are published in Reference [82].

6.2 Synthesis and characterisation

For this project, all synthetic work was carried out by Matthew Burrard-Lucas, Simon Cassidy, Kate Burns and Stefan Sedlmaier in the Inorganic Chemistry Laboratory, Oxford.

The synthesis of any intercalate began with a preparation of the starting material which, following the results in Reference [154], was a slightly Fe-rich variant of FeSe, namely $Fe_{1.01}Se$. First, high-quality Fe powder and Se shot were ground together in a pestle and mortar, before being sealed in an evacuated silica ampoule and heated up to 700°C at 2°C/min. After being held at this temperature for 24 hrs, the ampoule was cooled to 400°C at 4°C/min and held here for a further 24 hrs. The tetragonal structure is only stable above around 300°C so the ampoule then had to be quenched rapidly in ice water to prevent the formation of the competing hexagonal phase. It was found to be difficult to prevent this entirely, but the hexagonal phase typically composed less than 1%, by mass, of the resulting powder. Sample quality was assessed by using laboratory XRD to confirm the presence of a majority tetragonal phase, and using SQUID magnetometry to confirm superconductivity below $T_c = 8\,K$.

The intercalation procedure was then carried out using a Schlenk line that enabled the controlled mixing of solvents in inert conditions and at various temperatures. I proceed to describe the method of intercalating Li with ammonia (NH_3), but all samples discussed in this chapter were made in the same way.

Following the lead in Reference [169], freshly cut Li pieces were placed in a Schlenk tube with some $Fe_{1.01}Se$ powder according to the stoichiometry $Li_{0.5}Fe_{1.01}Se$. This Schlenk tube was then evacuated and cooled to $-78°C$ in a dry ice/isopropanol bath. NH_3 was then introduced to the tube and allowed to condense onto the reactants: for every 2 g of solid, roughly 50 cm^3 of NH_3 was incorporated. The resulting solution was mixed using a magnetic stirrer for around 30 mins before being slowly warmed to room temperature in the warming (uninsulated) bath.

The success of the intercalation procedure was suggested, even at this early stage, if the mixture was observed to change colour. Solvated electrons, from the Li atoms ionising in solution, form a composite system with the positively charged regions of the NH_3 molecules (close to the H atoms). The energy levels of this system are such that the solution will absorb light from the red end of the visible spectrum and therefore turn blue. During intercalation, these electrons will be removed from the solution (as they enter the FeSe structure with Li nuclei) and so this blue colour will disappear. Provided this happened, the remaining liquid was pumped out of the Schlenk tube, as was any residual ammonia gas. The resulting powder was extremely air-sensitive and much finer than the initial $Fe_{1.01}Se$ starter. This was another positive indication of successful intercalation, as forcing new species between atomic layers tends to produce strain sufficient to break the crystallites apart. Unfortunately, this means that single crystals of these compounds are likely to be impossible to make using this technique.

The authors of Reference [169] had assumed that, through this method, they had made the composition $LiFe_2Se_2$. However, even their own structural analysis should have cast doubt on this as they found, as the Oxford group did, that the c lattice parameter of the new compound was around 20% larger than that in $K_{0.8}Fe_{1.6}Se_2$ [166], suggesting that more than just Li had been intercalated between the FeSe layers. Indeed, using a basic

$LiFe_2Se_2$ model as the starting point for Rietveld refinement against laboratory XRD data, my colleagues showed that this produced unfeasibly large Li–Se distances [82].

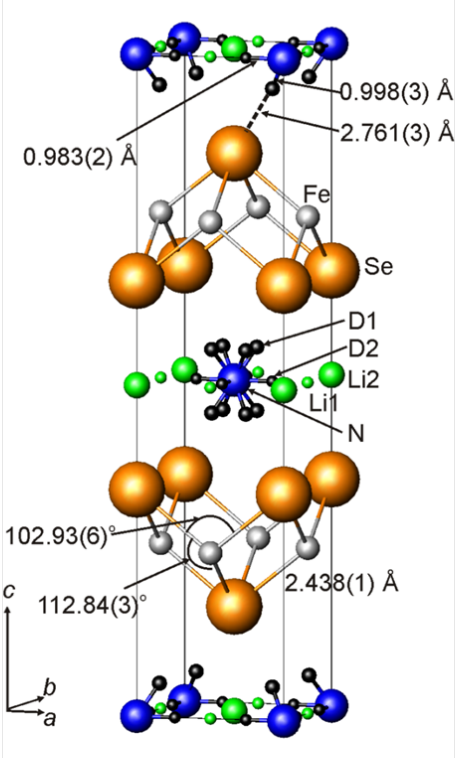

FIGURE 6.2: The structure of $Li_{0.6}(ND_2)_{0.2}(ND_3)_{0.8}Fe_2Se_2$, as determined by high-resolution neutron powder diffraction.

To identify the true composition and structure, a series of high-resolution neutron powder diffraction (NPD) measurements were performed on the HRPD and GEM instruments at ISIS. Because of the large incoherent cross-section of hydrogen, compounds for this study were synthesised with deuterated ammonia, and were presumed to be isostructural to their hydrogenated equivalents. The details of the analysis of the NPD data can be found in Reference [82]. The Li-intercalate forms with the tetragonal ($I4/nmm$) $ThCr_2Si_2$ structure – the same as that of members of the 122 pnictide family – with the ammonia occupying the 8-coordinate site and the Li atoms spread over two sites on the edges and faces of the unit cell (see Fig. 6.2). The refined composition of the Li-intercalate was found to be $Li_{0.6}(ND_2)_{0.2}(ND_3)_{0.8}Fe_2Se_2$.

Figure 6.3 shows the susceptibility data for samples from three different batches of the Li-intercalate. The data represented by blue dots is from the same hydrogenated sample used in the TF-μSR experiments I shall presently describe. The green and red data are from deuterated and hydrogenated samples respectively that were used in NPD measurements to examine the structure. All samples are superconducting below $T_c \simeq 43\,\mathrm{K}$, but do appear to have slightly different volume fractions. This is currently under investigation, but is most probably down to small variations in the ammonia concentration (see Section 6.5).

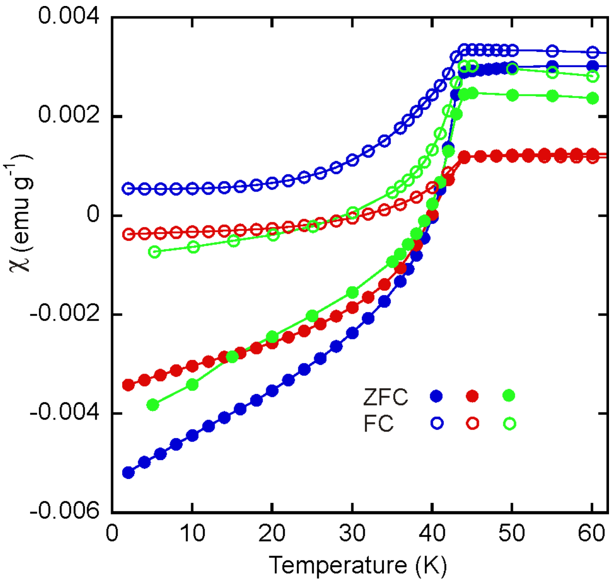

FIGURE 6.3: DC susceptibility data for three batches of the Li-intercalate: the hydrogenated sample used in the TF-μSR measurements (blue), the deuterated sample used in NPD experiments (green) and a hydrogenated sample also used in NPD (red). No difference in the values of T_c for these samples are seen, though they do appear to have slightly different volume fractions (see Section 6.5). These data were taken in an applied field of 50 G.

Following identical synthetic procedures, samples containing a range of other Group I and Group II metals (all with NH_3) were prepared. All were shown to superconduct, but there appear to be some minor structural variations in samples containing the larger metals. According to our initial Rietveld refinements against the best available structural data, the metal shares the ammonia site in the K, Rb, Cs and Ba-intercalates, whereas it occupies the Li sites shown in Fig. 6.2 for the samples containing Na and Ca. For the

Sr-intercalate, the apparent presence of significant stacking faults between the layers makes this structure even more mysterious, as many Bragg peaks are missing from the diffraction pattern. Like the remainder, though, the stoichiometry of the FeSe layers appears to be preserved in this compound. I have labelled the differing cases of metal ions occupying separate sites or sharing the ammonia site as structure type A and B respectively. These results, along with the T_c values extracted from susceptibility data, are shown in Table 6.1.

Intercalated metal	**Structure Type (see text)**	c (Å) (at 300 K)	T_c(SQUID) (K)
Li	A	16.4820(9)	43(1)
Na	A	17.361(1)	45(1)
K (phase 1)	B	14.756(1)	31(1)
K (phase 2)	B	15.898(1)	41(1)
Rb	B	15.891(3)	29(1)
Cs	B	16.294(5)	35(1)
Ca	A	16.945(5)	35(1)
Sr	?	17.3809(9)	35(1)
Ba	B	16.828(2)	35(1)

Table 6.1: The results of all structural and susceptibility measurements so far carried out on the intercalates. The K-intercalate appears to form in two distinct phases, with the same structure but varying ratios of K and NH_3, and different values of T_c.

The case of the K-intercalate is an interesting one, in that there appear to be two distinct phases available with different concentrations of K relative to NH_3 and Fe_2Se_2. These are currently believed to be $K_{0.6}$ and $K_{0.3}$, but as work to confirm this is still ongoing I refer to them as phase 1 and phase 2 respectively. These phases can apparently coexist and have different values of T_c, as shown in Table 6.1. Along with the unusual structure of the Sr-intercalate, this is another poorly-understood feature of a new compound. As mentioned in the Introduction, I shall therefore focus on the Li-intercalate, as the structural properties of this compound are the most well-characterised. Any μSR result presented on any other compound should be regarded as preliminary.

That said, while the intimate structural details of various layers are not yet confirmed for compounds other than the Li-intercalate, the value of the c lattice paramater is known for each of them. Even in the Sr-intercalate, layers are clearly present that give rise to a series of well-defined $(00l)$ Bragg peaks from which c can be extracted by Rietveld refinement. This quantity will correlate with the interlayer spacing, and so it is interesting to test whether there is any observable trend between c and T_c. These values are plotted in Fig. 6.4.

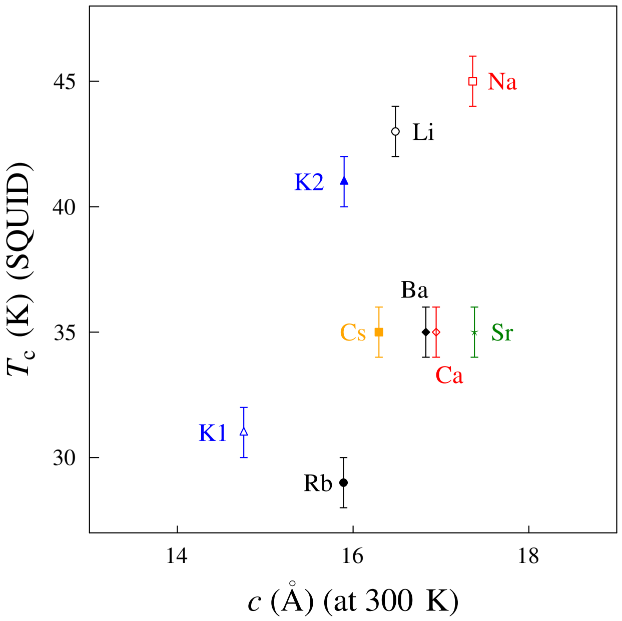

FIGURE 6.4: The superconducting transition temperature, T_c, extracted from susceptibility data, against the c lattice parameter. There may be a correlation for the light Group I metal-intercalates, but no clear correlation for the entire series is observed.

While there may be a correlation observed by the samples containing light Group I metals (Li, Na and K) there does not appear to be any significant trend that may account for the variations in T_c across the entire series. The apparent lack of a relationship between

T_c and the inter-layer spacing suggests that the enhancement of the former is not driven by merely separating the layers, but by some other structural or electronic effect.

6.3 TF-μSR: Analysis of the vortex lattice

As shown in Chapter 5, the behaviour of $\lambda_{ab}^{-2}(T)$ is intimately related to the electronic and superconducting gap structure and, since single crystals of these compounds will be difficult to produce, studies of the penetration depth may be one of the best ways to probe these structures for the forseeable future. Although all samples showed a superconducting response during susceptibility measurements, only four compounds (the Li, Na, Cs, and Sr-intercalates) exhibited a broadening of the field distribution that could be unambiguously attributed to the vortex lattice; namely, an increase in $B_\mathrm{rms}(T)$ below T_c, accompanied by a decrease (diamagnetic shift) in B_pk relative to the applied field. Some samples demonstrated the former without the latter or a form of $B_\mathrm{rms}(T)$ that most probably contains at least a contribution from an intrinsic magnetic phase. Reasons for this are unclear, though I present some recent results that may account for it in the Section 6.5. In this section however, I shall only present the data for the four compounds with an unambiguous response, beginning with the Li-intercalate.

Although not shown, typical signatures of the vortex lattice were seen in the asymmetry spectra above and below T_c in an applied transverse field of 100 G; namely, an increase in the damping of the oscillation and a reduction in its frequency. The data were then fitted to the usual function:

$$A(t) = A_\mathrm{bg}\cos(\gamma_\mu B_\mathrm{a} t)\mathrm{e}^{-\sigma_\mathrm{bg}^2 t^2/2} + A_\mathrm{s}\cos(\gamma_\mu B_\mathrm{pk} t)\,\mathrm{e}^{-\sigma^2 t^2/2}, \tag{6.1}$$

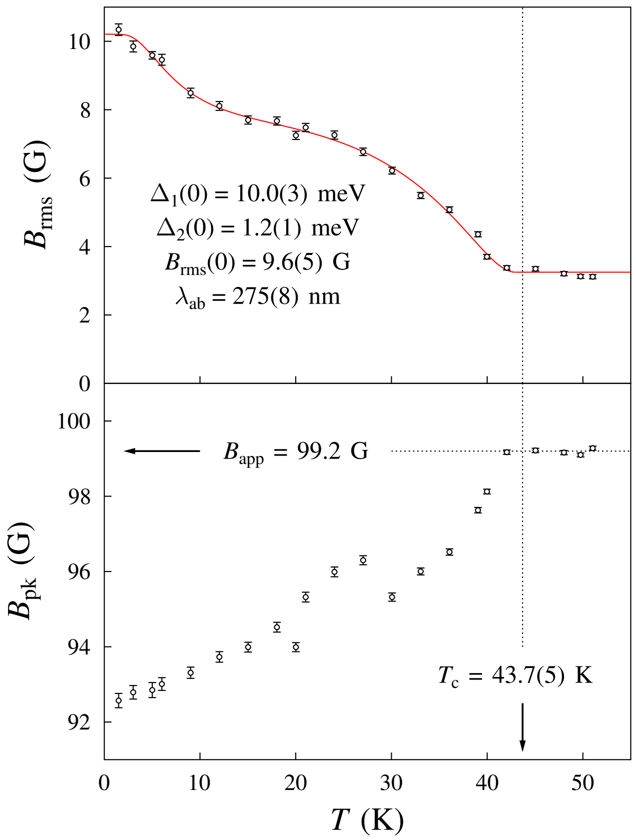

FIGURE 6.5: The TF-μSR data for the Li-intercalate [$Li_{0.6}(NH_2)_{0.2}(NH_3)_{0.8}Fe_2Se_2$]. The upper plot shows the width of the field distribution, $B_{rms}(T)$, fitted to the two-gap α-model and the lower plot shows the peak value, $B_{pk}(T)$. The diamagnetic shift ($B_{pk} \leq B_{app}$) shown in the lower plot confirms that the broadening shown in the upper plot is due to the vortex lattice. The value of T_c shown is that which was extracted from the α-model fit, and it agrees with the value extracted from susceptibility data within error.

with $\gamma_\mu B_{rms} = \sigma$. The results of this fitting procedure are shown in Fig. 6.5. The upper panel shows the breadth of the field distribution and how it varies with temperature, while the lower panel shows the corresponding evolution of the peak value of this distribution. One can see that a clear diamagnetic shift was observed and this, along with the fact that the temperature-dependent contribution to B_{rms} ends abruptly at T_c, confirms that the vortex lattice is the source of this contribution. Assuming the background contribution is temperature-independent and adds to that from the vortex lattice in quadrature, putting the extracted value of $B_{rms}(0)$ into Eq. 3.9 gives an in-plane penetration depth of $\lambda_{ab} = 275(8)$ nm.

The form of $B_{\mathrm{rms}}(T)$ can be accounted for in two ways. It could be that the rise in $B_{\mathrm{rms}}(T)$ below 10 K is due to a magnetic or superconducting impurity. For instance, the starter material ($\mathrm{Fe_{1.01}Se}$) is a known impurity and superconducts below 8 K. However, such impurities are typically found to make up less than 5% of the mass of a given sample, and it is unlikely that such a small impurity would produce such a noticeable effect.

Alternatively, and more likely, is that this form of $B_{\mathrm{rms}}(T)$ is indicative of 2-gap superconductivity, as is seen in other pnictides [19, 21]. To try and estimate the magnitudes of these gaps, I have fitted the data to the so-called "α-model" and the results of this are shown in the upper panel of Fig. 6.5. Note that the value of T_{c} shown on the plot is that from this fit, though it agrees with the value measured by the SQUID within error. The details of how this fit was achieved can be found in Appendix C.

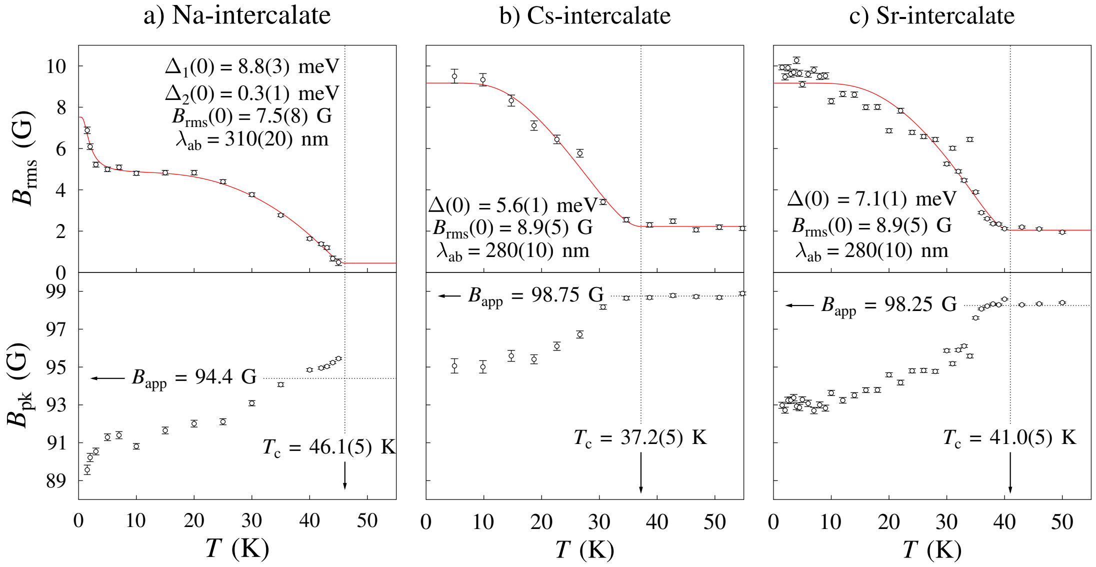

FIGURE 6.6: The evolution of $B_{\mathrm{rms}}(T)$ and $B_{\mathrm{pk}}(T)$ obtained from TF-μSR on the (a) Na-, (b) Cs- and (c) Sr-intercalates respectively. In all cases, the diamagnetic shift in B_{pk} confirms that the behaviour of $B_{\mathrm{rms}}(T)$ is due to the vortex lattice, and not an intrinsic magnetic state. T_{c} values are those extracted from fitting to two-gap or single-gap models.

Similar spectra – including clear diamagnetic shifts in B_{pk} – were observed for the Na, Cs, and Sr-intercalates, and the corresponding analyses of these data are presented in Fig. 6.6. As for the Li-intercalate, the form of $B_{\rm rms}(T)$ has been fitted to the α-model for each of these samples. For the Na-intercalate, similar two-gap behaviour was observed, although the values of the gaps are quite different from those extracted for the Li-intercalate. For the Cs and Sr-intercalates, the form of $B_{\rm rms}(T)$ was more readily accounted for by a single s-wave gap structure, so the fit was achieved by constraining the contribution from the second gap to zero (see Appendix C).

The parameters extracted from fitting $B_{\rm rms}(T)$ data in this way are shown, for all samples, in Table 6.2. While the absolute values of the superconducting gaps are presented on Figures 6.5 and 6.6, I give the correspnding value of $2\Delta_i(0)/k_{\rm B}T_{\rm c}$ in Table 6.2 as this allows for a more meaningful comparison between different systems to be made. It is notable that, while the gap structure and values seem to vary significantly from one sample to the next, the values of the penetration depth turn out to be very similar in all samples. Also shown in this table is a corresponding set of parameters extracted from TF-μSR data on $\rm FeSe_{0.85}$ in Reference [19], on the Li and pyridine ($\rm C_5H_5N$) intercalate in Reference [31] and on two of the 245 compounds [32]. The two-gap behaviour seen in $\rm FeSe_{0.85}$ is not preserved for every intercalate, and the penetration depth of $\rm FeSe_{0.85}$ is also very different from the values I measure for my samples (though it is closer to that of the pyridine intercalate).

Extacted values of $\lambda_{ab}^{-2}(0)$ are plotted against $T_{\rm c}$ to give the Uemura plot shown in Fig. 6.7. My ammonia intercalates, along with the pyridine intercalate and the 245 chalcogenides, all lie close to the hole-doped cuprate line, and therefore close to most other pnictides (see Fig. 5.4). I shall discuss what these data reveal about the similarities and differences between these compounds in Section 6.5.

Intercalate	T_c (K)	$\lambda_{ab}(0)$ (nm)	$\lambda_{ab}^{-2}(0)$ (μm^{-2})	**Gap structure** [with values of $2\Delta_i(0)/k_BT_c$]
Li	43.7(5)	275(8)	13.2(8)	$s^{\pm}$: $5.31(16), 0.64(5)$.
Na	46.1(5)	310(20)	10.4(15)	$s^{\pm}$: $4.43(16), 0.20(5)$.
Cs	37.2(5)	280(10)	12.8(10)	s: 3.49(6).
Sr	41.0(5)	280(10)	12.8(10)	s: 4.02(5).
$Li(C_5H_5N)_{0.2}$	40(1)	369(16)	7.3(7)	$s^{\pm}$: $3.96(54), 0.57(4)$.
$FeSe_{0.85}$	8.3	404(5)	6.1(1)	$s^{\pm}$: $4.49(6), 1.07(2)$.
$Rb_{0.77}Fe_{1.61}Se_2$	32.6(2)	258(2)	15.0(2)	s: 5.5(2).
$K_{0.74}Fe_{1.66}Se_2$	31.0(2)	225(2)	19.8(2)	s: 4.7(2).

Table 6.2: Extracted values of $\lambda_{ab}(0)$, $\lambda_{ab}^{-2}(0)$ and the sizes of superconducting gap(s) for various intercalates. Only those giving an unambiguously superconducting response, with no significant magnetic contribution, are presented. Also shown for comparison are data for $FeSe_{0.85}$ [19], the pyridine intercalate $Li(C_5H_5N)_{0.2}Fe_2Se_2$ [31] and two members of the 245 chalcogenide family [32].

6.4 ZF- and TF-μSR: Magnetic phases

6.4.1 The Li-intercalate

In the Li-intercalate, the Li atoms occupy two distinct sites (see Fig. 6.2). Motivated by the fact that the relative occupancies of these sites appeared to vary with temperature, a series of μSR measurements were made in ZF to look for evidence of Li diffusion. ZF-μSR has been shown [172] to be a very useful probe of such processes, as their effects can be easily distinguished from those of magnetic phases – a problem from which more conventional probes of diffusion, such as NMR, suffer. In the event, no evidence of diffusion was found but an emergent magnetic phase was uncovered. I begin this section by presenting the ZF-μSR data pertaining to this phase, before presenting some TF-μSR data from other intercalates that is also indicative of a magnetic phase. It should be noted, however, that because these TF-μSR experiments were designed to probe the vortex lattice, I cannot make a direct comparison between what they reveal

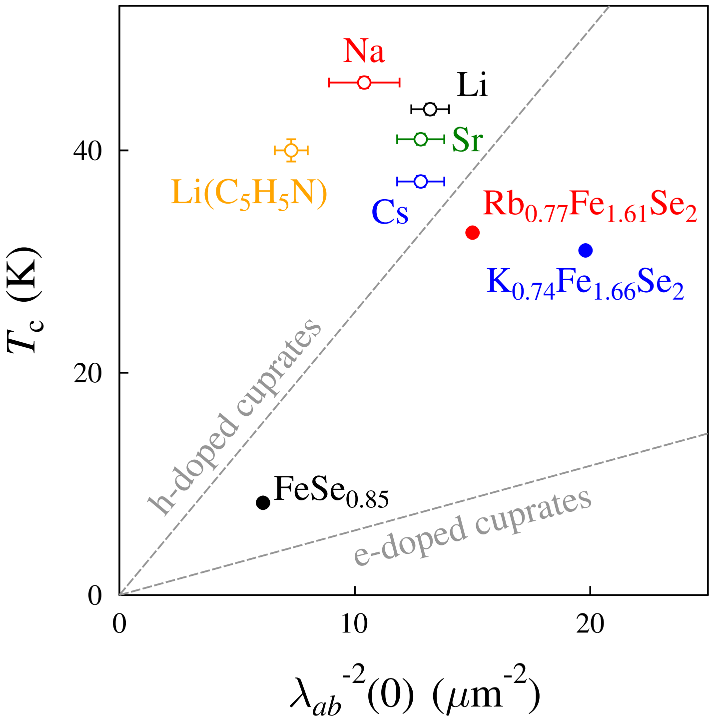

FIGURE 6.7: A Uemura plot for all superconducting compounds based on FeSe, constructed using the data from Table 6.2. The intercalates lie closer to the hole-doped cuprate line than the electron-doped cuprate line, and therefore close to most other pnictides.

and what is seen in the Li-intercalate. ZF-μSR data are needed for the remaining intercalates to facilitate a meaningful comparison between emergent magnetic phases, and such experiments are planned.

The asymmetry spectra for the Li-intercalate, taken at 295 K and 1.5 K using the MuSR spectrometer at ISIS, are shown in Fig. 6.8(a). An exponential contribution to the relaxation appears to be present at all temperatures, though it clearly makes a much greater contribution to the low-temperature relaxation. This, incidentally, was what allowed us to rule out Li diffusion: an exponentially relaxing asymmetry may be caused by this process [172], but would not become stronger on cooling as diffusion is thermally

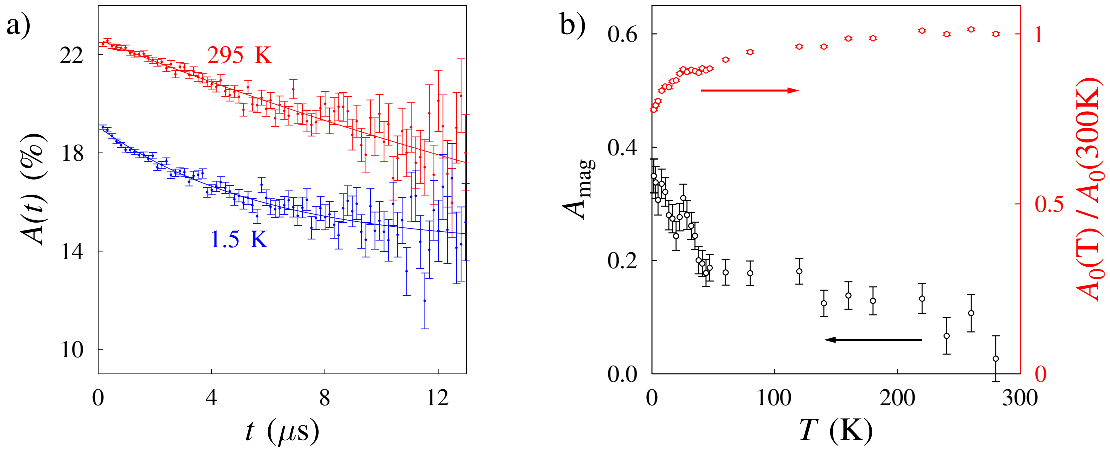

FIGURE 6.8: (a) The ZF asymmetry spectra for the Li-intercalate at 1.5 K (blue) and 295 K (red). (b) The temperature dependence of the magnetic fraction (black) and the initial asymmetry (red) obtained by fitting the data to Eq. 6.2.

activated. As well as a temperature-dependent exponential relaxation, Fig. 6.8(a) also shows an apparent reduction in the initial asymmetry on cooling.

When estimating the superconducting volume fraction from the susceptibility data shown in Fig. 6.3 (bearing in mind the limited reliability of such estimates due to the demagnetising field – Chapter 4), one finds that it is never more than around 50% in any intercalate. This suggests that around half the volume must not be superconducting. I therefore propose that the Li-intercalate supports phase separated regions of paramagnetism (that become superconducting below T_c) and an emergent magnetic state that gives rise to the exponential relaxation observed in ZF-μSR. This picture is supported by the use of a similar model to describe muon data from the pyridine intercalate [31].

In my case, the data were fitted to

$$A(t) = A_{\mathrm{pm}} \exp(-\sigma^2 t^2/2) + A_{\mathrm{mag}} \exp(-\Lambda t) + A_{\mathrm{base}}, \tag{6.2}$$

where A_{base} is the baseline asymmetry and $A_{\text{pm}} + A_{\text{mag}} = A_{\text{tot}}$, the total asymmetry[1]. The contribution from muons in paramagnetic regions is parameterised by the Gaussian term, whose width, σ, was fixed throughout fitting to its room temperature value. Muons in these regions experience only the nuclear dipole field, which should be temperature-independent. The exponential term describes the emergent magnetic contribution and, rather surprisingly, I found I also had to fix the exponent Λ in order to achieve successful fits. This is quite difficult to justify as it implies that the emergence of the magnetic phase is solely described by the behaviour of the magnetic fraction ($A_{\text{mag}}/A_{\text{tot}}$). Physically, this means that the magnetic regions are characterised only by their spacial extent and not by the sizes of the moments and/or the fluctuation rate within these regions, which are constant. This seems unlikely, but the model does still capture the essential observations; that the magnetic phase grows gradually on cooling before become abruptly stronger below around 50 K, and the initial asymmetry ($A_0 = A_{\text{tot}} + A_{\text{base}}$) decreases throughout. The behavour of these fitted parameters is shown in Fig. 6.8(b).

The problem with this fit, of having to fix Λ, led me to try a different model in which data were fitted to a single-component function:

$$A(t) = A_{\text{tot}} G_{\text{KT}}(\Delta, t) \exp(-\lambda t) + A_{\text{base}}. \tag{6.3}$$

Rather than describing phase separation, this model corresponds to the presence of dilute moments throughout the entire sample (exponential factor) broadening an otherwise paramagnetic field distribution (G_{KT}). This model produced fits (not plotted) of comparable statistical quality to those achieved using the phase separation model, but

---

[1] The baseline asymmetry is often not explicitly listed as a component of the functions used to analyse muon data, even though it is always present. This is because it is usually constant, unless dynamic magnetic phases are present (see Fig. 3.6).

conflicts with results on the pyridine intercalate [31] and does not agree so well with the results from susceptibility measurements. It also leads to further questions regarding atomic coexistence of magnetism and superconductivity (if the magnetic phase persists throughout the entire sample), and no other evidence for such coexistence has yet been found in these systems. I note that my data were taken using the MuSR spectrometer, which is not the ideal tool for characterising magnetic states; upcoming experiments on the GPS spectrometer at PSI may provide more definitive answers. In the meantime, I suggest that the phase separation model is the most consistent with results from other experiments and therefore the most plausible.

In any case, the signal from the magnetic phase is clearly described by an exponential relaxation function. As mentioned in Chapter 3, exponential relaxation functions in muon spectra are ambiguous as they can be the result of many different effects. Such a form may be ascribed to static, local order (as seen in the IM phase of $\mathrm{NaFe}_{1-x}\mathrm{Co}_x\mathrm{As}$, Chapter 4) or to dynamically fluctuating moments (as seen in $\mathrm{Li}_{1-y}\mathrm{Fe}_{1+y}\mathrm{As}$, Chapter 5). These data suggest that the latter scenario is more likely, as the magnetic phase appears to exist at room temperature and gradually grow on cooling, whereas one would expect static order to "switch on" more abruptly. One may suggest that the feature at 50 K could be just such an onset of static order, so I have plotted the behaviour of the three asymmetry parameters – A_0, A_{base} and A_{tot} – in Fig. 6.9 to help distinguish between these possibilities. This figure also allows me to address the aforementioned reduction of A_0 on cooling specifically, and I have labelled high and low temperature regimes on this figure for ease of discussion.

As shown in Chapter 3, the baseline asymmetry will be clearly affected when muons couple to a dynamically fluctuating field distribution. The observed reduction in A_{base} on cooling through all temperature regimes can be understood as a consequence of muons becoming increasingly coupled to such fluctuations as they slow down. At high temperatures, moments fluctuate outside the muon time window (i.e. very quickly) meaning that the muons only experience the nuclear dipole field which is described by a Kubo-Toyabe or Gaussian relaxation. On cooling, the fluctuation rate will drop to within the muon time window, and a Lorenztian broadening of the field distribution will set in, giving an exponential relaxation in the asymmetry spectrum along with a reduction in A_{base}. Below around 50 K the moments appear to freeze, leading to a sharp up-turn in their contribution to the asymmetry reminiscent of the situation in $\text{Li}_{1-y}\text{Fe}_{1+y}\text{As}$ (Chapter 5). As was the case for the $\text{Li}_{1-y}\text{Fe}_{1+y}\text{As}$ series, LF-μSR will be needed to confirm the presence of dynamics, as observing relaxation in LF is difficult to ascribe to typically-sized static moments. These experiments are planned.

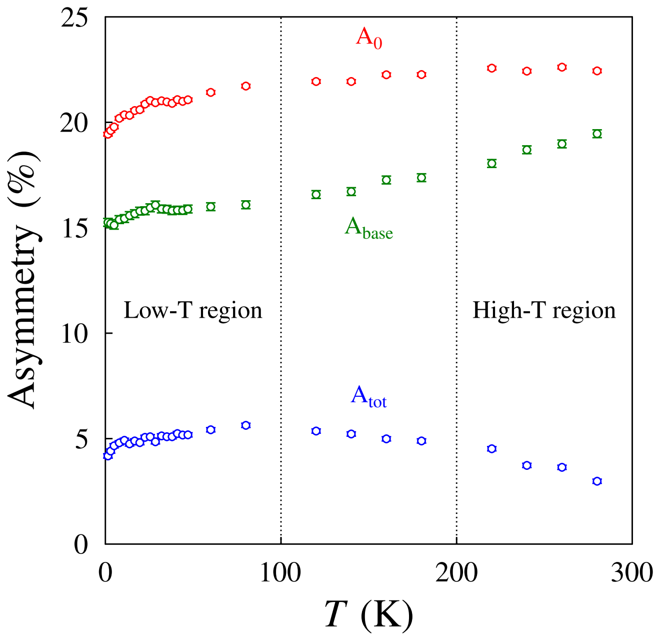

FIGURE 6.9: The initial (A_0), total (A_{tot}) and baseline (A_{base}) asymmetries as a function of temperature, from fitting to Eq. 6.2. Three approximate regions are highlighted for ease of discussion (see text).

Figure 6.9 also allows me to discuss the reduction in A_0 at low temperatures. In this regime, A_{base} is falling slightly and A_{tot} is flat. Typically, reductions in A_0 are indicative of a reduction in A_{tot} (A_{base} is usually temperature-independent). A loss of total asymmetry may correspond to the presence of quasi-static moments sufficiently large to cause muons to precess outside the time window (see, for example, Reference [173]). However, I observe a flat A_{tot} and, in addition, no evidence for the presence of such large moments ($\gg 1\,\mu_{\text{B}}$) was identified in susceptibility data. It is more likely, then, that this form of A_0 is not related to any magnetic phase, but is actually due to the formation of muonium within the molecular layer. As yet, this is unconfirmed and therefore uncharacterised, but there are various well-understood procedures for analysing muonium formation [11] and this is certainly a priority for future work. It is worth noting that a similar drop in asymmetry has been ascribed to muonium formation during experiments on solid ammonia [174].

Finally, I point out that the magnetic behavour observed in ZF could contribute to the broadening of the field distribution in TF. If this were so then my estimated value of the penetration depth would be too low, although it is difficult from these data to estimate the size of such a contribution.

6.4.2 Preliminary results on other intercalates

All the intercalates so far synthesised demonstrated a superconducting response in susceptibility measurements, and so were analysed using TF-μSR in an attempt to measure λ_{ab}. However, as previously mentioned, only four samples showed a response unambiguously consistent with a vortex lattice contribution. For the rest, behaviour like that shown in Fig. 6.10(a) was typically observed. These data are for the Ba-intercalate and, while one can see an increase in $B_{\text{rms}}(T)$ at low temperatures, it does not abruptly set in below T_{c}. Instead, $B_{\text{rms}}(T)$ appears to grow gradually on cooling. Furthermore, the diamagnetic shift seen in $B_{\mathrm{pk}}(T)$ is highly unusual compared with that seen for the Li-intercalate. While a part of $B_{\mathrm{rms}}(T)$ could come from the vortex lattice, it also appears to contain a significant contribution from some other magnetic phase. As TF-μSR is not the ideal tool with which to study intrinsic magnetic phases, I cannot say much more about the nature of it from these data. Such behaviour, that indicates contributions from both a vortex lattice and an uncharacterised magnetic phases, was observed in the K, Rb, Ca and Ba-intercalates. These observations are summarised in Table 6.3.

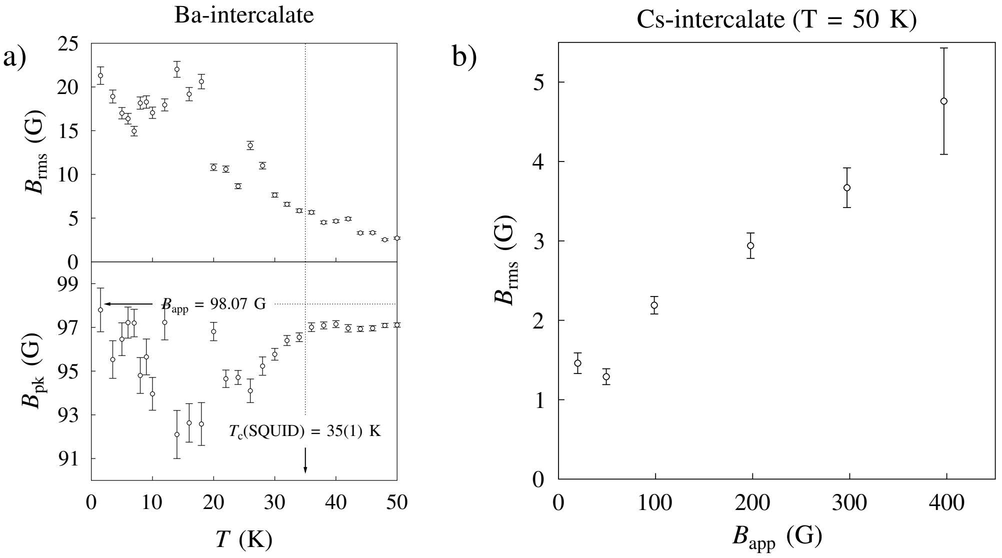

FIGURE 6.10: (a) The evolution of $B_{\mathrm{rms}}(T)$ and $B_{\mathrm{pk}}(T)$ extracted from TF-μSR data taken on the Ba-intercalate. These data, particularly the form of the latter, are inconsistent with the sample being entirely occupied by a vortex lattice; a significant intrinsic magnetic contribution is also present. (b) The field-dependence of B_{rms} above T_{c} (at 50 K) for the Cs-intercalate. The linear form is inconsistent with a solely nuclear field distribution.

Finally, an unusual field dependence of the width of the field distribution above T_{c} was found in the Cs-intercalate, and this is shown in Fig. 6.10(b). This confirms that the source of this broadening is not nuclear, as the field distribution from quasi-static, randomly-orientated nuclear dipole moments will not be affected by an applied field. The roughly linear form observed here is unaccounted for at present, but is another characteristic of the magnetic phase in this compound. It is worth reiterating that no temperature-dependent contribution, other than that from the vortex lattice, was observed in $B_{\mathrm{rms}}(T)$ for this sample, so I do not believe my analysis of $B_{\mathrm{rms}}(T)$ is in need of revision. However, as for the Li-intercalate, my estimate for the penetration depth may be too low if it turns out that there is a temperature-dependent magnetic phase below T_{c}. ZF data are needed to confirm this.

6.5 Discussion

I propose that these intercalated FeSe systems contain both paramagnetic regions, which accommodate the superconducting state below T_{c}, and regions of emergent magnetism which are probably characterised by dynamically fluctuating moments on the Fe site. There is strong and direct evidence for this phase separation in ZF-μSR data on the Li-intercalate, and comparable data on the remaining samples are forthcoming. One may be concerned that a contribution from the magnetic phase to the muon signal may make it difficult to extract meaningful information about the superconducting state, but it appears that the size of this contribution varies considerably from one compound to the next. For the Li-intercalate, I suggest that the diamagnetic shift observed in the peak value of the field distribution in TF, B_{pk}, is totally consistent with a dominant vortex lattice contribution. I also identified three other samples (containing Na, Cs and Sr) that also exhibit such a diamagnetic shift and are therefore not suspected to contain significant contributions from magnetic phases to the form of $B_{\mathrm{rms}}(T)$.

As shown in Table 6.2, these compounds appear to have very similar values of $\lambda_{ab}^{-2}(0)$, and therefore lie close to one another on the Uemura plot in Fig. 6.7. As I discussed in Chapter 5, a compound's position on the Uemura plot can be largely understood in terms of the topology of its Fermi surface and the magnitude of the Fermi velocity on various parts of this surface. The similar values of $\lambda_{ab}^{-2}(0)$ that I observe in these systems therefore suggest that they have similar electronic structures. It is also worth noting that these values for the intercalates are closer to those of the 245 chalcogenides [32], particularly $\mathrm{Rb_{0.77}Fe_{1.61}Se_2}$, than that of $\mathrm{FeSe_{0.85}}$ [19].

Given their similar electronic structures, the apparent variation in the gap structures of these systems is intriguing. I find that the Li and Na-intercalates exhibit a form of $B_{\mathrm{rms}}(T)$ that is most consistent with the two-gap $s^{\pm}$ structure that also describes data for $\mathrm{FeSe_{0.85}}$ [19] and the pyridine intercalate [31]. On the other hand, the Cs and Sr-intercalates appear to contain only a single, isotropic gap, which also happens to agree with what is observed in the 245 chalcogenides [32]. A useful insight into this debate comes from the results of inelastic neutron scattering (INS) measurements of the resonance mode. For non-intercalated FeSe derivatives, and as is the case for most pnictides, the resonance is observed at the $(\pi, \pi, 2\pi)$ wavevector [175]. This has been interpreted as a signature of the $s^{\pm}$ gap structure [176–178]. For $A_{0.8}\mathrm{Fe_{1.6}Se_2}$, however, the resonance appears to be at the $(\pi, \pi/2, 2\pi)$ [179, 180] and this is more consistent with a d-wave gap structure [181]. A recent measurement of the resonance mode in the Li-intercalate finds that it also lies at $(\pi, \pi/2, 2\pi)$ [182], suggesting that the superconducting phase in the intercalates resembles that in the 245 chalcogenides more closely than that in FeSe. This conflicts with my interpretation of the muon data for this compound as a signature of $s^{\pm}$ superconductivity, but the form of $B_{\mathrm{rms}}(T)$ expected for a d-wave superconductor is not so different to that from the $s^{\pm}$ state (see Reference [19] for a useful comparison). It may also be that a minor contribution from the magnetic state is affecting the form of $B_{\mathrm{rms}}(T)$, making it difficult to distinguish between gap structures from muon data.

With this in mind, I do not wish to say much more about gap structure estimates from my data, except to note a feature in the values of the ratio $2\Delta(0)/k_{\mathrm{B}}T_{\mathrm{c}}$. This quantity is often interpreted as a measure of the coupling strength between electrons that form Cooper pairs. This coupling is assumed to be weak in the BCS theory, where it is mediated by phonons, and one can show [95] that the "weak-coupling approximation" gives this ratio to be

$$\frac{2\Delta(0)}{k_{\mathrm{B}}T_{\mathrm{c}}} = 3.52. \tag{6.4}$$

Comparing the values shown in Table 6.2 to that from BCS theory, one can see that all samples contain a gap with $2\Delta(0)/k_{\mathrm{B}}T_{\mathrm{c}} \geq 3.52$, and in some cases this value is much greater. This suggests that these are all strongly-coupled superconductors. The apparent presence of a gap well below the weak coupling limit – in the Li, Na and pyridine intercalates, as well as $\mathrm{FeSe}_{0.85}$ – is often observed in Fe-based superconductors [183], but I reiterate that its presence in my compounds is difficult to be sure of from μSR data alone.

The INS result, that the intercalates may exhibit a superconducting state that is fundamentally different from that in FeSe, is also supported by a structural comparison. As mentioned in the introduction, interest in FeSe was largely driven by the observation of a high-T_{c} ($\sim 37\,\mathrm{K}$) superconducting phase emerging under pressure. It is then interesting to ask if FeSe layers respond to chemical pressure during intercalation in the same way as they do when under hydrostatic pressure. It may be that an identical structural response may explain the similar values of T_{c}.

Figure 6.11 compares the structures of the FeSe layers in FeSe at 90 kbar ($T_{\mathrm{c}} = 35\,\mathrm{K}$) [28, 55] and the Li-intercalate at ambient pressure. These data were taken at 16 K and 8 K and are from Reference [28] and Reference [82] respectively. As the authors of

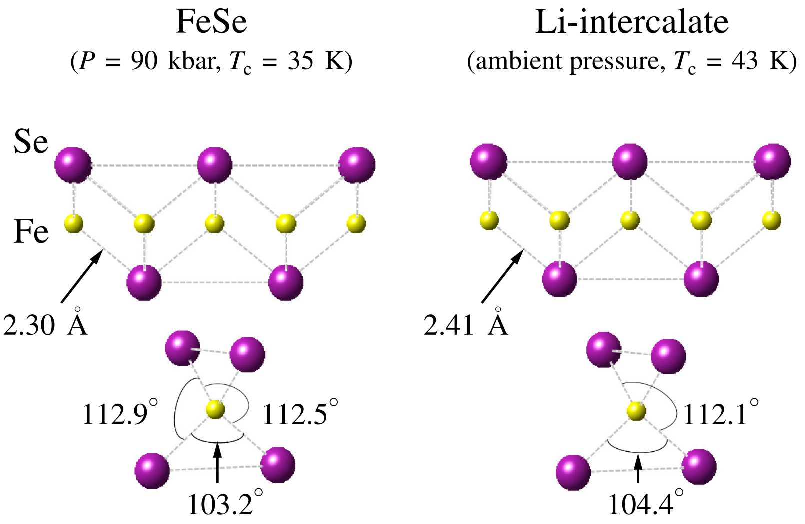

FIGURE 6.11: A comparison of the low temperature structures of the FeSe layer in unintercalated FeSe under pressure [$T_c(90\,\text{kbar}) = 35\,\text{K}$] and the Li-intercalate at ambient pressure. These data were taken at 16 K and 8 K respectively. The $FeSe_4$ tetrahedra are more distorted in the former case than the latter, and the Fe–Se bond length is larger in the intercalate. Structural data for unintercalated FeSe under pressure come from Reference [28].

Reference [28] demonstrate, the $FeSe_4$ tetrahedra become more distorted as the pressure increases; that is, the Se–Fe–Se bond angles diverge further away from the ideal angle of 109.5°. However, the bond angles in the Li-intercalate are closer to the ideal case [82] and so are closer to those in the ambient pressure (low-T_c) phase of FeSe. Therefore, as unintercalated FeSe is pressurised, its T_c rises towards that of the Li-intercalate but its tetrahedra become more distorted. This suggests that the increase in the T_c of FeSe both under pressure and through intercalation are not driven by the same structural effects.

It is therefore worth commenting on what could be driving the increase in T_c observed in the intercalates. Of course, chemical pressure could play a role, but clearly not in the same way as hydrostatic pressure does on the unintercalated compound. A key contribution almost certainly comes from electron doping. As Fig. 6.11 shows, the Fe–Se bond length in the Li-intercalate is larger than that in the starter material, consistent with those atoms being granted an increased electronegativity as electrons are added from the intercalated layer. This is interesting given that more conventional attempts to electron-dope FeSe, by substituting Fe for Co or Ni, have been shown only to reduce T_c [162]. This again raises questions about the precise role of chemical substitution; it could be that Co and Ni do simply act as magnetic impurity scatterers in FeSe and reduce T_c, but true electron doping by other means will raise it.

Another probable contributing factor behind the enhancement of superconductivity in these materials is the expected removal of any interstitial Fe from the starter material during intercalation. When sitting on interstitial sites between the layers, extra Fe has been shown to suppress T_c in FeSe [154]. Elemental Fe is consistently found as a small impurity in the intercalated compounds, despite none showing up in the starter material, suggesting that intercalation flushes it out. It could be that the increase in T_c is entirely driven by this removal, and the intercalation of any layer will achieve this goal. This would explain why the T_c values of most intercalates are so similar, but would not explain the observed differences in magnetic behaviour. In reality, it is probably a combination of electron doping, structural modifications to the FeSe layer and a removal of interstitial Fe that drive the enhancement of superconductivity in these systems. A more complete data set on samples other than the Li-intercalate will help us pinpoint the relative importance of each of these effects.

The extent of the magnetic phase in the intercalates varies considerably depending on what is intercalated, as a comparison of Figures 6.10 and 6.6 demonstrates. It is also intriguing that this phase appears to sit in regions of sample that are spatially separated from those that accommodate superconductivity. I now present some recent (unpublished) results from the Clarke group that may account for these observations.

FeSe seems to absorb ammonia (with various metals) rather readily. Therefore, under certain conditions, one may expect it to lose ammonia quite readily too. Indeed, it was quickly demonstrated that heating the Li-intercalate to around 100°C causes it to quickly decompose by losing NH_3 [82]. More recently, it has been shown that exposing the Li-intercalate to a vacuum for a few hours can recover the original starter material. This is a concern as ammonia gas was routinely pumped from the reaction vessel for an unknown length of time following the intercalation procedure behind all of the samples discussed in this chapter. The observed phase separation in the intercalates may then be the result of an inhomogenous removal of ammonia during the latter stages of synthesis. This would account for the differences between the volume fractions of samples from different batches of the Li-intercalate (shown Fig. 6.3) observed during susceptibility measurements; they may have been exposed to a vacuum for different lengths of time during synthesis and therefore lost different amounts of ammonia.

There also appears to be some unusual time-evolution in the properties of some of these compounds. For instance, when measuring the susceptibility of a sample of Rb-intercalate that is a few weeks old, one finds the superconducting signal has all but disappeared. Moreover, this sample appears to develop magnetic order – signified by the emergence of magnetic Bragg peaks – over this time-scale. The precise cause of this is currently being investigated but a steady loss of ammonia is a plausible candidate. All samples (until recently) were stored under Argon at room temperature; if they rapidly decompose at 100°C, a slow decomposition at $\sim$ 20°C seems perfectly possible.

This is further supported by some very recent measurements looking at how the structure of the compound evolves during intercalation. Placing a Schlenk tube containing metal dissolved in ammonia in a synchrotron beam, and then adding $Fe_{1.01}Se$, allows one to observe the absorption of NH_3 in real time. The resulting submerged compound is richer in ammonia than its dried out counterpart, incorporating an extra layer of

NH_3. This phase also superconducts at 40(1) K and current work is ongoing to establish whether or not the volume fraction is any different to those measured in dried samples. It may well be that the "true" superconducting phase is rich in ammonia, but losing it inhomogeneously during both drying and over time results in the formation of a separate magnetic phase. If the species of intercalated metal affected the rate or manner in which ammonia was lost, this would explain why the magnetic properties of the intercalates appear to vary so considerably from one compound to the next.

Here, then, is my conclusion: that the intercalated FeSe compounds support both dynamic magnetism and superconductivity, which exist in spacially separated regions. This phase separation may be driven by inhomogeneities in the ammonia concentration, and the apparent dependence of the magnetic phase on the intercalated species may be related to how each metal affects this loss of ammonia. The superconducting phase appears largely indifferent to the details of the intercalated layer, in that values of T_c and $\lambda_{ab}^{-2}(0)$ are similar across the series. Their proximity on the Uemura plot suggests that the Fermi surfaces of these compounds are similar to one another. Apparent variations in gap structure would challenge this, but possible contributions from magnetic phases to $B_\mathrm{rms}(T)$ cast doubt on my gap structure estimates from μSR data. Also, INS results do not support the two-gap model used to describe the Li and Na-intercalates. It also appears that the superconducting state in these intercalated systems is quite distinct from that in FeSe at both ambient and high pressure, suggesting that the intercalates belong to a separate and novel family of Fe-based superconductors.

For completeness, Table 6.3 summarises the current data set and what various results suggest for these compounds. Once again, μSR has shown itself to be a powerful tool in analysing compounds containing superconducting and magnetic phases. However, the kinds of experiments performed in this chapter can not tell one everything there is to know about a given system. The next chapter describes experiments designed to fill in some of these gaps by making use of high magnetic fields and applied pressure.

Intercalated Metal	**Existing μSR data (TF in red and ZF in blue)**	**Interpretation**
Li	TF spectra up to T_c, no field-dependence above T_c, ZF spectra up to room temperature.	Phase separated regions of emergent magnetic state and paramagnetism, PM phase becomes superconducting below T_c, main contribution to $B_\mathrm{rms}(T)$ below T_c from vortex lattice, two-gap superconductivity, $\lambda_{ab} = 275(10)\,\mathrm{nm}$.
Na	TF spectra up to T_c, no field-dependence above T_c, no ZF data.	Main contribution to $B_\mathrm{rms}(T)$ below T_c from vortex lattice, two-gap superconductivity, $\lambda_{ab} = 310(20)\,\mathrm{nm}$.
K	TF spectra up to T_c, field-dependence above T_c, no ZF data.	Large magnetic contribution to $B_\mathrm{rms}(T)$, unusual field-dependence confirms non-nuclear origin.

Rb	TF spectra up to T_c, no field-dependence above T_c, no ZF data.	Large magnetic contribution to $B_{rms}(T)$.
Cs	TF spectra up to T_c, field-dependence above T_c, no ZF data.	Main contribution to $B_{rms}(T)$ below T_c from vortex lattice, single s-wave gap, $\lambda_{ab} = 280(10)$ nm, unusual field-dependence of B_{rms} above T_c confirms presence of non-nuclear magnetic phase.
Ca	TF spectra up to T_c, no field-dependence above T_c, no ZF data.	Large magnetic contribution to $B_{rms}(T)$.
Sr	TF spectra up to T_c, no field-dependence above T_c, no ZF data.	Main contribution to $B_{rms}(T)$ below T_c from vortex lattice, single s-wave gap, $\lambda_{ab} = 280(10)$ nm.
Ba	TF spectra up to T_c, no field-dependence above T_c, no ZF data.	Large magnetic contribution to $B_{rms}(T)$.

TABLE 6.3: A summary of the current μSR data set for the intercalates, with key results and interpretations from TF data given in red, while those from ZF data are given in blue.

Chapter 7

NaFeAs under extreme conditions

7.1 Introduction

On discovering any new compound of interest, one wants to gather as much experimental information on it as possible. As demonstrated in Chapter 4, combining the results from several experimental techniques can allow one to build up great understanding of even as rich a system as $\text{NaFe}_{1-x}\text{Co}_x\text{As}$. However, the experiments discussed in Chapter 4 suffer from two key deficiences:

- They were carried out exclusively on powder samples and therefore offer no information on any anisotropy in a measured quantity.
- They only examined the effects of chemical substitution. This is just one way of affecting the properties of pnictide systems and is somewhat controversial (see Chapter 2).

This chapter presents the results of two investigations that seek to fill in some of the gaps in our understanding of this system caused by these deficiencies. The first half of the chapter describes my recent work on single crystal samples of NaFe$_{1-x}$Co$_x$As. High-quality crystals can be grown using the flux method (see Chapter 3) and allow one to study properties that may vary along different crystallographic directions. The critical fields, B_{c1} and B_{c2}, are two such quantities and one can extract a lot of useful information from their values. In particular, I analyse the evolution of $\lambda_{ab}^{-2}(0)$ right across the superconducting dome, and this compliments the ambient-pressure μSR results described in Chapter 4.

The remainder of this chapter describes the results of μSR experiments performed on polycrystalline samples of NaFeAs and NaFe$_{0.97}$Co$_{0.03}$As under applied pressure. It has been shown that systems can be driven from magnetic to superconducting states by pressure just as they can be through chemical substitution [54]. My results will examine whether or not they achieve this through comparable effects on the electronic structure.

7.2 Critical field anisotropy in NaFe$_{1-x}$Co$_x$As

Throughout this thesis, I have emphasised the value of measuring the quantity $\lambda_{ab}^{-2}(0)$ for superconducting samples using TF-μSR. This is a highly valuable quantity as it yields information about both the electronic structure and superconducting gap structure, which are difficult to probe directly. However, as μSR is a local probe of the entire internal magnetic field distribution, the muon signal will contain contributions not only from the vortex lattice, but also from any intrinsic magnetic state present. This means that the accuracy of these measurements may be affected unless the composition is well away from any magnetic phase. Thus, probing the electronic or gap structures in the coexistence regime of NaFe$_{1-x}$Co$_x$As, for example, is difficult to achieve using muons.

Thankfully, there are other ways of accessing this information and this section describes one such method: high-field magnetometry.

Materials with an anisotropic electronic structure will be expected to have similarly anisotropic superconducting properties. In particular, an anisotropic effective carrier mass should lead to an anisotropic coherence length and, consequently, values of the upper and lower critical fields will depend on the direction of the applied field with respect to crystallographic axes [95]. The coherence lengths within the ab-plane and along c are given respectively by $\xi_{ab} = \sqrt{\mu_0 \Phi_0 / 2\pi B^{c}_{\mathrm{c2}}}$ and $\xi_c = \mu_0 \Phi_0 / 2\pi \xi_{ab} B^{ab}_{\mathrm{c2}}$. Using these values, and measured values of B_{c1}, one can extract penetration depth estimates from

$$\begin{aligned} B^{c}_{\mathrm{c1}} &= \frac{\Phi_0}{4\pi\mu_0\lambda_{ab}^2} \log\left(\frac{\lambda_c}{\xi_{ab}}\right), \\ B^{ab}_{\mathrm{c1}} &= \frac{\Phi_0}{4\pi\mu_0\lambda_{ab}\lambda_c} \log\left(\sqrt{\frac{\lambda_{ab}\lambda_c}{\xi_{ab}\xi_c}}\right). \end{aligned} \tag{7.1}$$

The aim, then, is to find accurate ways of measuring both upper and lower critical fields in these two directions. B_{c1} is typically around 100 G [184] in pnictides and is therefore accessible, in principle, using low-field susceptibility measurements provided by a SQUID. B_{c2} is harder to obtain as it is typically somewhere between 10 T and 100 T [185, 186], so one must find an experimental setup capable of reaching these high fields. The pulsed-field system at the Nicholas Kurti High Magnetic Field Laboratory in Oxford is one such system, and the PDO technique (described in Chapter 3) provides a direct and reliable probe of the susceptibility up to 45 T. Both the SQUID and the pulsed-field PDO system probe samples in bulk. As susceptibility data typically do not contain significant contributions from the magnetic state in NaFeAs (due to the small moment size – see References [12, 97] and Chapter 4) one should be able to measure superconducting critical fields well into the coexistence regime.

This approach can be used to obtain an alternative set of $\lambda_{ab}^{-2}(0)$ values right across the superconducting dome of $\mathrm{NaFe}_{1-x}\mathrm{Co}_x\mathrm{As}$, which should reveal more information about the evolution of the Fermi surface with Co substitution. Probing the gap structure is more difficult with this method, but it can be shown that the anisotropy of $B_{\mathrm{c2}}(T)$ can at least confirm the presence of gaps on multiple Fermi surface sections [29]. This will be interesting for $\mathrm{NaFe}_{1-x}\mathrm{Co}_x\mathrm{As}$ in particular, as the form of $B_{\mathrm{rms}}(T)$ obtained from TF-μSR for fully superconducting $\mathrm{NaFe}_{0.975}\mathrm{Co}_{0.025}\mathrm{As}$ suggests only a single gap (note the saturation in $B_{\mathrm{rms}}(T)$ below around $T_{\mathrm{c}}/3$ shown in Fig. 4.10). Measuring B_{c2} will then allow me to confirm whether this is because only one part of the Fermi surface is gapped, or because two gaps which happen to be of roughly of the same magnitude are opened up.

As mentioned in Chapter 3, high-quality single crystal samples are required for the study of any anisotropic quantity and I therefore begin this section by discussing the preparation of such crystals. All the samples discussed in this chapter were synthesised by myself.

7.2.1 Single crystal synthesis and characterisation

Single crystals of $\mathrm{NaFe}_{1-x}\mathrm{Co}_x\mathrm{As}$, with nominal $x = 0$, 0.01, 0.02, 0.03, 0.05 and 0.08, were synthesised using the flux method. Freshly cut Na pieces, along with ground Fe, Co and As, were mixed in the molar ratio $\mathrm{Na} : \mathrm{Fe}_{1-x}\mathrm{Co}_x : \mathrm{As} = 3 : 1 : 3$ and sealed under Argon in a Nb tube. This was heated to 300°C in order to form a mixture of NaAs alloy and transition metals, which was then ground together. After this second grinding, the mixture was placed into an alumina crucible which was itself placed into a second Nb tube that was then sealed under Argon. This Nb tube was encapsulated in an evacuated silica ampoule and heated up to 900°C. It was then cooled to 400°C at a rate of 5°C/hr, and quickly cooled from there to room temperature by switching off the furnace.

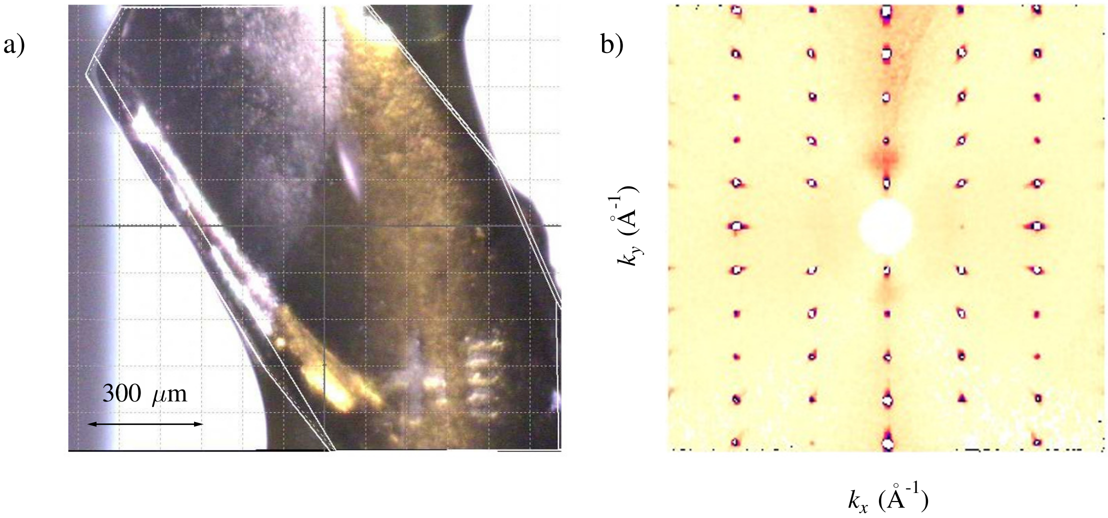

Figure 7.1: (a) A photograph of a single crystal of NaFeAs, mounted in Apeizon-N grease on a 300 μm microloop. (b) The $0kl$ plane from the same crystal, as measured by the SuperNova.

The resulting crystals, with typical dimensions of around $300 \times 300 \times 50\,\mu\mathrm{m}^3$, were mechanically chipped from the flux and did not appear to suffer any damage during this process. A photograph of an undoped NaFeAs crystal is shown in Fig. 7.1(a); large, shiny facets are clearly visible and these suggest a successful growth. To be assured of quality, however, the usual characterisation procedures were carried out. Firstly, using the Oxford Diffraction Supernova (see Chapter 3) and the accompanying Crysalis Pro software package, confirmation of phase purity was easily achieved by XRD as over 99% of observed peaks could be accounted for by the NaFeAs structure. Given the resolution of the instrument, and the probable presence of small amounts of flux still sticking to the crystal, I believe that this result confirms that these samples contain no impurity at any level that could affect the results of subsequent experiments.

In order to assess the stoichiometry of these samples – i.e. whether or not the nominal level of Co had been incorporated – I made use of susceptibility data (just as I did for powder samples) and such data for all my crystals are shown in Fig. 7.2(a). These data were all taken in an applied field of 100 G, after being cooled in zero field. The mass of a typical crystal grown as described above is roughly 0.5 mg so, in order to maximise the signal at low fields, several crystals from the same batch were used in each measurement. Anticipating the anisotropy of B_{c1} (also measured using the SQUID), these crystals were coaligned such that the applied field would be parallel to either the *c*-axis or to the *ab*-planes. The data shown in Fig. 7.2(a) were all taken with the field directed parallel to the *c*-axis.

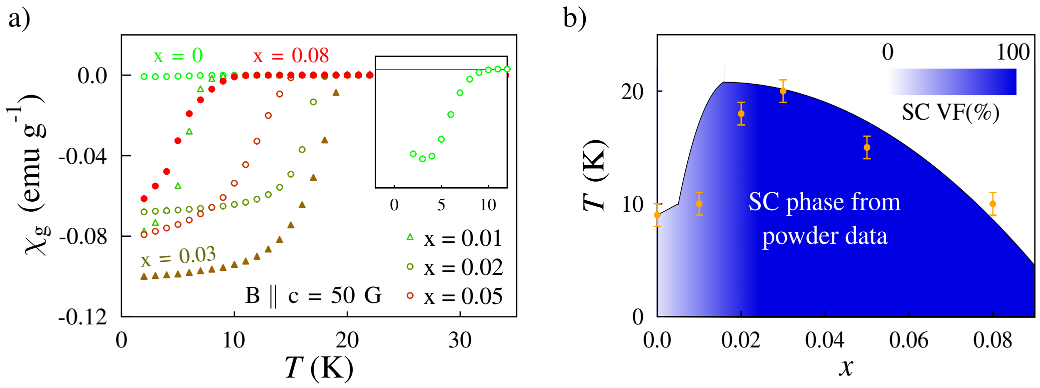

FIGURE 7.2: (a) Susceptibility data for all single crystal samples. These data were taken in 100 G on ∼ 3 mg samples containing several coaligned crystals, following cooling in zero field. The inset merely highlights the much smaller response of the $x = 0$ sample. (b) The extracted values of T_c for the crystal samples, superimposed on the superconducting part of the phase diagram composed from powder sample data (Fig. 4.13). The T_c values measured for overdoped samples are as expected, while there is a discrepancy, possibly indicating a lower-than-nominal incorporation of Co, in underdoped samples.

Extracted values of T_c for all these samples are plotted in Fig. 7.2(b), on which I also show the region of superconductivity defined by the powder samples studied in Chapter 4. I take the stoichiometry of these powder samples to be accurate, as it was also confirmed using XRD[1]. One can see that the T_c values measured for the crystal samples match

---

[1] In a powder XRD experiment, one can mix a compound with a known structure into one's sample, and use the diffraction peaks from this extra compound to calibrate instrumental offsets. This cannot be

those from the powder samples on the overdoped side of the phase diagram quite well. By contrast, this plot would suggest that the nominal $x = 0.01$ and $x = 0.02$ compositions actually contain slightly less Co, though the error on x could not be more than 0.005.

Because the discrepancy between the nominal and true levels of Co substitution in these crystals is small at most, I will refer to these samples by their nominal values of x in what follows. Though the SQUID data suggest a discrepancy in underdoped samples, it should be noted that this method, in isolation, is not a definitive measure of stoichiometry. More accurate information can be gained using Energy-Dispersive X-ray Diffraction (EDX), and this is a priority for future work.

Finally, I note that the superconducting transitions identified by these data are, particularly in the compositions closest to optimal doping, sharp (χ_g begins to saturate within a few degrees of T_c in the samples with the highest volume fraction). This indicates a homogeneous incorporation of Co, which is expected from the results of EDX experiments on other systems [151] .

7.2.2 Low-field DC magnetometry for B_{c1}

The determination of the lower critical field was also carried out using the SQUID, specifically by measuring the field-dependence of the magnetisation, $m(B)$. An example of such data, from the $x = 0.02$ composition, is shown in Fig. 7.3(a).

Below B_{c1} one would expect the complete expulsion of the field to give rise to a linear $m(B)$, so B_{c1} was therefore defined as the point of departure from linearity, as shown in Fig. 7.3(a)(*Inset*). In this way, values of B_{c1} were determined for all samples with

---

reliably done in single crystal XRD, meaning that the lattice parameters extracted from single crystal experiments are less accurate than those from equivalent powders. Because of this I did not perform a comparable study of lattice parameter evolution with which to assess Co concentration in my crystals.

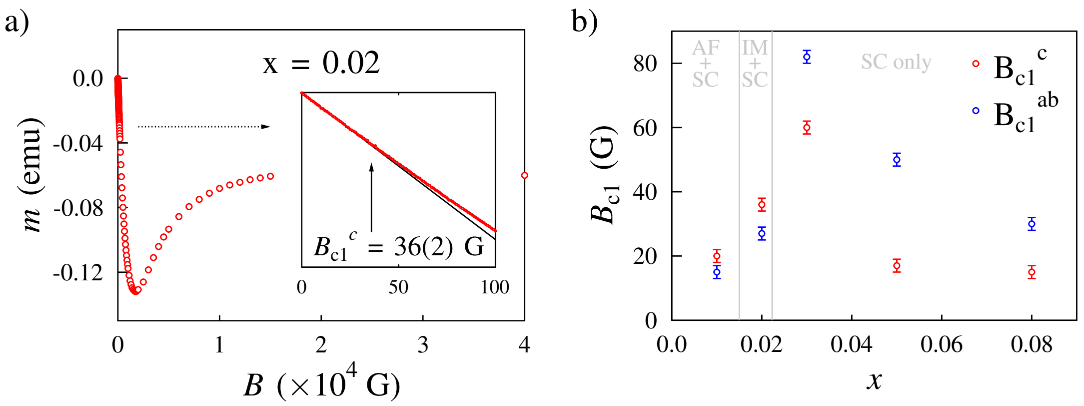

FIGURE 7.3: (a) Measuring the moment $m(B)$ at 2 K ($T \ll T_c$) allows for the extraction of B_{c1} as the point of departure from linearity, as shown in the *Inset*. When obtaining these data, the field was applied parallel to the crystallographic c-axis following cooling in zero-field. (b) Extracted values of B_{c1} are plotted against the nominal Co concentration, x, in these samples. Also highlighted are the regions of antiferromagnetism (AF) and inhomogenous magnetism (IM), as well as superconductivity, from the phase diagram in Fig. 4.13.

the applied field in one of two possible directions; either parallel to the c-axis or the ab-planes. The extracted values for each sample are plotted in Fig. 7.3(b), which also shows which compositions contain antiferromagetic (AF) and inhomogenous magnetic (IM) phases (see Fig. 4.13). It is anticipated that the value of B_{c1} (and B_{c2} for that matter) should scale with T_c, hence the peak in both values of B_{c1} at optimal doping. However, the fact that there appears to be a crossover beyond $x = 0.02$, concerning which of B_{c1}^{c} and B_{c1}^{ab} is the greater, is currently unaccounted for. It is interesting that this corresponds to the point where any magnetic order has vanished.

I note at this point that none of the data obtained from the SQUID were corrected for the shape-dependent demagnetisation factor (explained in Chapter 4). This correction could have an effect on the shape of these magnetisation curves, and consequently alter my estimates of B_{c1}.

7.2.3 Pulsed-field magnetometry for B_{c2}

The evolution of the anisotropic upper critical field with doping was measured using the PDO technique combined with a pulsed-field system. In this method, the susceptibility of the sample affects the resonant frequency of an LCR circuit so, as the susceptibility of a superconducting sample dramatically changes below the critical surface, B_{c2} can be defined as the field at which this frequency $[f(B)]$ matches that measured for the sample in the normal state. The data subsequently presented were all obtained and analysed by Saman Ghannadzadeh and Paul Goddard, so I shall only present the key results of these experiments here. More details can be found in Reference [187].

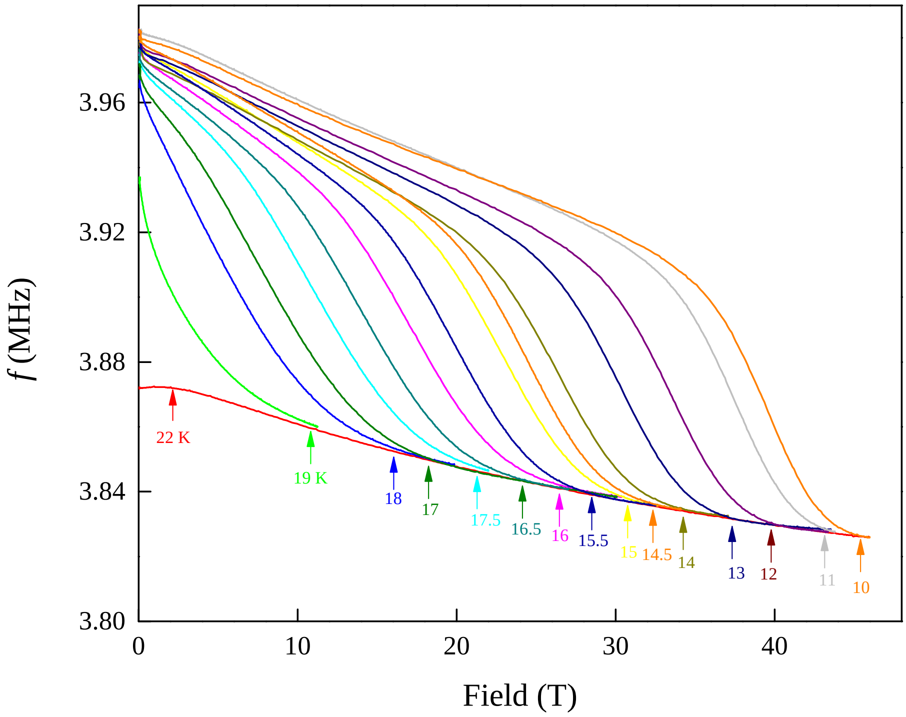

Figure 7.4: The resonant frequency of the LCR circuit in the PDO system, when containing a single crystal of $NaFe_{0.98}Co_{0.02}As$. The field is applied parallel to the *ab*-planes and swept up at various temperatures (arrows). B_{c2}^{ab} is defined as the field at which the frequency matches that measured in the normal state (the 22 K line).

Figure 7.4 shows $f(B)$ data for a single crystal of $NaFe_{0.98}Co_{0.02}As$, taken at various temperatures. The field in this case was applied parallel to the *ab*-plane. A scan of $f(B)$ was taken above $T_c = 18(1)$ K to use as the normal state marker (the 22 K line); the point at which the $f(B)$ curve for a particular temperature joined this line was defined as B_{c2}^{ab}, and such points are shown by the arrows in Fig. 7.4.

Figure 7.5 shows the extracted behaviour of $B_{\mathrm{c2}}(T)$, measured with B applied parallel to either the c-axis or the ab-planes. All samples were covered in dried out Apiezon-N grease during these measurements to prevent the oxidation of the surface. Unfortunately, this procedure was not enough to prevent the degradation of the NaFeAs sample, for which only data taken with B parallel to c were obtained. However, as superconductivity may well be filamentary in this compound (note the low volume fraction in Fig. 4.13), $B_{\mathrm{c2}}(T)$ data may not relate to the superconducting state that emerges at higher doping levels.

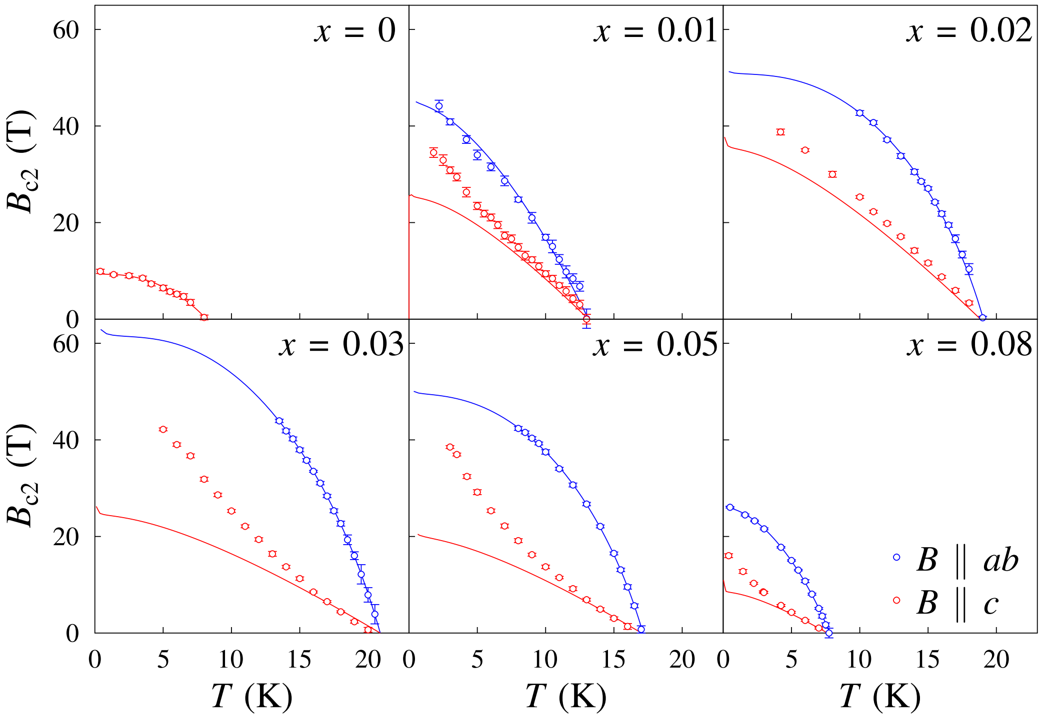

FIGURE 7.5: $B_{\mathrm{c2}}(T)$ data for the $\mathrm{NaFe}_{1-x}\mathrm{Co}_x\mathrm{As}$ series, obtained from pulsed-field magnetometry measurements on a series of single crystal samples. For NaFeAs, sample degradation meant that only data taken with B directed parallel to the c-axis were obtained. The lines shown are the results of fitting to the WHH model (see text).

The lines fitted to the data in Fig. 7.5 are from the Werthamer-Helfand-Hohenberg

(WHH) model [188]. This is appropriate for a single-band superconductor so it is interesting to note that it only appears to work for one field alignment – with B parallel to the ab-planes. When B is directed along the c-axis, it turns out that a two-band fit is required but this is not shown as the two-band WHH model is highly overparameterised (that is, many different values of fitting parameters give fits of the same statistical quality). I therefore say no more about this fitting, except to emphasise that a single-band fit describes the form of $B_{\mathrm{c}2}^{ab}(T)$ but a two-band model is required for $B_{\mathrm{c}2}^{c}(T)$.

There are two physical effects that limit the value of $B_{\mathrm{c}2}$: pair-breaking due to Zeeman splitting of Cooper pairs (the "paramagnetic limit") and the formation and eventual overlap of Abrikosov vortices (the "orbital limit"). The former effect is isotropic, as a field will break singlet pairs regardless of its orientation. The latter, however, may affect $B_{\mathrm{c}2}$ differently along different directions, depending on the topology of the Fermi surface on which the normal state electrons within the vortices reside. The precise interplay of these two effects is intricate but one can see how a two-band fit will not be necessary when the field is applied within the planes; in such a configuration, electrons will undergo open orbits in the k_z-direction along the cylindrical Fermi surfaces in these compounds, and so any differences between the sizes of these cylinders will not affect their motion. A two-band model is clearly required when these electrons are made to orbit around the circumference of these cylinders, which will have different sizes and appear in ARPES data to be differently warped [106, 189].

Multiband superconductivity in these compounds is also confirmed by the temperature-dependence of the critical field anisotropy ($\gamma_B = B_{\mathrm{c}2}^{ab}/B_{\mathrm{c}2}^{c}$), which is close to unity at low temperatures but increases on approaching T_{c} in all samples. This is clear from the data in Fig. 7.5 but is explicitly plotted in Fig. 7.6(a). The author of Reference [29] demonstrated that single-band superconductors must have a flat anisotropy (i.e.

γ = constant) and found that different forms of $\gamma(T)$ emerge when more than one gap (each with a different value of carrier diffusivity) was present. From these data, it is clear that more than one part of the Fermi surface must be gapped.

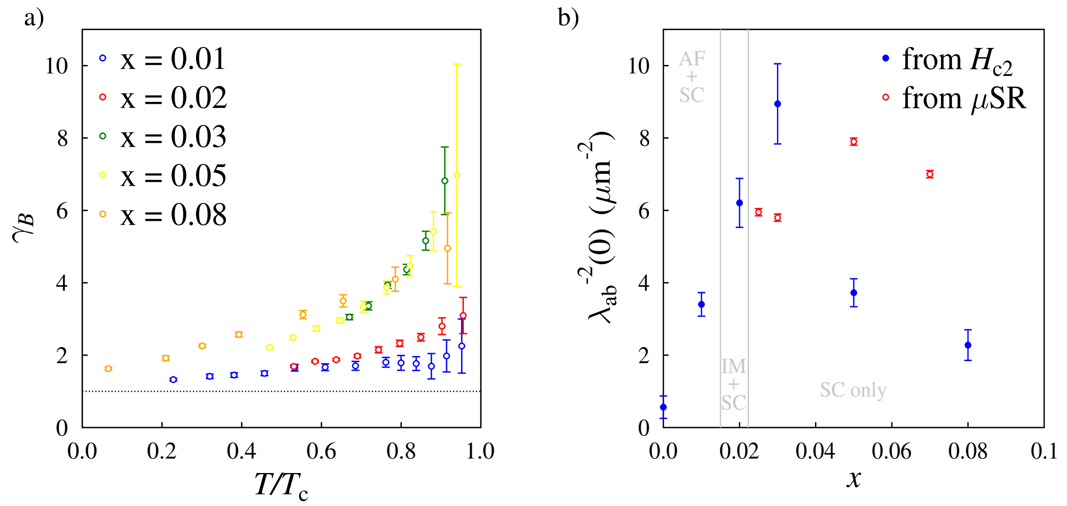

FIGURE 7.6: a) The temperature dependence of the anisotropy, $\gamma_B = B_{c2}^{ab}/B_{c2}^{c}$, extracted from the data shown in Fig. 7.5. Observing any temperature dependence in γ_{B} is indicative of multiband superconductivity [29]. b) Values of $\lambda_{ab}^{-2}(0)$ (filled circles) extracted from Eq. 7.1 using measured values of $B_{c2}(0)$. Also shown for comparison is the data from μSR (open circles) and the relevant regions of the phase diagram (grey).

From all the critical field data, it is possible to estimate the penetration depth and coherence length across the series using Eq. 7.1. Of particular interest is the in-plane penetration depth as these values can be directly compared with those obtained from μSR (in this work and Reference [12]). Values measured using both techniques are shown in Fig. 7.6(b). Encouragingly, these two sets of data are of the same order of magnitude, though their are some discrepancies on the overdoped side of the phase diagram in particular. These can be put down to the sensitivity of the value of λ_{ab} estimated from Eq. 7.1 to the value of B_{c1}, and my method of extracting B_{c1} is possibly somewhat simplistic. However, as it was applied systematically across the series, the trend established by these values of $\lambda_{ab}^{-2}(0)$ should be valid. This trend agrees with that found in other Fe-based superconductors [190] and is easily explained: At low doping levels magnetic order reconstructs the Fermi surface, generally reducing the size of various pockets and, by the Chandrasekhar result, reducing $\lambda_{ab}^{-2}(0)$. As doping increases and magnetic order is suppressed, the Fermi surface grows and $\lambda_{ab}^{-2}(0)$ rises. The peak in $\lambda_{ab}^{-2}(0)$ at optimal doping, followed by a reduction on the overdoped side, suggests that continual electron doping begins to reduce the overall size of the Fermi surface. This is supported by studies of electron-doped $\mathrm{Ba(Fe_{1-x}Co_x)_2As_2}$ [77].

Finally, one can also calculate the values of the anisotropic coherence length from the extrapolated values of $B_{c2}(0)$. For instance, in the $x = 0.01$ composition, one finds $\xi_c \simeq 2.5\,\mathrm{nm}$ and $\xi_{ab} \simeq 3\,\mathrm{nm}$. Respectively, these values are roughly two and three times greater than the dimensions of the assumed magnetic unit cell in this composition [102], so one would not expect an internal magnetic field from the ordered moments to break up Cooper pairs, and influence B_{c1}, as the field from the moments varies over too small a length scale. It may have been tempting to use such an argument to account for the aforementioned crossover in the values of B_{c1} (Fig. 7.3), but this appears to be invalid.

In conclusion, the principal achievement of this work is the analysis of how the electronic structure evolves over the entire superconducting dome in $\mathrm{NaFe_{1-x}Co_xAs}$, which could not be achieved using μSR. In addition, I have confirmed that multiple parts of the Fermi surface are gapped, which was not clear from the data presented in Chapter 4.

7.3 NaFeAs and $\mathrm{NaFe_{0.97}Co_{0.03}As}$ under pressure

Chemical substitution is a simple way of tuning NaFeAs from an antiferromagnet to a superconductor, and the results in the previous section are neatly interpreted in terms of the corresponding evolution of the Fermi surface as one carries out this tuning. However, as discussed in Chapter 2, the exact means by which substitution affects the electronic structure is not clear, so it is useful to study other ways of tuning the system whose precise effects may be easier to understand. Applying pressure is one such method and, as it introduces no extra charge or possible magnetic impurity, its effects on the electronic structure should be easier to calculate. To the best of my knowledge, such calculations have not yet been performed for NaFeAs, so the data I present here provide predictions for what these calculations should find.

ZF- and TF-μSR data were taken for polycrystalline samples of $\mathrm{NaFe_{0.97}Co_{0.03}As}$ and NaFeAs, which should be fully superconducting and fully magnetic respectively. Resistivity measurements under pressure [191] show that the superconducting transition temperature rises in the undoped compound, apparently at the expense of magnetic order. μSR can probe this directly, allowing one to measure the response of the size of the ordered moment as well as the ordering temperature (T_{N}). The superconducting T_{c} also goes up with pressure in the optimally doped compound, so it will be interesting to see what happens to $\lambda_{ab}^{-2}(0)$.

These samples were prepared and characterised according to the methods described in Chapters 3 and 4, so there is no need to describe these processes again here. Samples were loaded into a CuBe pressure cell, in which they could be manually compressed up to $\sim 20\,\mathrm{kbar}$. Because of the thickness of the pressure cell walls, decay muons were required (see Appendix B) and so all data were taken on the GPD Spectrometer at PSI. The muon signal from the cell was obtained when empty and included in all subsequent fitting as a background component.

7.3.1 The evolution of the magnetic phase in NaFeAs

Figure 7.7(a) shows the asymmetry spectra for NaFeAs in the pressure cell (though at ambient pressure) at 5 K. One can clearly see a multi-component oscillation, as expected from Fig. 4.5, superimposed upon a slow relaxation from the cell itself. ZF spectra were obtained at various temperatures up to 55 K and at three pressures: ambient (1 bar), 9.6 kbar and 24 kbar.

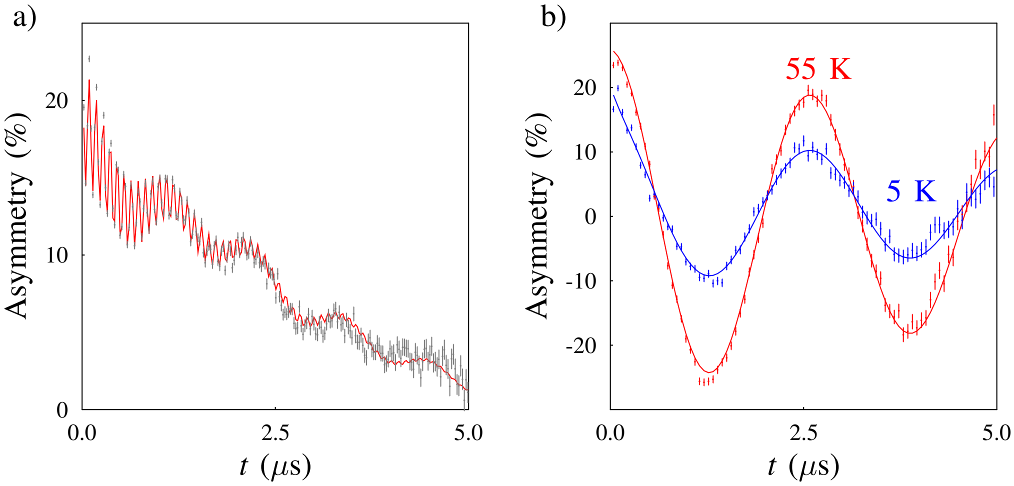

FIGURE 7.7: (a) The ZF asymmetry spectra of NaFeAs and the pressure cell at 5 K. (b) The spectra taken above and below T_N in a weak transverse-field of 30 G. In both cases, data were taken at ambient pressure.

These data were fitted to the following function:

$$A(t) = A_\mathrm{c} G_\mathrm{KT}(\Delta_\mathrm{c}, t)\mathrm{e}^{-\Lambda_\mathrm{c} t} + \sum_{i=1,2,3} A_i \cos(\nu_i t)\mathrm{e}^{-\lambda_i t}. \tag{7.2}$$

The signal from the cell is decribed by the first term, a Kubo-Toyabe function with a width, Δ_c, and weak exponential relaxation, Λ_c, that were both fixed. The signal from the sample is, as expected from Eq. 4.1, described by a superposition of three cosine functions, each with their own frequency (ν_i) and exponential damping (λ_i). Once again, these indicate three distinct muon sites, each with their own value of the local field. The values of A_i combined to just less than half of the total relaxing asymmetry, so half of the incident muons stopped in the sample and half in the cell. Because of this, long runs ($\sim$ 2 hrs per temperature) were required in order to obtain data of a sufficient statistical quality to be able to accurately extract $\nu_i(T)$.

Some information, however, could be obtained more quickly by taking data in a weak transverse-field (30 G in this case) and studying the behaviour of the amplitudes of various parts of the signal. Even in spectra from short ($\sim$ 20 min) runs, in which the comparatively fast oscillations from muons in the sample cannot be resolved, one can still see a damping of the slow 30 G oscillation from these muons below T_{N}. This is shown in Fig. 7.7(b). Analysing the amplitude of the damped component as a function of temperature provided a quick means of determining T_{N} at high pressures. These TF data were fitted to the function

$$A(t) = A_{\mathrm{c}} \cos(\gamma_\mu B_{\mathrm{app}} t) \mathrm{e}^{-\Lambda_{\mathrm{c}} t} + A_{\mathrm{mag}} \mathrm{e}^{-\lambda_{\mathrm{mag}} t}, \tag{7.3}$$

with $A_{\mathrm{mag}}(T)$ the quantity of interest (λ_{mag} was fixed to its value at base temperature throughout the fitting).

The results of fitting both ZF and TF data to Equations 7.2 and 7.3 respectively are shown in Fig. 7.8. The upper panels show the evolution of the three frequencies with temperature at various pressures and the lower panels show the corresponding evolution of A_{mag} obtained from TF data. For the first two pressures at least, the form of $\nu_i(T)$ could be described by a typical order parameter-type dependence, $\nu_i(0)[1 - (T/T_{\mathrm{c}})^\alpha]^\beta$, and the extrapolated zero-temperature values of the largest frequency, ν_1, are shown on the figure. At the highest pressure, such a fit did not work so well because of unusual

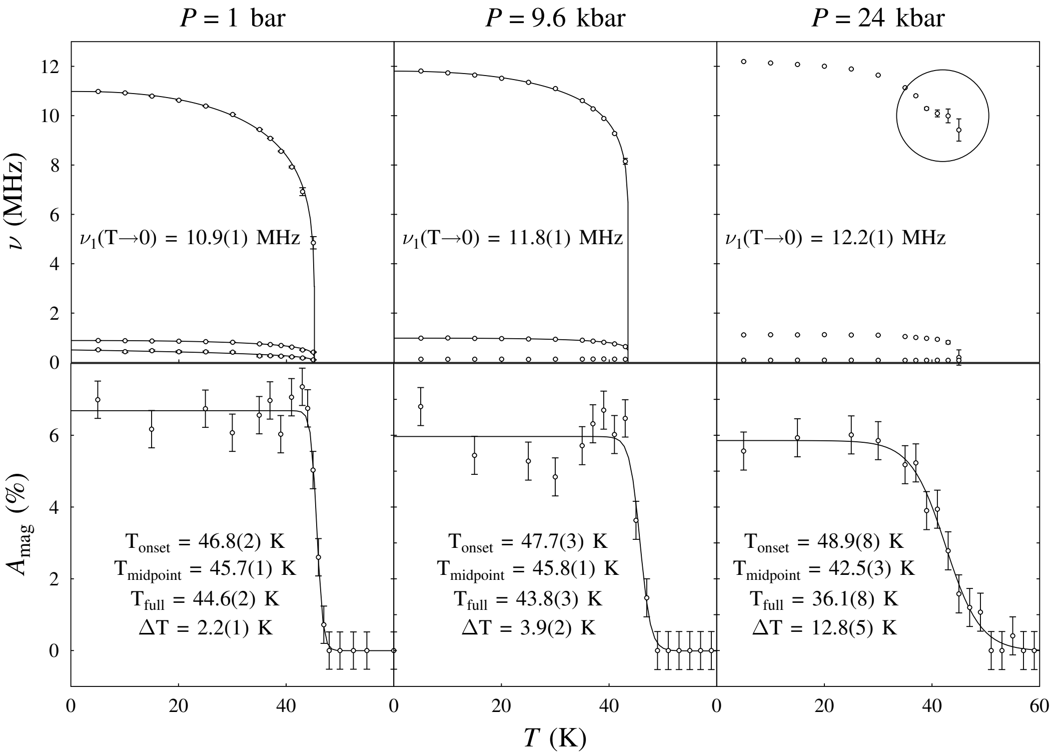

FIGURE 7.8: The results of analysing all data obtained for NaFeAs at the three pressures applied. The upper panels show the behaviour of the three precession frequencies (defined in Eq. 7.2) with temperature, and the extrapolated zero-temperature values (proportional to the size of the ordered moment) are highlighted. The lower panels show the temperature-dependence of the amplitude of the magnetic phase obtained using TF-μSR (30 G). The ordering temperature is then described by a midpoint temperature (T_{midpoint}) and a width (ΔT) that indicates the sharpness of the transition. Also shown are the onset temperature for magnetic order (T_{onset}), and the temperature at which the order is fully established (T_{full}). In the top right panel, an unusual feature in $\nu_1(T)$ is circled (see text).

behaviour around T_{N} (circled in the top right panel). This is probably caused by some phase separation in the sample close to T_{N}, perhaps due to a loss of hydrostaticity in the pressure medium. In the lower panels, the forms of $A_{\mathrm{mag}}(T)$ were fitted to a Fermi function which allowed me to parameterise the magnetic transition by the onset temperature for ordering (T_{onset}), the midpoint temperature (T_{midpoint}), the temperature at which order is fully established (T_{full}), and the width of the transition (ΔT).

It is apparent from this analysis that, on increasing pressure, the ordered moment of NaFeAs (proportional to the precession frequency) also increases. As for the transition temperature, T_{midpoint} and T_{full} clearly decrease, whereas T_{onset} rises slightly due to the increase in the transition width[2], ΔT. The behaviour of the ordering temperature is thus somewhat ambiguous from these measurements, but my results do not conflict with those from the resistivity data of Wang *et al.* [191] that show T_{N} fall as the pressure is raised.

It is interesting to compare these results to those from an almost identical experiment [192] on the 1111 parent compounds LnFeAsO (Ln = La, Ce, Pr, Sm). In these systems, the magnetic ordering temperature goes down with increasing pressure and the transition broadens, as is seen in my data. However, in the 1111 compounds, the ordered moment also decreases with pressure, unlike what happens in NaFeAs. I shall return to this comparison in the Section 7.3.3.

7.3.2 The evolution of the superconducting phase in NaFe$_{0.97}$Co$_{0.03}$As

Due to some technical difficulties when loading the sample, only one reliable data set was obtained for the fully superconducting NaFe$_{0.97}$Co$_{0.03}$As composition; at an applied pressure of 16 kbar. Asymmetry spectra were obtained in a transverse field of 100 G and analysed in the usual way (see Chapters 3 and 5). The evolution of $B_{\text{rms}}(T)$ and $B_{\text{pk}}(T)$, at ambient and the applied pressure, are shown in Fig. 7.9.

It is immediately clear that, as expected from Reference [191], T_{c} increases with pressure by a factor of ~ 1.5. Correspondingly, the value of $B_{\text{rms}}(0) \sim \lambda_{ab}^{-2}(0)$ increases by nearly the same factor, meaning the penetration depth has decreased.

---

[2] indicating a loss of magnetic homogeneity within the sanple.

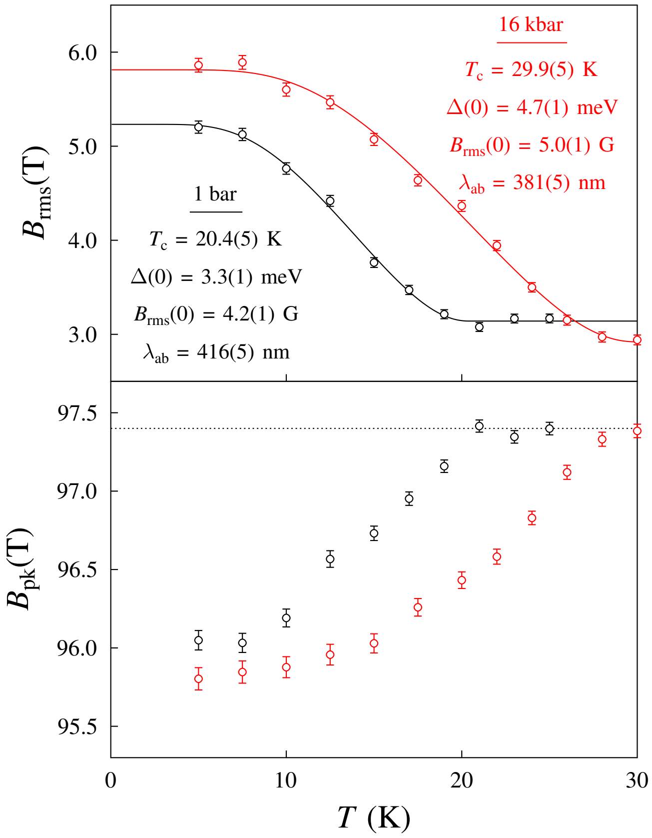

FIGURE 7.9: A comparison of the behaviour of $B_{\mathrm{rms}}(T)$ (upper panel) and $B_{\mathrm{pk}}(T)$ (lower panel) at ambient pressure and at an applied pressure of 16 kbar. The form of $B_{\mathrm{rms}}(T)$ has been fitted to a single-gap dependence (see Appendix C).

In addition, the forms of $B_{\mathrm{rms}}(T)$, at both ambient and high pressure, appear to exhibit single-gap behaviour. The measured anisotropy of B_{c2} for this compound clearly indicates multi-band behaviour, however, so it must be that the gaps on each part of the Fermi surface are of roughly the same magnitude. Indeed, this is confirmed by ARPES measurements on a similar composition [77]. As shown in Fig. 7.9, fitting to a single-gap model (a valid approximation if two gaps of nearly equal magnitudes are present) suggests that the gap structure is unaffected by pressure as the value of $2\Delta(0)/k_{\mathrm{B}}T_{\mathrm{c}} \sim 3.6$ is constant.

7.3.3 Discussion

My pressure study has revealed that both the magnetic and superconducting states are strengthened in some way as the sample is compressed. For the magnetic state, the ordered moment size increases with pressure and in the superconducting state both T_{c} and the value of $\lambda_{ab}^{-2}(0)$ are raised. The former of these results confounds the idea that pressure has the same effect on NaFeAs as chemical substitution. Although both appear to cause T_{N} to go down, my work in Chapter 4 showed that substitution reduces the moment size, whereas pressure increases it. The fact that T_{N} goes down either way suggests that both chemical substitution and applied pressure destroy the nesting of the Fermi surface, and allow a superconducting state to grow in place of the magnetic state. However, they clearly achieve this in very different ways.

The results in this chapter take on additional importance as pressure-dependent experimental studies of the Fermi surface are very difficult to carry out directly[3]. The observed increase in $\lambda_{ab}^{-2}(0)$ in the superconducting state has a fairly straight forward interpretation in light of the Chandrasekhar result (see Reference [96] and Chapter 5); that the overall extent of the Fermi surface and/or the Fermi velocity increases under pressure. At present, few studies of Fermi surface evolution under pressure exist for any Fe-based superconductor, and certainly not for superconducting $\mathrm{NaFe}_{1-x}\mathrm{Co}_x\mathrm{As}$. There is a report of the size of the reconstructed pockets in the magnetic state of $\mathrm{BaFe}_2\mathrm{As}_2$ increasing with pressure [193], and the unreconstructed (normal state) Fermi surface for the 122 compound is similar to that of NaFeAs [106]. To my knowlege, even band structure calculations do not exist for superconducting $\mathrm{NaFe}_{1-x}\mathrm{Co}_x\mathrm{As}$ under pressure, and these would clearly be desirable.

---

[3] This is usually because of the practicalities of including a pressure cell in the apparatus used to measure quantum oscillations, or the fact that such a cell will surround the sample and make ARPES impossible.

The increase in the size of the ordered moment in undoped NaFeAs reveals more still about what happens to the electronic structure under pressure. Data from a similar set of experiments on the 1111 family, showing a decrease in moment size with pressure [192], were explained in that paper as being a consequence of a corresponding increase in the width of the Fe d-bands. Such an increase in bandwidth is expected under pressure because the transfer integrals that define it are raised as atoms are brought closer together [194]. Increasing the bandwidth will decrease the density of states at the Fermi level [$g(E_{\mathrm{F}})$] which, it is claimed in Reference [192], will diminish the system's ability to satisfy the Stoner criterion [$Ug(E_{\mathrm{F}}) \geq 1$] and magnetically order. However, the Stoner criterion really only governs the formation of a ferromagnetic state [98], so the authors of Reference [192] are assuming that a similar dependence on $g(E_{\mathrm{F}})$ applies to the antiferromagnetic case and that the moment size directly depends on how comfortably this criterion is satisfied. If this picture is valid, my results would suggest that applying pressure to NaFeAs reduces the bandwidth. This seems unlikely, however, as atoms are presumably being brought closer together under pressure and the transfer integrals should increase as usual.

For a complete account, then, one requires the evolution of the chemical structure of NaFeAs under pressure. It may be that some unusual structural features of this compound do allow for a decrease in bandwidth, explaining the increase in moment size according to the scheme proposed in Reference [192]. At present, this is not available as obtaining high-resolution structural data at high pressures and the temperatures relevant for magnetism is a challenge. In the meantime, the results of band structure calculations using theoretical structures (like those used in Reference [192]) would be very useful. My results predict that they will find an increase in the overall size of the Fermi surface, particularly in the optimally-doped compound, and that the bandwidth decreases under pressure in the undoped compound.

I conclude by mentioning an upcoming experiment that will add further insight into the interplay of superconductivity and magnetism in this compound. I have measured the response of both fully superconducting and fully magnetic samples to pressure, and found that both $\lambda_{ab}^{-2}(0)$ in the superconducting sample and the ordered magnetic moment size in the magnetic sample increase as pressure is applied. We therefore plan to measure the response of both phases in the coexistence regime, namely in the $\mathrm{NaFe_{0.985}Co_{0.015}As}$ composition (see Fig. 4.13), and this experiment will provide an interesting test of our conclusion that these phases compete and coexist on an atomic length scale. I demonstrated in Chapter 4 that the broadening of the field distrubution in TF contains both magnetic and superconducting contributions that should, using the data shown in Fig. 7.9, be separable. If both the magnetic and superconducting contributions are raised under pressure then doubt would be cast on the atomic coexistence hypothesis. Instead, this would suggest that these phases occupy spatially separated regions of the sample that can both be enhanced simultaneously as they are not in direct competition. However, the NMR data from Reference [101] [albeit on $\mathrm{Ba(Fe_{0.94}Co_{0.06})_2As_2}$] do suggest that the coexistence of these phases is on an atomic scale, so I predict that our upcoming experiments will reveal an enhancement of the superconducting phase at the expense of the magnetic one.

The unusual behaviour of the ordered moment under pressure is worthy of a final comment. The work in Chapter 4 suggested that $\mathrm{NaFe_{1-x}Co_xAs}$ is a typical electron-doped pnictide system. Of course, the experiments and analyses I carried out in that study were highly detailed, and revealed some novel features of the system, such as the diminishment of the moment size with doping, but nevertheless my ultimate conclusion was that the phase diagram (Fig. 4.13) of $\mathrm{NaFe_{1-x}Co_xAs}$ is very similar to that of the more widely studied $Ba(Fe_{1-x}Co_x)_2As_2$ (Fig. 2.5). It is exciting, then, that by extending the variety of techniques used to study $NaFe_{1-x}Co_xAs$, I have found a truly unanticipated feature that suggests that perhaps this system is not so similar to other pnictides as I first thought.

Chapter 8

Conclusion

Understanding the interplay of superconductivity and magnetism is of vital importance for understanding unconventional superconductivity in general. With the ability to probe both the superconducting vortex lattice, and the intrinsic magnetic state of a system, μSR continues to play a key role in this pursuit. That said, throughout this thesis I have demonstrated the value of utilising as many techniques as possible, making particular use of magnetometry and x-ray diffraction.

In Chapter 4, I applied this approach to studying a series of polycrystalline samples of $\mathrm{NaFe}_{1-x}\mathrm{Co}_x\mathrm{As}$, focussing specifically on the low-x regime where magnetic order and superconductivity were expected to be in direct competition. Building on the previous work of others [12], I used a combination of techniques to compose a detailed phase diagram (Fig. 4.13) that highlights the extent of this competition. ZF and TF-μSR, along with dipole field calculations, allowed me to perform a detailed study of the destruction of magnetic order in particular, and I showed that this is primarily driven by a continuous collapse of the moment size as more Co is added. Long-range order evolves into inhomogenous, local order, whose eventual disappearance coincides with the removal of the structural transition, demonstrating that the latter relies on magnetic fluctuations. Although there is debate surrounding the exact mechanism by which Co substitution affects these systems, there is a lot of evidence to suggest that electron doping plays a major role (see Chapter 2) and I therefore interpret my findings in this system as being a consequence of such a process. The work described in this chapter is published in Reference [97].

The work in Chapter 4 suggests that NaFeAs is very similar to other Fe-based superconductors; compare, for example, Fig. 4.13 to the phase diagrams in Fig. 2.5. Chapter 5 then asks how far the isostructural compound LiFeAs resembles these other systems. Firstly, I used TF-μSR to study the evolution of λ_{ab}^{-2} across a series of polycrystalline $\mathrm{LiFe_{1-x}Co_xAs}$ samples. This quantity is known to relate to the electronic structure [96] and the topology of the Fermi surface is suspected to govern the formation of both magnetic and superconducting states (see Chapter 2). Adding the extracted values of $\lambda_{ab}^{-2}(0)$ and T_{c} to the Uemura plot allowed me to make a direct comparison between LiFeAs derivatives and, in particular, widely studied variants of the 122 compound $\mathrm{BaFe_2As_2}$. I found that the reduction in $\lambda_{ab}^{-2}(0)$ with Co concentration in $\mathrm{LiFe_{1-x}Co_xAs}$ resembles that seen in electron-doped $\mathrm{Ba(Fe_{1-x}Co_x)_2As_2}$ but contrasts with what happens in hole-doped $\mathrm{Ba_{1-x}K_xFe_2As_2}$. This suggests that LiFeAs is close, at least in terms of its electronic structure, to the optimally electron-doped versions of other Fe-based superconductors. However, subsequent ZF-μSR and low-field magnetometry studies of $\mathrm{Li_{1-y}Fe_{1+y}As}$ samples revealed magnetic behaviour not yet seen in other systems; namely, the crossover from ferromagnetic to antiferromagnetic correlations between induced itinerant moments on cooling. Additionally, I also observed a freezing of these moments at low temperature and confirmed the dynamic nature of the magnetism in this system using LF-μSR. These observations led me to my final conclusion that LiFeAs does indeed resemble other optimally electron-doped pnictides, but is close to multiple magnetic instabilities that this novel substitution can access. The work in this chapter is published in References [14] and [146].

These two chapters highlight the aforementioned power of the μSR technique in studying unconventional superconductors, so, when an apparently new family of ammonia-intercalated FeSe compounds were discovered with T_{c} values much greater than that in the starter material, I was well placed to use μSR to examine them. Chapter 6 describes my ZF and TF-μSR studies of compounds made by intercalating $\mathrm{NH_3}$ and various Group I and Group II metals between FeSe layers using soft chemistry techniques. Of particular interest was whether it matters which metal one chooses to intercalate, or whether the act of separating FeSe layers with anything is sufficient to drive the observed increase in T_{c}. The similarities in the values of T_{c} across the series suggest that the precise details of the intercalated layer do not matter; T_{c} is somewhere between 30 K and 45 K in the intercalates, and indeed close to 40 K for most, compared to 8 K in $\mathrm{Fe_{1.01}Se}$. My TF-μSR work showed that, for those samples whose spectra are dominated by a contribution from a superconducting vortex lattice, their values of $\lambda_{ab}^{-2}(0)$ are also similar. However, my ZF-μSR work on the Li-intercalate suggests that these samples contain spatially separated regions of emergent magnetism, in amongst a paramagnetic, superconducting fraction. The contrubution of this phase to the muon signal greatly varies from one compound to another, suggesting that, while the intercalated species may not have much impact on superconducting properties, magnetic properties are highly dependent on it. Much of this work, in both establishing the true extent of these variations and what drives them, is ongoing, but some of the data presented for the Li-intercalate is published in Reference [82].

Finally, Chapter 7 builds on the work of Chapter 4 by returning to the $\mathrm{NaFe_{1-x}Co_xAs}$

system and studying various compositions under high magnetic fields and high pressures. Using a pulsed-field system, measurements of the DC susceptibility were made up to 45 T on a series of single crystal samples. Using this method, I was able to confirm multiband superconductivity in this system as well as measure $\lambda_{ab}^{-2}(0)$ right across the superconducting dome. This is impossible to achieve with ZF-μSR alone as the muon couples to the itinerant Fe moments, as well as the vortex lattice, in the coexistence regime ($x < 0.0225$). High-pressure μSR studies of powder samples then allowed me to explore an alternative way of driving the system from a magnetic to a superconducting state. The optimally-doped compound showed an expected increase in T_{c} and $\lambda_{ab}^{-2}(0)$, the latter result suggesting an increase in the overall size of the Fermi surface. Intriguingly, although pressure was shown to promote superconductivity in the optimally-doped compound, it was also shown to increase the size of the magnetically ordered moment in the undoped compound. This conflicts with results from a similar study of the 1111 compounds, and suggests that the electronic structure of NaFeAs responds to pressure in an unprecedented way, with a decrease in the width of the Fe *d*-bands. This may mean that NaFeAs is, in the end, not quite as similar to other pnictides as my work in Chapter 4 implies.

Appendix A

Theoretical background and technical details concerning XRD

This appendix contains some of the theoretical and technical considerations behind the discussion of x-ray diffraction given in Chapter 3. Following a derivation of some of the key equations that describe the formation of a diffraction pattern, I then give more information on the equipment used to obtain these data and the numerical procedures used to analyse them.

A.1 Theoretical considerations

A diffraction experiment can be modelled as an incoming wave, with vector $\mathbf{k}$, being scattered by a periodic[1] potential $V(\mathbf{r})$ and emerging as a wave with vector $\mathbf{k}'$. This process is assumed to be elastic, so $|\mathbf{k}| = |\mathbf{k}'|$. Following Fermi's Golden Rule, one can show that the scattering matrix element $\langle \mathbf{k}|V(\mathbf{r})|\mathbf{k}'\rangle$, under the plane wave approximation, is given by

$$\langle \mathbf{k}|V(\mathbf{r})|\mathbf{k}'\rangle = \frac{1}{L^3}\sum_{\mathbf{R}} \mathrm{e}^{-i(\mathbf{k}'-\mathbf{k}).\mathbf{R}} \int_{\text{unit cell}} \mathrm{d}\mathbf{x}\, \mathrm{e}^{-i(\mathbf{k}'-\mathbf{k}).\mathbf{x}}\, V(\mathbf{x}). \tag{A.1}$$

Here the vector from the origin to the point of scattering, $\mathbf{r}$, has been written as the sum of a lattice vector, $\mathbf{R}$, and the vector $\mathbf{x}$, which connects the unit cell origin to the point of scattering. The periodicity of the potential, $V(\mathbf{x}+\mathbf{R}) = V(\mathbf{x})$, has also been explicitly used.

---

[1] such that $V(\mathbf{r}+\mathbf{R}) = V(\mathbf{r})$, where $\mathbf{R}$ is a lattice vector.

Equation A.1 reveals two key contributions to the amplitude for scattering. Firstly, the sum is only non-zero when $\mathbf{k}' - \mathbf{k} = \mathbf{G}$, where $\mathbf{G}$ is a reciprocal lattice vector. This condition, known as the "Laue condition", will generally not be met for an arbitrary incoming wavevector; one must vary the incoming wavevector continuously in order to find the discrete set of instances where the condition is satisfied. This is done by varying either the angle of incidence or the wavelength of the incoming beam.

Each reciprocal lattice vector corresponds to a set of crystal planes[2], so each set of planes contributes one spot or peak to the diffraction pattern. The intensity of these peaks are governed by the second contribution, the integral in Eq. A.1 – known as the "structure factor". Essentially, this contains all the information about how atoms are arranged within these crystal planes, their species and how, if at all, they are moving due to thermal excitation. Extracting this information from a diffraction pattern is discussed in Section A.3.

Incidentally, the potential $V(\mathbf{x})$ in Eq. A.1 is worthy of brief discussion. The exact form of $V(\mathbf{x})$ depends on the nature of the interaction between the incoming wave or particle and the atoms. For x-rays, the interaction is electrostatic and is with the electron cloud, thus the intensity of peaks in an x-ray diffraction (XRD) pattern depends on the atomic number Z relevant to that atomic plane. For neutrons, and ignoring the case of magnetic order, the interaction is with the atomic nucleus and due to the strong-nuclear force. The strength of this interaction is governed by the details of the nuclear structure, but has no dependence on Z. This makes neutron diffraction a powerful tool for examining structures of compounds containing light (low-Z) atoms, and indeed this was used to confirm the structurs of my three series'.

A.2 X-ray sources and equipment

All of the diffraction experiments undertaken by the author during this project used x-ray sources (although some results obtained by colleagues using neutron sources will be presented). They are as follows:

- **PANalytical XPert Pro**: this machine is designed for powder diffraction measurements at room temperature. By definition a powder sample will contain many crystallites, typically of a few microns each in dimenion, which are randomly orientated with respect to the beam direction and this results in the effective variation of the incident wavevector. However, in order to extract as much data as possible

---

[2] labelled by the "Miller indices", $\{h, k, l\}$, defined such that planes intersect the crystallographic axes a, b and c at a/h, b/k and c/l respectively.

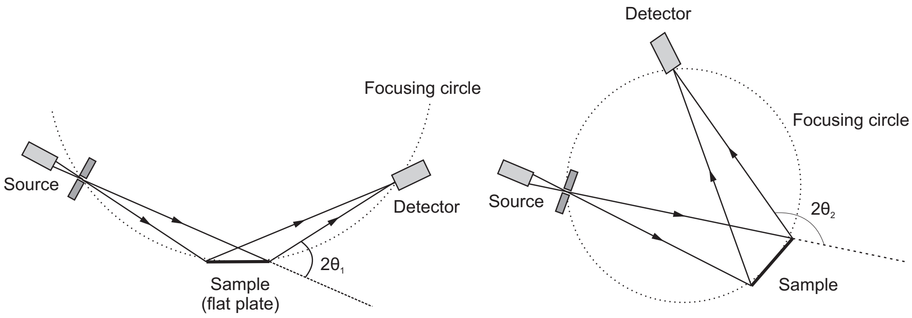

FIGURE A.1: A schematic depiction of the Bragg-Brentano gemoetry employed by the PANalytical XPert Pro Diffractometer. The sample plate rotates at half the angular velocity of the detector so as to remain at a tangent to the focussing circle. Intensity is recorded as a function of 2θ defined as shown. Figure taken from Reference [30].

the relative orientation of the sample mount with respect to the detector is continuously varied over a specified angular range, so that every crystallite will contribute intensity from several allowed reflections. Specifically, this diffractometer operates in "Bragg-Brentano" geometry, as shown in Fig. A.1. This diagram also defines the angular variable 2θ, aginst which the reflected intensity is recorded. Samples are mounted on flat plates which, if they are prone to reacting with oxygen or moisture, may be placed into air-tight containers with transparent windows. To generate x-rays, electrons are stripped from a hot tungsten filament before being accelerated and fired into a Cu target. They excite the $K_{\alpha 1}$ transition which produces x-rays with $\lambda = 1.54051\,\text{Å}$.

- **Oxford Diffraction SuperNova**: this machine is designed for single crystal diffraction measurements. Like the XPert, this machine uses a fixed wavelength beam ($\lambda = 0.71\,\text{Å}$) in this case generated from K-shell transitions in molybdenum. The sample, typically around 1 mm in length, is mounted on the end of a microloop and in turn on a goniometer that can rotate the orientation of the sample through the full solid angle.

- **ID31 High-resolution diffractometer, ESRF**[3]: The ESRF makes use of *synchrotron radiation*. When relativistic electrons are bent in a magnetic field, as in a synchrotron, a beam of highly intense x-rays (comprising many wavelengths) is emitted tangentially to the direction of travel. At the ID31 beamline – optimised for powder diffraction – this radiation is monochromated by two silicon crystals, the (111) reflections of which select the wavelength to be 0.4 Å. Samples are mounted in borosilicate glass capilliaries that spin over the course of the measurement to optimise powder averaging, and a He-cooled flow cryostat allows for data to be taken down to 4 K. Like the XPert, the detectors are rotated with respect to the sample (in this case about the axis defined by the capilliary), so again intensity

---

[3] Grenoble, France.

is recorded as a function of the scattering angle 2θ. The high brightness of the beam not only shortens collection times down to a few minutes, but also makes the resolution of this instrument among the highest in the world.

A.3 Analysing diffraction data

The way in which one calculates the structure of a compound from diffraction data depends on what one already knows. This project dealt exclusively either with compounds of known structure or with structurally close derivatives. For powder samples, this makes the situation relatively simple, as the published structure can then act as an input model to be refined. Two numerical procedures were used to do this; Rietveld and Pawley refinement.

The **Rietveld method** inputs a model containing, at the very least, information on the unit cell, the space group and the atomic species and their locations within the cell. A theoretical diffraction pattern is generated from this, such that the calculated intensity at every point (y_{ci}) is given by

$$y_{ci} = y_{bi} + s \sum_{hkl} L_{hkl}\, P_{hkl}\, A \left|F_{hkl}\right|^2 \psi(2\theta_i - 2\theta_{hkl}), \tag{A.2}$$

where F_{hkl} is the structure factor; the integral in Eq. A.1. L_{hkl} is the *Lorentz factor* which accounts for detector geometry, the polarisation of the beam and the multiplicity of a peak [4]. P_{hkl} accounts for any *preferred orientation* of crystallites with respect to the incident beam: for instance, layered compounds often grow as platelets that will tend to lie flat, biassing the powder average and giving the $(00l)$ reflections extra intensity. The factor A accounts for absorption of the beam by the sample and $\psi(2\theta_i - 2\theta_{hkl})$ is a *peak profile function*, which is often partly instrument-dependent. The other factors in this expression are the background intensity, y_{bi} (often described by a simple polynomial) and a scale factor, s, which accounts for data acquisition time. The resulting theoretical curve is fitted to the data through a conventional least-squares optimisation procedure, and the model is thus refined.

If one is attempting to describe the data from a compound with an unknown structure, the Rietveld method is not suitable unless one can make a remarkably accurate guess for the starting model. The **Pawley method** was originally developed to assist this

---

[4] In a powder experiment one collapses the image of the reciprocal lattice down to a 2D plot of intensity vs 2θ. Thus, reflections from sets of planes with the same spacing will all contribute intensity to the same peak. The number of different reflections contained within a peak is the *multiplicity* of that peak.

procedure by obtaining just the unit cell geometry [195]. Unlike in the Rietveld method where the intensity is calculated, here it is treated as a variable, but arbitrary, quantity. The peak positions will, it is assumed, be solely dependent on the unit cell dimensions and these are the meaningful quantities to emerge from a Pawley fit. Some effects, particularly preferred orientation, are intrinsically difficult to parameterise in Rietveld refinement and were found at times during this project to be large enough to prevent any statistically satisfactory fitting from being achieved. In such cases where unit cell parameters were the only objects of interest anyway, Pawley refinement provided a simpler and quicker way of describing the data.

More details on both methods can be found in Reference [88]. The software used to carry out Rietveld refinement was the GSAS package [85], along with a graphical user interface EXPGUI [86]. Pawley fits were done using TOPAS [87].

For single crystal data, the procedure was slightly different. The software accompanying the SuperNova, CrysAlis Pro, effectively calculates the structure that best describes a given dataset from scratch. It achieves using a trial-and-error approach; cycling through crystal systems to find a unit cell, before proposing different space groups to account for as many reflections as possible. From this, one can extract a model structure that can then be used as the basis for Rietveld refinement. The user can point the software towards likely space groups through constraints, and thus speed up this process, or indeed test how well a specific space group describes the pattern. All of the samples discussed in subsequent chapters were of sufficient quality that this potentially troublesome procedure was actually very quick; the software promptly identified the symmetry of the cell from minimal user instruction.

Appendix B

Technical information regarding μSR

In this Appendix, I present some of the key properties of the muon that make it such a useful probe, as well as an explanation of how one can produce a spin-polarised beam of muons. Also presented are some of the technical differences between the two kinds of muon source (continuous beam and pulsed beam) used throughout this project and, finally, what stopping processes muons undergo when they enter a sample.

B.1 The muon

The fundamental properties of muons, compared with other subatomic particles, are shown in Table B.1. Although they can carry both positive and negative charge, the subsequent discussion is restricted to positive muons. Negatively charged muons, when implanted into a sample, will be attracted and most probably bound to the positively charged atomic nuclei in a $1s$ orbital with a small Bohr radius ($\simeq a_0/(Zm_\mu/m_\mathrm{e})$ where Z is the atomic number of the nucleus, $m_\mu/m_\mathrm{e} \simeq 207$ and a_0 is the Bohr radius or hydrogen). Their subsequent precession will therefore be dominated by a contact hyperfine interaction with the nucleus. Positive muons on the other hand are drawn to areas of negative electric charge – in and around atomic electron clouds – and it is in these regions of the unit cell that the effects of any emergent magnetism in the system will be most keenly felt.

	q (e)	S	Mass (m_e)	Moment (μ_B)	$\gamma/2\pi$ (MHz T^{-1})	Lifetime (s)
e	-1	$\frac{1}{2}$	1	-1.0011	2802×10^{-3}	∞
μ^+	$+1$	$\frac{1}{2}$	207	4.88×10^{-3}	135.5	2.19×10^{-6}
n	0	$\frac{1}{2}$	1840	-1.713×10^{-3}	183.3	885

TABLE B.1: Properties of the muon, electron and neutron. γ is the gyromagnetic ratio, which governs the precession frequency of a particle's spin in a magnetic field.

B.2 A beam of spin-polarised muons

As previously mentioned, the experimental aim is to track the precession of the muon spin within the sample. One therefore needs to know the polarisation of the muon as it enters the sample, the polarisation on decay and the time elapsed between these two events. It is shown in the next subsection that the instantaneous spin of the muon on decay is revealed by a consequence of weak decay. This section discusses how, thanks to a careful method of muon production and transport, a beam of muons with all their spins coaligned can be readily achieved, and thus the muon polarisation on entry is known too.

Muons are produced during the decay of pions, themselves a product of collisions between protons and nucleons. Typically, a proton beam (the production of which is discussed in a later subsection) impinges on a heavy metal target (e.g. W), and produces pions via

$$\begin{aligned} \mathrm{p} + \mathrm{p} &\longrightarrow \mathrm{p} + \mathrm{n} + \pi^+, \\ \mathrm{p} + \mathrm{n} &\longrightarrow \mathrm{n} + \mathrm{n} + \pi^+. \end{aligned}$$

These pions then decay into muons via

$$\pi^+ \longrightarrow \mu^+ + \nu_\mu.$$

The neutrino in this decay has negative helicity, meaning that its spin is antiparallel to its momentum. As this is two-body decay, the conservation of linear and angular momentum forces the muon to have negative helicity in the pion rest frame, so its spin must also be antiparallel to its momentum. A series of dipolar and quadrupolar magnets steer and focus the muon beam, maintaining its polarisation as the spins of different muons are all affected identically. To remove any unwanted particles, such as positrons from early muon decay (see later subsection), a *separator* is created from electric and magnetic fields at right angles. In this setup, particles with a velocity $v \neq E/B$ will experience a Lorentz force and be diverted, so calibrating the fields such that $E/B = v_\mu$ will ensure that only muons pass to the sample.

B.2.1 Aside: decay muons

Most of the pions which decay into muons do so almost instantaneously after their own production from proton collisions. Thus, these pions are essentially at rest on the surface of the heavy metal target and the muons emerging from them are sometimes called “surface muons”. This is as opposed to so-called “decay muons” which come from pions that have escaped the target and decay in-flight. Decay muons have a higher energy than surface muons, as they come from moving pions, but are not quite so well polarised. Because of their higher energy, they tend to pass straight through typically-sized samples, and so they (with their reduced polarisation) do not contribute to the asymmetry spectrum.

Sometimes, however, decay muons are required. If the sample is large, for instance if it is contained in a heavy pressure cell (see Chapter 7), surface muons will not have the required energy to penetrate the bulk of the sample and so decay muons are used instead.

B.3 Continuous and pulsed sources

When muons arrive at the sample they must be counted in. This is done differently depending on the nature of the muon beam and there are two cases to consider: continuous and pulsed muon beams. The work in this project made use of both the continuous beam at the Paul Scherrer Institute (PSI)[1] and the pulsed muon beam at the ISIS Facility[2].

At ISIS, protons are generated by stripping electrons from H$^-$ ions. These ions are extracted from a plasma in 200 μs pulses which means the generation of subsequent muons also occurs in such pulses. The extraction of H$^-$ ions is timed and, when corrected for the creation and transport of muons, this provides the counting in time at ISIS.

At PSI, the protons are similarly produced but accelerated by a cyclotron (as opposed to the synchrotron at ISIS) in lots of small and closely spaced bunches, so the resulting muon beam is effectively continuous. Following muon production, a series of choppers

---

[1] Villigen, Switzerland.

[2] Rutherford Appleton Laboratory, Chilton, Oxfordshire, UK.

restrict muons to pass through a counter and into the sample one at a time. The counter is a thin sheet of mylar that scintillates as a muon passes through it; this electrodynamic process can be recorded and timed and does not affect the muon spin. If more than one muon is counted on decay (perhaps a very long-lived muon remains in the sample as the next one arrives) then those events are discarded from the final signal, as one could not be sure of the corresponding entry times.

This rejection of data from long-lived muons causes a problem for continuous sources from which pulsed sources do not suffer. Although the average muon lifetime is $2.2\,\mu$s (see Table B.1) there will be some muons decaying more than $10\,\mu$s after production. Such muons can respond to a variety of microscopic phenomena, such as slow dynamic processes, that short-lived muons simply cannot and so such effects can only be seen at pulsed sources. However, the downside of a pulsed source is a comparatively poor time resolution. The pulse of muons arriving at the sample has a temporal width ($\simeq 70\,rmns$ – not every muon arrives at precisely the same time – yet they are counted in as one. Good data will not be available until the entire pulse has arrived but many muons will be already precessing by then. If such physical processes exist to cause sufficiently rapid precession that some muons have significantly dephased before the entire pulse has arrived, the effects of these processes will be lost. Fast dynamic effects and strong-moment magnetism, for instance, are therefore best observed at continuous sources.

Incidentally, a key advantage of μSR in general is highlighted by the value of the muon lifetime, shown in Table B.1: $\tau_\mu = 2.19\,\mu s$. On the time-scale of typical fluctuations within condensed matter systems, this lifetime is such as to allow muons to probe physical processes that are outside the temporal resolution of other techniques. Figure B.1 shows that μSR bridges an important gap between fluctuations that can be seen by neutron scattering (fast) and those that can be probed using nuclear magnetic resonance (NMR – slow).

B.4 Muon decay

Positive muons decay into positrons and neutrinos, conserving lepton number in the usual way:

$$\mu^+ \longrightarrow e^+ + \nu_e + \bar{\nu}_\mu .$$

Positrons are easily detected using a scintillator and a photomultiplier tube, so the decay time is easily measured. Information about the spin then comes from the violation

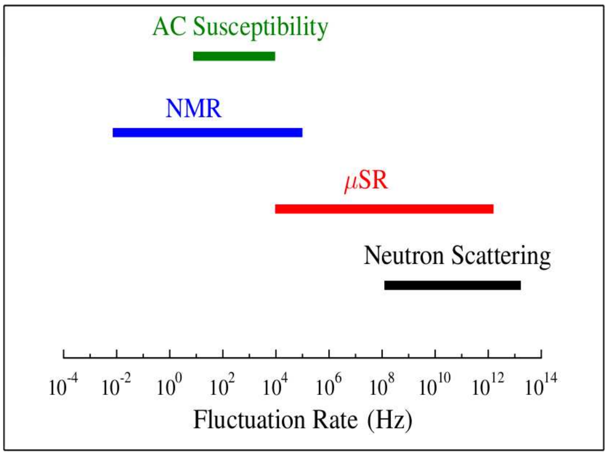

Figure B.1: The range of fluctuation rates that can be measured with different techniques.

of the conservation of parity during this weak decay process. Positrons are emitted preferentially along the direction in which the muon spin was pointing at the instant of decay and when averaged over all available positron energies the angular distribution of positron trajectories is as shown in Figure 3.3.

B.5 Muon stopping processes

On entering the sample, the muon will come to rest before precessing. Figure B.2 summarises the processes undergone by a muon on entering a sample and what is vital here is that none of these processes affect the muon spin.

In the kinds of experiments carried out during this project, muons come to rest once they have passed through around 100 mg cm^{-2} of sample, thus at least twice this area density is usually needed in order to probe the bulk. Any appreciable damage to the sample will occur at the surface and, due to the energies involved, muons will typically come to rest at least 1 μm away from this damaged region.

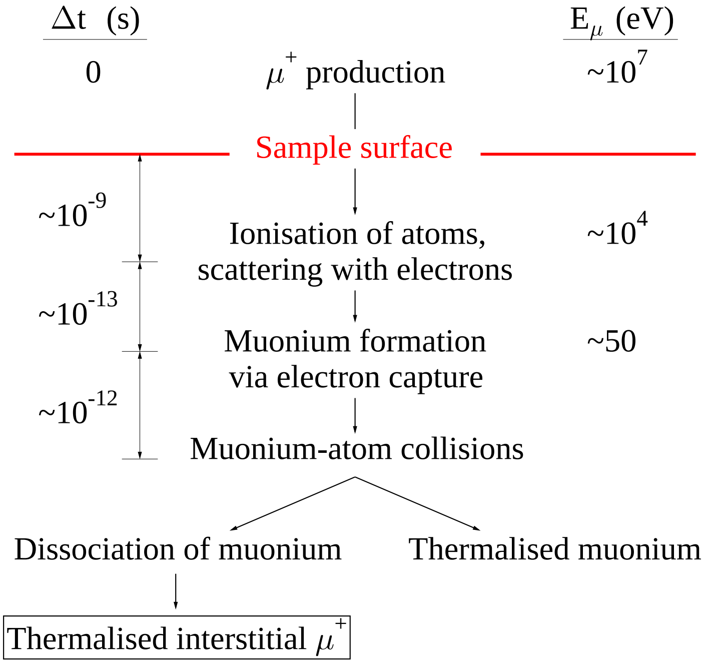

FIGURE B.2: Processes undergone by muons on entering a sample. Shown also are the timescales of each process and the kinetic energy of the muon following them. Crucially, none of these processes affect the muon spin.

Appendix C

The two-gap α-model

In this Appendix, I present the mathematical background of the two-gap α-model that was used to fit the $B_{\mathrm{rms}}(T)$ data for the Li-intercalate in Chapter 6.

The starting point is the Chandrasekhar [96] result, also referenced extensively in Chapter 5, which gives the penetration depth (in SI units) as:

$$\frac{1}{\lambda^2(T)} = \frac{\mu_0 e^2}{4\pi^3\hbar} \oint \mathrm{d}S_{\mathrm{F}} \frac{\vec{v_{\mathrm{F}}} \cdot \vec{v_{\mathrm{F}}}}{v_{\mathrm{F}}} \times \left(1 + 2\int_{\Delta_k(T)}^{\infty} \mathrm{d}E \frac{\partial f(E,T)}{\partial E} \frac{E}{\sqrt{E^2 - \Delta_k(T)^2}}\right), \tag{C.1}$$

where $f(E,T)$ is the Fermi-Dirac distribution function, Δ_k is the (generally momentum-dependent) superconducting gap and $\vec{v_{\mathrm{F}}}$ and $\mathrm{d}S_{\mathrm{F}}$ are the Fermi velocity and a Fermi surface element respectively. Note that the temperature-dependence only enters the expression on the second term, which quantifies the effects of Bogoliubov quasiparticles being thermally excited across the energy gap (which is also absent from the first term). As $\partial f(E,T)/\partial E$ is negative at finite temperature, the second term reduces $\lambda(T)^{-2}$ from its zero-temperature value. If the Fermi surface has more than one section, one can calculate the contributions from each section by applying Equation C.1 to them individually, and then summing the contributions.

If one has either measured the electronic and gap structures, perhaps using ARPES, or has calculated them from some numerical procedure, Equation C.1 can then be used to predict what the corresponding penetration depth will be. I, however, am interested in the opposite: I can measure $\lambda(T)^{-2}$ directly using TF-μSR and I want to fit this data to Equation C.1 to find out something about these structures. Achieving this can be tricky, not least because the second integral in Equation C.1 is impossible to carry out analytically. To proceed, I need to make some simplifications.

The first is to assume that I am dealing exclusively with systems containing two isotropic gaps, in accordance with the $s^{\pm}$ gap structure proposed for the majority of pnictides. I then take the temperature-dependence of these gaps to be approximated by

$$\Delta_{1,2}(T) = \Delta_{1,2}(0)\tanh\left\{1.82\left[1.018\left(\frac{T_{\mathrm{c}}}{T}-1\right)\right]^{0.51}\right\}, \tag{C.2}$$

following Refs. [19, 21, 170]. I can re-write Equation C.1 as

$$\frac{1}{\lambda_{1,2}^{2}(T)} = \frac{1}{\lambda_{1,2}^{2}(0)}[1 - I_{1,2}(T)], \tag{C.3}$$

with

$$I_{1,2} = -2\int_{\Delta_{1,2}(T)}^{\infty} \mathrm{d}E \frac{\partial f(E,T)}{\partial E}\frac{E}{\sqrt{E^2 - \Delta_{1,2}(T)^2}} \tag{C.4}$$

and

$$\frac{1}{\lambda_{1,2}(0)^2} = \frac{\mu_0 e^2}{4\pi^3\hbar}\left(\oint \mathrm{d}S_{\mathrm{F}}\frac{\vec{v_{\mathrm{F}}}\cdot\vec{v_{\mathrm{F}}}}{v_{\mathrm{F}}}\right)_{1,2}. \tag{C.5}$$

Following Reference [196], I can further approximate the integrals (C.4) as

$$I_{1,2} = \mathrm{sech}^2\left(\frac{\Delta_{1,2}}{k_{\mathrm{B}}T}\right)\sqrt{\frac{\pi\Delta_{1,2}}{8k_{\mathrm{B}}T} + \left(1+\frac{\pi\Delta_{1,2}}{8k_{\mathrm{B}}T}\right)^{-1}} \tag{C.6}$$

The absolute value of the penetration depth will be given by $\lambda(0)^{-2} = \lambda_1(0)^{-2} + \lambda_2(0)^{-2}$, so defining $\omega = \lambda_1(0)^{-2}/\lambda(0)^{-2}$ allows me to write the temperature-dependence of $\lambda(T)$ as

$$\frac{1}{\lambda(T)^2} = \frac{1}{\lambda(0)^2}\{\omega[1 - I_1(T)] + (1-\omega)[1 - I_2(T)]\}, \tag{C.7}$$

where Equations C.6 and C.2 are used to compute the values of $I_{1,2}$.

Using the fact that $B_{\mathrm{rms}}(T) \propto \lambda^{-2}$ (see Equation 3.10), and contributions to $B_{\mathrm{rms}}(T)$ add in quadrature, I can then provide the function I used to fit my TF-μSR results for the Li-intercalate:

$$B_{\mathrm{rms}}(T) = \sqrt{B_{\mathrm{rms}}(0)^2\{\omega[1 - I_1(T)] + (1-\omega)[1 - I_2(T)]\}^2 + BG^2} \tag{C.8}$$

The fitting parameters are then $B_{\mathrm{rms}}(0)$, the zero-temperature gap values, $\Delta_{1,2}(0)$, the relative contribution of these gaps, ω, the transition temperature, T_{c}, and a constant background contribution to $B_{\mathrm{rms}}(T)$, BG. From the former, I can then calculate $\lambda(0)$ using Equation 3.10. To be clear, $B_{\mathrm{rms}}(0)$ is governed by details of the Fermi surface according to Equation C.5; I have no access to this information, so $B_{\mathrm{rms}}(0)$ is a free parameter. Rather, it is the *form* of $B_{\mathrm{rms}}(T)$ that is governed by the magnitudes and relative contributions of the gaps.

Bibliography

[1] Fong-Chi Hsu, Jiu-Yong Luo, Kuo-Wei Yeh, Ta-Kun Chen, Tzu-Wen Huang, Phillip M. Wu, Yong-Chi Lee, Yi-Lin Huang, Yan-Yi Chu, Der-Chung Yan, and Maw-Kuen Wu. Superconductivity in the PbO-type structure α-FeSe. *Proceedings of the National Academy of Sciences*, 105(38):14262–14264, 2008. doi: 10.1073/pnas.0807325105.

[2] Kenji Ishida, Yusuke Nakai, and Hideo Hosono. To what extent iron-pnictide new superconductors have been clarified: A progress report. *Journal of the Physical Society of Japan*, 78(6):062001, 2009. doi: 10.1143/JPSJ.78.062001.

[3] Chul-Ho Lee, Akira Iyo, Hiroshi Eisaki, Hijiri Kito, Maria Teresa Fernandez-Diaz, Toshimitsu Ito, Kunihiro Kihou, Hirofumi Matsuhata, Markus Braden, and Kazuyoshi Yamada. Effect of structural parameters on superconductivity in fluorine-free $\mathrm{LnFeAsO}_{1-y}$ $(\mathrm{Ln} = \mathrm{La}, \mathrm{Nd})$. *Journal of the Physical Society of Japan*, 77(8):083704, 2008. doi: 10.1143/JPSJ.77.083704.

[4] A. I. Goldman, D. N. Argyriou, B. Ouladdiaf, T. Chatterji, A. Kreyssig, S. Nandi, N. Ni, S. L. Bud'ko, P. C. Canfield, and R. J. McQueeney. Lattice and magnetic instabilities in $\mathrm{CaFe_2As_2}$: A single-crystal neutron diffraction study. *Phys. Rev. B*, 78:100506, Sep 2008. doi: 10.1103/PhysRevB.78.100506.

[5] S. Nandi, M. G. Kim, A. Kreyssig, R. M. Fernandes, D. K. Pratt, A. Thaler, N. Ni, S. L. Bud'ko, P. C. Canfield, J. Schmalian, R. J. McQueeney, and A. I. Goldman. Anomalous suppression of the orthorhombic lattice distortion in superconducting $\mathrm{Ba(Fe_{1-x}Co_x)_2As_2}$ single crystals. *Phys. Rev. Lett.*, 104(5):057006, Feb 2010. doi: 10.1103/PhysRevLett.104.057006.

[6] S. Avci, O. Chmaissem, D. Y. Chung, S. Rosenkranz, E. A. Goremychkin, J. P. Castellan, I. S. Todorov, J. A. Schlueter, H. Claus, A. Daoud-Aladine, D. D. Khalyavin, M. G. Kanatzidis, and R. Osborn. Phase diagram of $\mathrm{Ba_{1-x}K_xFe_2As_2}$. *Phys. Rev. B*, 85:184507, May 2012. doi: 10.1103/PhysRevB.85.184507.

[7] H. Luetkens, H.-H. Klauss, M. Kraken, F. J. Litterst, T. Dellmann, R. Klingeler, C. Hess, R. Khasanov, A. Amato, C. Baines, M. Kosmala, O. J. Schumann, M. Braden, J. Hamann-Borrero, N. Leps, A. Kondrat, G. Behr, J. Werner, and B. Buchner. The electronic phase diagram of the $\mathrm{LaO_{1-x}F_xFeAs}$ superconductor. *Nature Materials*, 8(4):305–309, 2009.

[8] J. Zhao, Q. Huang, S. de la Cruz, C.and Li, J. W. Lynn, Y. Chen, M. A. Green, G. F. Chen, G. Li, Z. Li, J. L. Luo, N. L. Wang, and P. Dai. Structural and magnetic phase diagram of $\mathrm{CeFeAsO_{1-x}F_x}$ and its relation to high-temperature superconductivity. *Nature Materials*, 7:953–959, 2008.

[9] J. Dong, H. J. Zhang, G. Xu, Z. Li, G. Li, W. Z. Hu, D. Wu, G. F. Chen, X. Dai, J. L. Luo, Z. Fang, and N. L. Wang. Competing orders and spin-density-wave instability in $\mathrm{La(O_{1-x}F_x)FeAs}$. *EPL (Europhysics Letters)*, 83(2):27006, 2008.

[10] Paul Scherrer Institut. URL `http://www.psi.ch/media/doing-research-with-muons`.

[11] S.S.L. Lee, S.H. Kilcoyne, and R. Cywinski. *Muon Science: Muons in Physics, Chemistry, and Materials : Proceedings of the Fifty First Scottish Universities Summer School in Physics, St. Andrews, August 1998*. NATO advanced study institutes series: Physics. Scottish Universities Summer School in Physics & Institute of Physics Publishing, 1999. ISBN 9780750306300.

[12] Dinah R. Parker, Matthew J. P. Smith, Tom Lancaster, Andrew J. Steele, Isabel Franke, Peter J. Baker, Francis L. Pratt, Michael J. Pitcher, Stephen J. Blundell, and Simon J. Clarke. Control of the competition between a magnetic phase and a superconducting phase in cobalt-doped and nickel-doped NaFeAs using electron count. *Phys. Rev. Lett.*, 104(5):057007, Feb 2010. doi: 10.1103/PhysRevLett.104.057007.

[13] D. R. Parker, M. J. Pitcher, P. J. Baker, I. Franke, T. Lancaster, S. J. Blundell, and S. J. Clarke. Structure, antiferromagnetism and superconductivity of the layered iron arsenide NaFeAs. *Chemical Communications*, 16:2189–2193, 2009.

[14] Michael J. Pitcher, Tom Lancaster, Jack D. Wright, Isabel Franke, Andrew J. Steele, Peter J. Baker, Francis L. Pratt, William Trevelyan Thomas, Dinah R. Parker, Stephen J. Blundell, and Simon J. Clarke. Compositional control of the superconducting properties of LiFeAs. *J. Am. Chem. Soc*, 132(30):10467–10476, Jul 2010. doi: 10.1021/ja103196c.

[15] F. L. Pratt, P. J. Baker, S. J. Blundell, T. Lancaster, H. J. Lewtas, P. Adamson, M. J. Pitcher, D. R. Parker, and S. J. Clarke. Enhanced superfluid stiffness,

lowered superconducting transition temperature, and field-induced magnetic state of the pnictide superconductor LiFeAs. *Phys. Rev. B*, 79(5):052508, Feb 2009. doi: 10.1103/PhysRevB.79.052508.

[16] T. J. Williams, A. A. Aczel, E. Baggio-Saitovitch, S. L. Bud'ko, P. C. Canfield, J. P. Carlo, T. Goko, H. Kageyama, A. Kitada, J. Munevar, N. Ni, S. R. Saha, K. Kirschenbaum, J. Paglione, D. R. Sanchez-Candela, Y. J. Uemura, and G. M. Luke. Superfluid density and field-induced magnetism in $\mathrm{Ba(Fe_{1-x}Co_x)_2As_2}$ and $\mathrm{Sr(Fe_{1-x}Co_x)_2As_2}$ measured with muon spin relaxation. *Phys. Rev. B*, 82:094512, Sep 2010. doi: 10.1103/PhysRevB.82.094512.

[17] J. P. Carlo, Y. J. Uemura, T. Goko, G. J. MacDougall, J. A. Rodriguez, W. Yu, G. M. Luke, Pengcheng Dai, N. Shannon, S. Miyasaka, S. Suzuki, S. Tajima, G. F. Chen, W. Z. Hu, J. L. Luo, and N. L. Wang. Static magnetic order and superfluid density of RFeAs(O,F) (R=La,Nd,Ce) and LaFePO studied by muon spin relaxation: Unusual similarities with the behavior of cuprate superconductors. *Phys. Rev. Lett.*, 102(8):087001, Feb 2009. doi: 10.1103/PhysRevLett.102.087001.

[18] H. Luetkens, H.-H. Klauss, R. Khasanov, A. Amato, R. Klingeler, I. Hellmann, N. Leps, A. Kondrat, C. Hess, A. Kohler, G. Behr, J. Werner, and B. Buchner. Field and temperature dependence of the superfluid density in $\mathrm{LaFeAsO_{1-x}F_x}$ superconductors: A muon spin relaxation study. *Phys. Rev. Lett.*, 101(9):097009, Aug 2008. doi: 10.1103/PhysRevLett.101.097009.

[19] R. Khasanov, K. Conder, E. Pomjakushina, A. Amato, C. Baines, Z. Bukowski, J. Karpinski, S. Katrych, H.-H. Klauss, H. Luetkens, A. Shengelaya, and N. D. Zhigadlo. Evidence of nodeless superconductivity in $\mathrm{FeSe_{0.85}}$ from a muon-spin-rotation study of the in-plane magnetic penetration depth. *Phys. Rev. B*, 78: 220510, Dec 2008. doi: 10.1103/PhysRevB.78.220510.

[20] K. Hashimoto, K. Cho, T. Shibauchi, S. Kasahara, Y. Mizukami, R. Katsumata, Y. Tsuruhara, T. Terashima, H. Ikeda, M. A. Tanatar, H. Kitano, N. Salovich, R. W. Giannetta, P. Walmsley, A. Carrington, R. Prozorov, and Y. Matsuda. A sharp peak of the zero-temperature penetration depth at optimal composition in $\mathrm{BaFe_2(As_{1-x}P_x)_2}$. *Science*, 336(6088):1554–1557, 2012. doi: 10.1126/science.1219821.

[21] R. Khasanov, D. V. Evtushinsky, A. Amato, H.-H. Klauss, H. Luetkens, Ch. Niedermayer, B. Büchner, G. L. Sun, C. T. Lin, J. T. Park, D. S. Inosov, and V. Hinkov. Two-gap superconductivity in $\mathrm{Ba_{1-x}K_xFe_2As_2}$: A complementary study of the magnetic penetration depth by muon-spin rotation and

angle-resolved photoemission. *Phys. Rev. Lett.*, 102:187005, May 2009. doi: 10.1103/PhysRevLett.102.187005.

[22] H. Kawano-Furukawa, C. J. Bowell, J. S. White, R. W. Heslop, A. S. Cameron, E. M. Forgan, K. Kihou, C. H. Lee, A. Iyo, H. Eisaki, T. Saito, H. Fukazawa, Y. Kohori, R. Cubitt, C. D. Dewhurst, J. L. Gavilano, and M. Zolliker. Gap in KFe_2As_2 studied by small-angle neutron scattering observations of the magnetic vortex lattice. *Phys. Rev. B*, 84:024507, Jul 2011. doi: 10.1103/PhysRevB.84.024507.

[23] Y.J. Uemura. Twin spin/charge roton mode and superfluid density: Primary determining factors of T_c in high-T_c superconductors observed by neutron, ARPES, and μSR. *Physica B: Condensed Matter*, 374–375"(0):1–8, 2006. ISSN 0921–4526. doi: http://dx.doi.org/10.1016/j.physb.2005.11.004. Proceedings of the Tenth International Conference on Muon Spin Rotation, Relaxation and Resonance.

[24] C. C. Homes, B. P. Clayman, J. L. Peng, and R. L. Greene. Optical properties of $Nd_{1.85}Ce_{0.15}CuO_4$. *Phys. Rev. B*, 56(9):5525–5543, Sep 1997. doi: 10.1103/PhysRevB.56.5525.

[25] A. Shengelaya, R. Khasanov, D. G. Eshchenko, D. Di Castro, I. M. Savić, M. S. Park, K. H. Kim, Sung-Ik Lee, K. A. Müller, and H. Keller. Muon-spin-rotation measurements of the penetration depth of the infinite-layer electron-doped $Sr_{0.9}La_{0.1}CuO_2$ cuprate superconductor. *Phys. Rev. Lett.*, 94(12):127001–127005, Mar 2005. doi: 10.1103/PhysRevLett.94.127001.

[26] P. J. Hirschfeld, M. M. Korshunov, and I. I. Mazin. Gap symmetry and structure of Fe-based superconductors. *Reports on Progress in Physics*, 74(12):124508, 2011.

[27] L.Craco and S.Leoni. Comparative study of tetragonal and hexagonal FeSe: An orbital-selective scenario. *EPL (Europhysics Letters)*, 92(6):67003, 2010.

[28] S. Margadonna, Y. Takabayashi, Y. Ohishi, Y. Mizuguchi, Y. Takano, T. Kagayama, T. Nakagawa, M. Takata, and K. Prassides. Pressure evolution of the low-temperature crystal structure and bonding of the superconductor FeSe ($T_c =$ 37 K). *Phys. Rev. B*, 80:064506, Aug 2009. doi: 10.1103/PhysRevB.80.064506.

[29] A. Gurevich. Enhancement of the upper critical field by nonmagnetic impurities in dirty two-gap superconductors. *Phys. Rev. B*, 67:184515, May 2003. doi: 10.1103/PhysRevB.67.184515.

[30] M. J. Pitcher. PhD Thesis: The structures and properties of layered pnictides and oxychalcogenides, 2011.

[31] P. K. Biswas, A. Krzton-Maziopa, R. Khasanov, H. Luetkens, E. Pomjakushina, K. Conder, and A. Amato. Two-dimensional superfluid density in an alkali metal-organic solvent intercalated iron selenide superconductor $Li(C_5H_5N)_{0.2}Fe_2Se_2$. *Phys. Rev. Lett.*, 110:137003, Mar 2013. doi: 10.1103/PhysRevLett.110.137003.

[32] Z. Shermadini, H. Luetkens, R. Khasanov, A. Krzton-Maziopa, K. Conder, E. Pomjakushina, H-H. Klauss, and A. Amato. Superconducting properties of single-crystalline $A_xFe_{2-y}Se_2$ (A =Rb, K) studied using muon spin spectroscopy. *Phys. Rev. B*, 85:100501, Mar 2012. doi: 10.1103/PhysRevB.85.100501.

[33] F. London and H. London. The electromagnetic equations of the supraconductor. *Proc. Roy. Soc. (London)*, A149:71, 1935.

[34] W. Meissner and R. Ochsenfeld. Ein neuer effekt bei eintritt der supraleitfähigkeit. *Naturwissenschaften*, 21:787–788, 1933.

[35] J. Bardeen, L. N. Cooper, and J. R. Schrieffer. Theory of Superconductivity. *Phys. Rev.*, 108:1175–1204, Dec 1957. doi: 10.1103/PhysRev.108.1175.

[36] J. G. Bednorz and K. A. Müller. Zeitschrift für physik b condensed matter. *Naturwissenschaften*, 64:189–193, 1986.

[37] A. Shilling, M. Cantoni, J. D. Guo, and H. R. Ott. Superconductivity above 130K in the Hg-Ba-Ca-Cu-O system. *Nature*, 363:56–58, 1993.

[38] N. P. Armitage, P. Fournier, and R. L. Greene. Progress and perspectives on electron-doped cuprates. *Rev. Mod. Phys.*, 82:2421–2487, Sep 2010. doi: 10.1103/RevModPhys.82.2421.

[39] F. Steglich, J. Aarts, C. D. Bredl, W. Lieke, D. Meschede, W. Franz, and H. Schäfer. Superconductivity in the presence of strong pauli paramagnetism: $CeCu_2Si_2$. *Phys. Rev. Lett.*, 43:1892–1896, Dec 1979. doi: 10.1103/PhysRevLett.43.1892.

[40] P. Monthoux, D. Pines, and G. G. Lonzarich. Superconductivity without phonons. *Nature*, 450:1177–1183, Dec 2007.

[41] G. R. Stewart. Superconductivity in iron compounds. *Rev. Mod. Phys.*, 83:1589–1652, Dec 2011. doi: 10.1103/RevModPhys.83.1589.

[42] David C. Johnston. The puzzle of high temperature superconductivity in layered iron pnictides and chalcogenides. *Advances in Physics*, 59(6):803–1061, 2010. doi: 10.1080/00018732.2010.513480.

[43] M. J. Pitcher, D. R. Parker, P. Adamson, S. J. C Herkelrath, A. T. Boothroyd, R. M. Ibberson, M. Brunelli, and S. J. Clarke. Structure and superconductivity of LiFeAs. *Chemical Communications*, pages 5918–20, 2008. doi: 10.1039/b813153h.

[44] Joshua H. Tapp, Zhongjia Tang, Bing Lv, Kalyan Sasmal, Bernd Lorenz, Paul C. W. Chu, and Arnold M. Guloy. LiFeAs: An intrinsic FeAs-based superconductor with $T_c = 18$ K. *Phys. Rev. B*, 78:060505, Aug 2008. doi: 10.1103/PhysRevB.78.060505.

[45] Yoichi Kamihara, Takumi Watanabe, Masahiro Hirano, and Hideo Hosono. Iron-based layered superconductor La($O_{1-x}F_x$)FeAs (x = 0.050.12) with $T_c = 26$ K. *Journal of the American Chemical Society*, 130(11):3296–3297, 2008. doi: 10.1021/ja800073m.

[46] Marianne Rotter, Marcus Tegel, Dirk Johrendt, Inga Schellenberg, Wilfried Hermes, and Rainer Pöttgen. Spin-density-wave anomaly at 140 K in the ternary iron arsenide $BaFe_2As_2$. *Phys. Rev. B*, 78:020503, Jul 2008. doi: 10.1103/PhysRevB.78.020503.

[47] T. M. McQueen, A. J. Williams, P. W. Stephens, J. Tao, Y. Zhu, V. Ksenofontov, F. Casper, C. Felser, and R. J. Cava. Tetragonal-to-orthorhombic structural phase transition at 90 K in the superconductor $Fe_{1.01}Se$. *Phys. Rev. Lett.*, 103:057002, Jul 2009. doi: 10.1103/PhysRevLett.103.057002.

[48] Q. Huang, Y. Qiu, Wei Bao, M. A. Green, J. W. Lynn, Y. C. Gasparovic, T. Wu, G. Wu, and X. H. Chen. Neutron-diffraction measurements of magnetic order and a structural transition in the parent $BaFe_2As_2$ compound of FeAs-based high-temperature superconductors. *Phys. Rev. Lett.*, 101(25):257003, Dec 2008. doi: 10.1103/PhysRevLett.101.257003.

[49] T Nomura, S W Kim, Y Kamihara, M Hirano, P V Sushko, K Kato, M Takata, A L Shluger, and H Hosono. Crystallographic phase transition and high-T_c superconductivity in LaFeAsO:F. *Superconductor Science and Technology*, 21(12): 125028, 2008.

[50] C. de la Cruz, Q. Huang, J. W. Lynn, J. Li, W. Ratcliff II, J. L. Zarestky, H. A. Mook, G. F. Chen, J. L. Luo, N. L. Wang, and P. Dai. Magnetic order close to superconductivity in the iron-based layered $LaO_{1-x}F_xFeAs$ systems. *Nature*, 453: 889–902, 2008.

[51] Jun Zhao, Q. Huang, Clarina de la Cruz, J. W. Lynn, M. D. Lumsden, Z. A. Ren, Jie Yang, Xiaolin Shen, Xiaoli Dong, Zhongxian Zhao, and Pengcheng Dai. Lattice

and magnetic structures of PrFeAsO, $PrFeAsO_{0.85}F_{0.15}$, and $PrFeAsO_{0.85}$. *Phys. Rev. B*, 78:132504, Oct 2008. doi: 10.1103/PhysRevB.78.132504.

[52] Y. Qiu, Wei Bao, Q. Huang, T. Yildirim, J. M. Simmons, M. A. Green, J. W. Lynn, Y. C. Gasparovic, J. Li, T. Wu, G. Wu, and X. H. Chen. Crystal structure and antiferromagnetic order in $NdFeAsO_{1-x}F_x$ ($x = 0.0$ and 0.2) superconducting compounds from neutron diffraction measurements. *Phys. Rev. Lett.*, 101:257002, Dec 2008. doi: 10.1103/PhysRevLett.101.257002.

[53] Jun Zhao, W. Ratcliff II, J. W. Lynn, G. F. Chen, J. L. Luo, N. L. Wang, Jiangping Hu, and Pengcheng Dai. Spin and lattice structures of single-crystalline $SrFe_2As_2$. *Phys. Rev. B*, 78:140504, Oct 2008. doi: 10.1103/PhysRevB.78.140504.

[54] S. A. J. Kimber, A. Kreyssig, Y.-Z. Zhang, H. O. Jeschke, R. Valenti, F. Yokaichiya, E. Colombier, J. Yan, T. C. Hansen, T. Chatterji, R. J. McQueeney, P. C. Canfield, A. I. Goldman, and D. N. Argyriou. Similarities between structural distortions under pressure and chemical doping in superconducting $BaFe_2As_2$. *Nature Materials*, 8:471–475, 2009.

[55] S. Medvedev, T. M. McQueen, I. A. Troyan, T. Palasyuk, M. I. Eremets, R. J. Cava, S. Naghavi, F. Casper, V. Ksenofontov, G. Wortmann, and C. Felser. Electronic and magnetic phase diagram of β-$Fe_{1.01}Se$ with superconductivity at 36.7 K under pressure. *Nature Materials*, 8:630–633, 2009.

[56] Shilpam Sharma, A. Bharathi, Sharat Chandra, V. Raghavendra Reddy, S. Paulraj, A. T. Satya, V. S. Sastry, Ajay Gupta, and C. S. Sundar. Superconductivity in ru-substituted polycrystalline $BaFe_{2-x}Ru_xAs_2$. *Phys. Rev. B*, 81: 174512, May 2010. doi: 10.1103/PhysRevB.81.174512.

[57] S. Kasahara, T. Shibauchi, K. Hashimoto, K. Ikada, S. Tonegawa, R. Okazaki, H. Shishido, H. Ikeda, H. Takeya, K. Hirata, T. Terashima, and Y. Matsuda. Evolution from non-fermi- to fermi-liquid transport via isovalent doping in $BaFe_2(As_{1-x}P_x)_2$ superconductors. *Phys. Rev. B*, 81:184519, May 2010. doi: 10.1103/PhysRevB.81.184519.

[58] Chandra Varma. High-temperature superconductivity: Mind the pseudogap. *Nature*, 468:184–185, 2010.

[59] Yoshikazu Mizuguchi and Yoshihiko Takano. Review of Fe chalcogenides as the simplest Fe-based superconductor. *Journal of the Physical Society of Japan*, 79 (10):102001, 2010. doi: 10.1143/JPSJ.79.102001.

[60] I. I. Mazin, D. J. Singh, M. D. Johannes, and M. H. Du. Unconventional superconductivity with a sign reversal in the order parameter of $\mathrm{LaFeAsO}_{1-x}\mathrm{F}_x$. *Phys. Rev. Lett.*, 101(5):057003, Jul 2008. doi: 10.1103/PhysRevLett.101.057003.

[61] G. Grüner. *Density Waves In Solids*. Advanced book program: Addison-Wesley. Perseus Publishing, 2000. ISBN 9780738203041.

[62] S. Lebègue. Electronic structure and properties of the fermi surface of the superconductor LaOFeP. *Phys. Rev. B*, 75:035110, Jan 2007. doi: 10.1103/PhysRevB.75.035110.

[63] D. J. Singh. Electronic structure and doping in $\mathrm{BaFe}_2\mathrm{As}_2$ and LiFeAs: Density functional calculations. *Phys. Rev. B*, 78:094511, Sep 2008. doi: 10.1103/PhysRevB.78.094511.

[64] H. Ding, P. Richard, K. Nakayama, K. Sugawara, T. Arakane, Y. Sekiba, A. Takayama, S. Souma, T. Sato, T. Takahashi, Z. Wang, X. Dai, Z. Fang, G. F. Chen, J. L. Luo, and N. L. Wang. Observation of fermi-surfacedependent nodeless superconducting gaps in $\mathrm{Ba}_{0.6}\mathrm{K}_{0.4}\mathrm{Fe}_2\mathrm{As}_2$. *EPL (Europhysics Letters)*, 83(4): 47001, 2008.

[65] Chang Liu, G. D. Samolyuk, Y. Lee, Ni Ni, Takeshi Kondo, A. F. Santander-Syro, S. L. Bud'ko, J. L. McChesney, E. Rotenberg, T. Valla, A. V. Fedorov, P. C. Canfield, B. N. Harmon, and A. Kaminski. K-doping dependence of the fermi surface of the iron-arsenic $\mathrm{Ba}_{1-x}\mathrm{K}_x\mathrm{Fe}_2\mathrm{As}_2$ superconductor using angle-resolved photoemission spectroscopy. *Phys. Rev. Lett.*, 101:177005, Oct 2008. doi: 10.1103/PhysRevLett.101.177005.

[66] A. Furrer, J. Mesot, and T. Strässle. *Neutron scattering in condensed matter physics*. Series on neutron techniques and applications. World Scientific, 2009. ISBN 9789810248307.

[67] A. D. Christianson, E. A. Goremychkin, R. Osborn, S. Rosenkranz, M. D. Lumsden, C. D. Malliakas, I. S. Todorov, H. Claus, D. Y. Chung, M. G. Kanatzidis, R. I. Bewley, and T. Guidi. Unconventional superconductivity in $\mathrm{Ba}_{0.6}\mathrm{K}_{0.4}\mathrm{Fe}_2\mathrm{As}_2$ from inelastic neutron scattering. *Nature*, 456:930–932, 2008.

[68] K. Matano, Z. A. Ren, X. L. Dong, L. L. Sun, Z. X. Zhao, and Guo qing Zheng. Spin-singlet superconductivity with multiple gaps in $\mathrm{PrFeAsO}_{0.89}\mathrm{F}_{0.11}$. *EPL (Europhysics Letters)*, 83(5):57001, 2008.

[69] Nobuyuki Terasaki, Hidekazu Mukuda, Mitsuharu Yashima, Yoshio Kitaoka, Kiichi Miyazawa, Parasharam M. Shirage, Hijiri Kito, Hiroshi Eisaki, and Akira Iyo.

Spin fluctuations and unconventional superconductivity in the fe-based oxypnictide superconductor $LaFeAsO_{0.7}$ probed by ^{57}Fe-NMR. *Journal of the Physical Society of Japan*, 78(1):013701, 2009. doi: 10.1143/JPSJ.78.013701.

[70] Fanlong Ning, Kanagasingham Ahilan, Takashi Imai, Athena S. Sefat, Ronying Jin, Michael A. McGuire, Brian C. Sales, and David Mandrus. ^{59}Co and ^{75}As NMR investigation of electron-doped high-T_c superconductor $BaFe_{1.8}Co_{0.2}As_2$ ($T_c = 22\,K$). *Journal of the Physical Society of Japan*, 77(10):103705, 2008. doi: 10.1143/JPSJ.77.103705.

[71] J.-Ph. Reid, M. A. Tanatar, A. Juneau-Fecteau, R. T. Gordon, S. René de Cotret, N. Doiron-Leyraud, T. Saito, H. Fukazawa, Y. Kohori, K. Kihou, C. H. Lee, A. Iyo, H. Eisaki, R. Prozorov, and Louis Taillefer. Universal heat conduction in the iron arsenide superconductor KFe_2As_2: Evidence of a *d*-wave state. *Phys. Rev. Lett.*, 109:087001, Aug 2012. doi: 10.1103/PhysRevLett.109.087001.

[72] M. D. Johannes and I. I. Mazin. Microscopic origin of magnetism and magnetic interactions in ferropnictides. *Phys. Rev. B*, 79(22):220510, Jun 2009. doi: 10.1103/PhysRevB.79.220510.

[73] I.I. Mazin and J. Schmalian. Pairing symmetry and pairing state in ferropnictides: Theoretical overview. *Physica C: Superconductivity*, 469(9-12):614–627, 2009.

[74] P. Dai, J. Hu, and E. Dagotto. Magnetism and its microscopic origin in iron-based high-temperature superconductors. *Nature Physics*, 8(10):709–718.

[75] H. Wadati, I. Elfimov, and G. A. Sawatzky. Where are the extra *d* electrons in transition-metal-substituted iron pnictides? *Phys. Rev. Lett.*, 105:157004, Oct 2010. doi: 10.1103/PhysRevLett.105.157004.

[76] C. Liu, T. Kondo, R. M. Fernandes, A. D. Palczewski, E. D. Mun, N. Ni, A. N. Thaler, A. Bostwick, E. Rotenberg, J. Schmalian, S. L. Bud/'ko, P. C. Canfield, and A. Kaminski. Evidence for a Lifshitz transition in electron-doped iron arsenic superconductors at the onset of superconductivity. *Nature Physics*, 6(4):419–423.

[77] Chang Liu, A. D. Palczewski, R. S. Dhaka, Takeshi Kondo, R. M. Fernandes, E. D. Mun, H. Hodovanets, A. N. Thaler, J. Schmalian, S. L. Bud'ko, P. C. Canfield, and A. Kaminski. Importance of the fermi-surface topology to the superconducting state of the electron-doped pnictide $Ba(Fe_{1-x}Co_x)_2As_2$. *Phys. Rev. B*, 84:020509, Jul 2011. doi: 10.1103/PhysRevB.84.020509.

[78] T. Sato, K. Nakayama, Y. Sekiba, P. Richard, Y.-M. Xu, S. Souma, T. Takahashi, G. F. Chen, J. L. Luo, N. L. Wang, and H. Ding. Band structure and fermi surface

of an extremely overdoped iron-based superconductor KFe_2As_2. *Phys. Rev. Lett.*, 103:047002, Jul 2009. doi: 10.1103/PhysRevLett.103.047002.

[79] R. S. Dhaka, R. M. Liu, C.and Fernandes, R. Jiang, C. P. Strehlow, A. Kondo, T.and Thaler, J. Schmalian, S. L. Bud'ko, P. C. Canfield, and A. Kaminski. What controls the phase diagram and superconductivity in Ru-substituted $BaFe_2As_2$? *Phys. Rev. Lett.*, 107:267002, Dec 2011. doi: 10.1103/PhysRevLett.107.267002.

[80] Z. R. Ye, Y. Zhang, F. Chen, M. Xu, Q. Q. Ge, J. Jiang, B. P. Xie, and D. L. Feng. Doping dependence of the electronic structure in phosphorus-doped ferropnictide superconductor $BaFe_2(As_{1-x}P_x)_2$ studied by angle-resolved photoemission spectroscopy. *Phys. Rev. B*, 86:035136, Jul 2012. doi: 10.1103/PhysRevB.86.035136.

[81] M. Merz, P. Schweiss, P. Nagel, T. Wolf, H. v. Loehneysen, and S. Schuppler. To dope or not to dope: Electronic structure of Ba-site and Fe-site substituted single-crystalline $BaFe_2As_2$. *ArXiv e-prints*, Jun 2013.

[82] Matthew Burrard-Lucas, Stefan J. Free, David G.and Sedlmaier, Jack D. Wright, Simon J. Cassidy, Yoshiaki Hara, Alex J. Corkett, Tom Lancaster, Peter J. Baker, Stephen J. Blundell, and Simon J. Clarke. Enhancement of the superconducting transition temperature of FeSe by intercalation of a molecular spacer layer. *Nature Materials*, 12:15–19. doi: 10.1038/nmat3464.

[83] N. Ni, S. L. Bud'ko, A. Kreyssig, S. Nandi, G. E. Rustan, A. I. Goldman, S. Gupta, J. D. Corbett, A. Kracher, and P. C. Canfield. Anisotropic thermodynamic and transport properties of single-crystalline $Ba_{1-x}K_xFe_2As_2$ ($x = 0$ and 0.45). *Phys. Rev. B*, 78:014507, Jul 2008. doi: 10.1103/PhysRevB.78.014507.

[84] N.W. Ashcroft and N.D. Mermin. *Solid state physics*. Science: Physics. Holt, Rinehart and Winston, 1976. ISBN 9780030839931.

[85] A.C. Larson and R. B. Von Dreele. General structure analysis system (GSAS). *Los Alamos National Laboratory Report LAUR*, pages 86–748, 1994.

[86] B. H. Toby. EXPGUI, a graphical user interface for GSAS. *J. Appl. Cryst*, 34: 210–213, 2001.

[87] A. A Coelho. Topas academic. *Bruker AXS*, 2007.

[88] R.A. Young. *The Rietveld Method*. IUCr monographs on crystallography. Oxford University Press on Demand, 1995. ISBN 9780198559122.

[89] J. F. Annett. *Superconductivity, Superfluidity and Condensates*. Oxford University Press, 2004.

[90] S. Ghannadzadeh, M. Coak, I. Franke, P. A. Goddard, J. Singleton, and J. L. Manson. Measurement of magnetic susceptibility in pulsed magnetic fields using a proximity detector oscillator. *Review of Scientific Instruments*, 82(11):113902, 2011. doi: 10.1063/1.3653395.

[91] S. J. Blundell. Spin-polarized muons in condensed matter physics. *Contemporary Physics*, 40, 1999.

[92] F. L. Pratt. WiMDA: a muon data analysis program for the Windows PC. *Physica B*, 710:289–290, 2000. doi: 10.1016/S0921-4526(00)00328-8.

[93] Jeff E. Sonier, Jess H. Brewer, and Robert F. Kiefl. μSR studies of the vortex state in type-II superconductors. *Rev. Mod. Phys.*, 72(3):769–811, Jul 2000. doi: 10.1103/RevModPhys.72.769.

[94] V.I. Fesenko, V.N. Gorbunov, and V.P. Smilga. Analytical properties of muon polarization spectra in type-II superconductors and experimental data interpretation for mono- and polycrystalline HTSCs. *Physica C: Superconductivity*, 176(46): 551–558, 1991. ISSN 0921-4534. doi: 10.1016/0921-4534(91)90063-5.

[95] M. Tinkham. *Introduction to superconductivity*. Dover books on physics and chemistry. DOVER PUBN Incorporated, 1996. ISBN 9780486435039.

[96] B. S. Chandrasekhar and D. Einzel. The superconducting penetration depth from the semiclassical model. *Annalen der Physik*, 505(6):535–546, 1993. ISSN 1521–3889. doi: 10.1002/andp.19935050604.

[97] J. D. Wright, T. Lancaster, I. Franke, A. J. Steele, J. S. Möller, M. J. Pitcher, A. J. Corkett, D. R. Parker, D. G. Free, F. L. Pratt, P. J. Baker, S. J. Clarke, and S. J. Blundell. Gradual destruction of magnetism in the superconducting family $\mathrm{NaFe}_{1-x}\mathrm{Co}_x\mathrm{As}$. *Phys. Rev. B*, 85:054503, Feb 2012. doi: 10.1103/PhysRevB.85.054503.

[98] S. J. Blundell. *Magnetism in Condensed Matter*. Oxford University Press, 2001.

[99] H. Maeter, H. Luetkens, Yu. G. Pashkevich, A. Kwadrin, R. Khasanov, A. Amato, A. A. Gusev, K. V. Lamonova, D. A. Chervinskii, R. Klingeler, C. Hess, G. Behr, B. Büchner, and H.-H. Klauss. Interplay of rare earth and iron magnetism in RFeAsO (R =La, Ce, Pr and Sm): Muon-spin relaxation study and symmetry analysis. *Phys. Rev. B*, 80(9):094524, Sep 2009. doi: 10.1103/PhysRevB.80.094524.

[100] A. A. Aczel, E. Baggio-Saitovitch, S. L. Budko, P. C. Canfield, J. P. Carlo, G. F. Chen, Pengcheng Dai, T. Goko, W. Z. Hu, G. M. Luke, J. L. Luo, N. Ni, D. R. Sanchez-Candela, F. F. Tafti, N. L. Wang, T. J. Williams, W. Yu, and Y. J.

Uemura. Muon-spin-relaxation studies of magnetic order and superfluid density in antiferromagnetic NdFeAsO, $BaFe_2As_2$, and superconducting $Ba_{1-x}K_xFe_2As_2$. *Phys. Rev. B*, 78:214503, Dec 2008. doi: 10.1103/PhysRevB.78.214503.

[101] Y. Laplace, J. Bobroff, F. Rullier-Albenque, D. Colson, and A. Forget. Atomic coexistence of superconductivity and incommensurate magnetic order in the pnictide $Ba(Fe_{1-x}Co_x)_2As_2$. *Phys. Rev. B*, 80(14):140501, Oct 2009. doi: 10.1103/PhysRevB.80.140501.

[102] Shiliang Li, Clarina de la Cruz, Q. Huang, G. F. Chen, T.-L. Xia, J. L. Luo, N. L. Wang, and Pengcheng Dai. Structural and magnetic phase transitions in $Na_{1-\delta}FeAs$. *Phys. Rev. B*, 80(2):020504, Jul 2009. doi: 10.1103/PhysRevB.80.020504.

[103] S.J. Blundell, A.J. Steele, T. Lancaster, J.D. Wright, and F.L. Pratt. A Bayesian approach to magnetic moment determination using μSR. *Physics Procedia*, 30(0): 113–116, 2012. ISSN 1875–3892. doi: 10.1016/j.phpro.2012.04.052. 12th International Conference on Muon Spin Rotation, Relaxation and Resonance.

[104] D. K. Pratt, W. Tian, A. Kreyssig, J. L. Zarestky, S. Nandi, N. Ni, S. L. Bud'ko, P. C. Canfield, A. I. Goldman, and R. J. McQueeney. Coexistence of competing antiferromagnetic and superconducting phases in the underdoped $Ba(Fe_{0.953}Co_{0.047})_2As_2$ compound using x-ray and neutron scattering techniques. *Phys. Rev. Lett.*, 103(8):087001, Aug 2009. doi: 10.1103/PhysRevLett.103.087001.

[105] R. M. Fernandes, L. H. VanBebber, S. Bhattacharya, P. Chandra, V. Keppens, D. Mandrus, M. A. McGuire, B. C. Sales, A. S. Sefat, and J. Schmalian. Effects of nematic fluctuations on the elastic properties of iron arsenide superconductors. *Phys. Rev. Lett.*, 105(15):157003, Oct 2010. doi: 10.1103/PhysRevLett.105.157003.

[106] C. He, Y. Zhang, B. P. Xie, X. F. Wang, L. X. Yang, B. Zhou, F. Chen, M. Arita, K. Shimada, H. Namatame, M. Taniguchi, X. H. Chen, J. P. Hu, and D. L. Feng. Electronic-structure-driven magnetic and structure transitions in superconducting NaFeAs single crystals measured by angle-resolved photoemission spectroscopy. *Phys. Rev. Lett.*, 105:117002, Sep 2010. doi: 10.1103/PhysRevLett.105.117002.

[107] D. K. Pratt, M. G. Kim, A. Kreyssig, Y. B. Lee, G. S. Tucker, A. Thaler, W. Tian, J. L. Zarestky, S. L. Bud'ko, P. C. Canfield, B. N. Harmon, A. I. Goldman, and R. J. McQueeney. Incommensurate spin-density wave order in electron-doped $BaFe_2As_2$ superconductors. *Phys. Rev. Lett.*, 106:257001, Jun 2011. doi: 10.1103/PhysRevLett.106.257001.

[108] Huiqian Luo, Rui Zhang, Mark Laver, Zahra Yamani, Meng Wang, Xingye Lu, Miaoyin Wang, Yanchao Chen, Shiliang Li, Sung Chang, Jeffrey W. Lynn, and Pengcheng Dai. Coexistence and competition of the short-range incommensurate antiferromagnetic order with the superconducting state of $\mathrm{BaFe}_{2-x}\mathrm{Ni}_x\mathrm{As}_2$. *Phys. Rev. Lett.*, 108:247002, Jun 2012. doi: 10.1103/PhysRevLett.108.247002.

[109] R. Juza and K. Langer. Ternre Phosphide und Arsenide des Lithiums mit Eisen, Kobalt oder Chrom im Cu2Sb-Typ. *Zeitschrift fr anorganische und allgemeine Chemie*, 361(1-2):58–73, 1968. ISSN 1521-3749. doi: 10.1002/zaac.19683610107.

[110] X.C. Wang, Q.Q. Liu, Y.X. Lv, W.B. Gao, L.X. Yang, R.C. Yu, F.Y. Li, and C.Q. Jin. The superconductivity at 18 K in LiFeAs system. *Solid State Communications*, 148(11–12):538–540, 2008. ISSN 0038–1098. doi: 10.1016/j.ssc.2008.09.057.

[111] Masaki Mito, Michael J. Pitcher, Wilson Crichton, Gaston Garbarino, Peter J. Baker, Stephen J. Blundell, Paul Adamson, Dinah R. Parker, and Simon J. Clarke. Response of superconductivity and crystal structure of LiFeAs to hydrostatic pressure. *Journal of the American Chemical Society*, 131(8):2986–2992, 2009. doi: 10.1021/ja808914a. PMID: 19206468.

[112] Zhi Li, J. S. Tse, and C. Q. Jin. Crystal, spin, and electronic structure of the superconductor LiFeAs. *Phys. Rev. B*, 80:092503, Sep 2009. doi: 10.1103/PhysRevB.80.092503.

[113] Y.-F. Li and B.-G. Liu. Striped antiferromagnetic order and electronic properties of stoichiometric LiFeAs from first-principles calculations. *The European Physical Journal B*, 72(2):153–157, 2009. ISSN 1434-6028. doi: 10.1140/epjb/e2009-00338-5.

[114] Xinxin Zhang, Hui Wang, and Yanming Ma. First-principles study of the magnetic, structural and electronic properties of LiFeAs. *Journal of Physics: Condensed Matter*, 22(4):046006, 2010.

[115] A. E. Taylor, M. J. Pitcher, R. A. Ewings, T. G. Perring, S. J. Clarke, and A. T. Boothroyd. Antiferromagnetic spin fluctuations in LiFeAs observed by neutron scattering. *Phys. Rev. B*, 83:220514, Jun 2011. doi: 10.1103/PhysRevB.83.220514.

[116] N. Qureshi, P. Steffens, Y. Drees, A. C. Komarek, D. Lamago, Y. Sidis, L. Harnagea, H.-J. Grafe, S. Wurmehl, B. Büchner, and M. Braden. Inelastic neutron-scattering measurements of incommensurate magnetic excitations on superconducting LiFeAs single crystals. *Phys. Rev. Lett.*, 108:117001, Mar 2012. doi: 10.1103/PhysRevLett.108.117001.

[117] Meng Wang, X. C. Wang, D. L. Abernathy, L. W. Harriger, H. Q. Luo, Yang Zhao, J. W. Lynn, Q. Q. Liu, C. Q. Jin, Chen Fang, Jiangping Hu, and Pengcheng Dai. Antiferromagnetic spin excitations in single crystals of nonsuperconducting Li_{1-x}FeAs. *Phys. Rev. B*, 83:220515, Jun 2011. doi: 10.1103/PhysRevB.83.220515.

[118] A. K. Pramanik, L. Harnagea, C. Nacke, A. U. B. Wolter, S. Wurmehl, V. Kataev, and B. Büchner. Fishtail effect and vortex dynamics in LiFeAs single crystals. *Phys. Rev. B*, 83:094502, Mar 2011. doi: 10.1103/PhysRevB.83.094502.

[119] Torben Hänke, Steffen Sykora, Ronny Schlegel, Danny Baumann, Luminita Harnagea, Sabine Wurmehl, Maria Daghofer, Bernd Büchner, Jeroen van den Brink, and Christian Hess. Probing the unconventional superconducting state of LiFeAs by quasiparticle interference. *Phys. Rev. Lett.*, 108:127001, Mar 2012. doi: 10.1103/PhysRevLett.108.127001.

[120] S.-H. Baek, H.-J. Grafe, F. Hammerath, M. Fuchs, C. Rudisch, L. Harnagea, S. Aswartham, S. Wurmehl, J. Brink, and B. Bchner. ^{7}5As NMR-NQR study in superconducting LiFeAs. *The European Physical Journal B*, 85(5):1–10, 2012. ISSN 1434-6028. doi: 10.1140/epjb/e2012-30164-5.

[121] S-H Baek, L Harnagea, S Wurmehl, B Bchner, and H-J Grafe. Anomalous superconducting state in LiFeAs implied by the ^{7}5As knight shift measurement. *Journal of Physics: Condensed Matter*, 25(16):162204, 2013.

[122] G. Li, R. R. Urbano, P. Goswami, C. Tarantini, B. Lv, P. Kuhns, A. P. Reyes, C. W. Chu, and L. Balicas. Anomalous hysteresis as evidence for a magnetic-field-induced chiral superconducting state in LiFeAs. *Phys. Rev. B*, 87:024512, Jan 2013. doi: 10.1103/PhysRevB.87.024512.

[123] D. S. Inosov, J. S. White, D. V. Evtushinsky, I. V. Morozov, A. Cameron, U. Stockert, V. B. Zabolotnyy, T. K. Kim, A. A. Kordyuk, S. V. Borisenko, E. M. Forgan, R. Klingeler, J. T. Park, S. Wurmehl, A. N. Vasiliev, G. Behr, C. D. Dewhurst, and V. Hinkov. Weak superconducting pairing and a single isotropic energy gap in stoichiometric LiFeAs. *Phys. Rev. Lett.*, 104:187001, May 2010. doi: 10.1103/PhysRevLett.104.187001.

[124] A. A. Kordyuk, V. B. Zabolotnyy, D. V. Evtushinsky, T. K. Kim, I. V. Morozov, M. L. Kulić, R. Follath, G. Behr, B. Büchner, and S. V. Borisenko. Angle-resolved photoemission spectroscopy of superconducting LiFeAs: Evidence for strong electron-phonon coupling. *Phys. Rev. B*, 83:134513, Apr 2011. doi: 10.1103/PhysRevB.83.134513.

[125] P. M. R. Brydon, Maria Daghofer, Carsten Timm, and Jeroen van den Brink. Theory of magnetism and triplet superconductivity in LiFeAs. *Phys. Rev. B*, 83: 060501, Feb 2011. doi: 10.1103/PhysRevB.83.060501.

[126] Christian Platt, Ronny Thomale, and Werner Hanke. Superconducting state of the iron pnictide LiFeAs: A combined density-functional and functional-renormalization-group study. *Phys. Rev. B*, 84:235121, Dec 2011. doi: 10.1103/PhysRevB.84.235121.

[127] Y. J. Uemura, G. M. Luke, B. J. Sternlieb, J. H. Brewer, J. F. Carolan, W. N. Hardy, R. Kadono, J. R. Kempton, R. F. Kiefl, Kreitzman, S. R., P. Mulhern, T. M. Riseman, D. Ll. Williams, B. X. Yang, S. Uchida, H. Takagi, J. Gopalakrishnan, A. W. Sleight, M. A. Subramanian, C. L. Chien, M. Z. Cieplak, Gang Xiao, V. Y. Lee, B. W. Statt, C. E. Stronach, W. J. Kossler, and X. H. Yu. Universal correlations between T_c and $n_s/m*$ (carrier density over effective mass) in high-T_c cuprate superconductors. *Phys. Rev. Lett.*, 62(19):2317–2320, May 1989. doi: 10.1103/PhysRevLett.62.2317.

[128] Y. J. Uemura, L. P. Le, G. M. Luke, B. J. Sternlieb, W. D. Wu, J. H. Brewer, T. M. Riseman, C. L. Seaman, M. B. Maple, M. Ishikawa, D. G. Hinks, J. D. Jorgensen, G. Saito, and H. Yamochi. Basic similarities among cuprate, bismuthate, organic, chevrel-phase, and heavy-fermion superconductors shown by penetration-depth measurements. *Phys. Rev. Lett.*, 66(20):2665–2668, May 1991. doi: 10.1103/PhysRevLett.66.2665.

[129] Y.J. Uemura. Universal correlations, pseudo-gaps and condensation mechanisms in high-T_c superconductors. *Hyperfine Interactions*, 105(1-4):35–46, 1997. ISSN 0304-3843. doi: 10.1023/A:1012649826130.

[130] Y J Uemura. Condensation, excitation, pairing, and superfluid density in high-T_c superconductors: The magnetic resonance mode as a roton analogue and a possible spin-mediated pairing. *Journal of Physics: Condensed Matter*, 16(40): S4515, 2004.

[131] Y. J. Uemura, A. Keren, L. P. Le, G. M. Luke, W. D. Wu, Y. Kubo, T. Manako, Y. Shimakawa, M. Subramanian, J. L. Cobb, and J. T. Markert. Magnetic-field penetration depth in $Tl_2Ba_2CuO_{6+\delta}$ in the overdoped regime. *Nature*, 364:605–607, 1993.

[132] Ch. Niedermayer, C. Bernhard, U. Binninger, H. Glückler, J. L. Tallon, E. J. Ansaldo, and J. I. Budnick. Muon spin rotation study of the correlation between T_c and n_s/m^* in overdoped $Tl_2Ba_2CuO_{6+\delta}$. *Phys. Rev. Lett.*, 71:1764–1767, Sep 1993. doi: 10.1103/PhysRevLett.71.1764.

[133] V. J. Emery and S. A. Kivelson. Importance of phase fluctuations in superconductors with small superfluid density. *Nature*, 374:343–347, Mar 1995. doi: doi:10.1038/374434a0.

[134] Takafumi Sato, Seigo Souma, Kosuke Nakayama, Kensei Terashima, Katsuaki Sugawara, Takashi Takahashi, Yoichi Kamihara, Masahiro Hirano, and Hideo Hosono. Superconducting gap and pseudogap in iron-based layered superconductor La($O_{1-x}F_x$)FeAs. *Journal of the Physical Society of Japan*, 77(6):063708, 2008. doi: 10.1143/JPSJ.77.063708.

[135] Yong Seung Kwon, Jong Beom Hong, Yu Ran Jang, Hyun Jin Oh, Yun Young Song, Byeong Hun Min, Takeuya Iizuka, Shin ichi Kimura, A V Balatsky, and Yunkyu Bang. Evidence of a pseudogap for superconducting iron-pnictide $Ba_{0.6+\delta}K_{0.4-\delta}Fe_2As_2$ single crystals from optical conductivity measurements. *New Journal of Physics*, 14(6):063009, 2012.

[136] F. Massee, Y. K. Huang, J. Kaas, E. van Heumen, S. de Jong, R. Huisman, H. Luigjes, J. B. Goedkoop, and M. S. Golden. Pseudogap-less high-T_c superconductivity in $BaCo_xFe_{2-x}As_2$. *Europhysics Letters*, 92(5):57012, 2010.

[137] University of Florida. URL http://http://www.phys.ufl.edu/fermisurface/.

[138] S. V. Borisenko, V. B. Zabolotnyy, D. V. Evtushinsky, T. K. Kim, I. V. Morozov, A. N. Yaresko, A. A. Kordyuk, G. Behr, A. Vasiliev, R. Follath, and B. Buchner. Superconductivity without nesting in LiFeAs. *Phys. Rev. Lett.*, 105(6):067002, Aug 2010. doi: 10.1103/PhysRevLett.105.067002.

[139] D. V. Evtushinsky, D. S. Inosov, V. B. Zabolotnyy, A. Koitzsch, M. Knupfer, B. Büchner, M. S. Viazovska, G. L. Sun, V. Hinkov, A. V. Boris, C. T. Lin, B. Keimer, A. Varykhalov, A. A. Kordyuk, and S. V. Borisenko. Momentum dependence of the superconducting gap in $Ba_{1-x}K_xFe_2As_2$. *Phys. Rev. B*, 79: 054517, Feb 2009. doi: 10.1103/PhysRevB.79.054517.

[140] H. Shishido, A. F. Bangura, A. I. Coldea, S. Tonegawa, K. Hashimoto, S. Kasahara, P. M. C. Rourke, H. Ikeda, T. Terashima, R. Settai, Y. Ōnuki, D. Vignolles, C. Proust, B. Vignolle, A. McCollam, Y. Matsuda, T. Shibauchi, and A. Carrington. Evolution of the fermi surface of $BaFe_2(As_{1-x}P_x)_2$ on entering the superconducting dome. *Phys. Rev. Lett.*, 104:057008, Feb 2010. doi: 10.1103/PhysRevLett.104.057008.

[141] Z. Li, Y. Ooe, X.-C. Wang, Q.-Q. Liu, C.-Q. Jin, M. Ichioka, and G. q. Zheng. ^{75}As NQR and NMR studies of superconductivity and electron correlations in iron

arsenide LiFeAs. *Journal of the Physical Society of Japan*, 79(8):083702, 2010. doi: 10.1143/JPSJ.79.083702.

[142] M. A. Tanatar, J.-Ph. Reid, S. René de Cotret, N. Doiron-Leyraud, F. Laliberté, E. Hassinger, J. Chang, H. Kim, K. Cho, Yoo Jang Song, Yong Seung Kwon, R. Prozorov, and Louis Taillefer. Isotropic three-dimensional gap in the iron arsenide superconductor LiFeAs from directional heat transport measurements. *Phys. Rev. B*, 84:054507, Aug 2011. doi: 10.1103/PhysRevB.84.054507.

[143] H. Kim, M. A. Tanatar, Yoo Jang Song, Yong Seung Kwon, and R. Prozorov. Nodeless two-gap superconducting state in single crystals of the stoichiometric iron pnictide LiFeAs. *Phys. Rev. B*, 83:100502, Mar 2011. doi: 10.1103/PhysRevB.83.100502.

[144] J. S. Kim, Seunghyun Khim, H. J. Kim, M. J. Eom, J. M. Law, R. K. Kremer, Ji Hoon Shim, and Kee Hoon Kim. Electron-hole asymmetry in Co- and Mn-doped srfe$_2$as$_2$. *Phys. Rev. B*, 82:024510, Jul 2010. doi: 10.1103/PhysRevB.82.024510.

[145] Athena S. Sefat, David J. Singh, Lindsay H. VanBebber, Yurij Mozharivskyj, Michael A. McGuire, Rongying Jin, Brian C. Sales, Veerle Keppens, and David Mandrus. Absence of superconductivity in hole-doped $Ba(Fe_{1-x}Cr_x)_2As_2$ single crystals. *Phys. Rev. B*, 79:224524, Jun 2009. doi: 10.1103/PhysRevB.79.224524.

[146] J. D. Wright, M. J. Pitcher, W. Trevelyan-Thomas, T. Lancaster, P. J. Baker, F. L. Pratt, S. J. Clarke, and S. J. Blundell. Magnetic fluctuations and spin freezing in non-superconducting LiFeAs derivatives. *Phys. Rev. B*, 88:060401, Aug 2013. doi: 10.1103/PhysRevB.88.060401.

[147] A. D. Hillier, J. Quintanilla, and R. Cywinski. Evidence for time-reversal symmetry breaking in the noncentrosymmetric superconductor $LaNiC_2$. *Phys. Rev. Lett.*, 102:117007, Mar 2009. doi: 10.1103/PhysRevLett.102.117007.

[148] G. M. Luke, Y. Fudamoto, K. M. Kojima, M. I. Larkin, J. Merrin, B. Nachumi, Y. J. Uemura, Y. Maeno, Z. Q. Mao, Y. Mori, H. Nakamura, and M. Sigrist. Time-reversal symmetry-breaking superconductivity in Sr_2RuO_4. *Nature*, 394:558–561, Aug 1998.

[149] Grant Bunker. *Introduction to XAFS.* Cambridge University Press, 2010.

[150] A. Thaler, N. Ni, A. Kracher, J. Q. Yan, S. L. Bud'ko, and P. C. Canfield. Physical and magnetic properties of $Ba(Fe_{1-x}Ru_x)_2As_2$ single crystals. *Phys. Rev. B*, 82: 014534, Jul 2010. doi: 10.1103/PhysRevB.82.014534.

[151] N. Ni, M. E. Tillman, J.-Q. Yan, A. Kracher, S. T. Hannahs, S. L. Bud'ko, and P. C. Canfield. Effects of Co substitution on thermodynamic and transport properties and anisotropic H_{c2} in Ba(Fe$_{1-x}$Co$_x$)$_2$As$_2$ single crystals. *Phys. Rev. B*, 78: 214515, Dec 2008. doi: 10.1103/PhysRevB.78.214515.

[152] Satoru Masaki, Hisashi Kotegawa, Yudai Hara, Hideki Tou, Keizo Murata, Yoshikazu Mizuguchi, and Yoshihiko Takano. Precise pressure dependence of the superconducting transition temperature of FeSe: Resistivity and ^{77}Se-NMR study. *Journal of the Physical Society of Japan*, 78(6):063704, 2009. doi: 10.1143/JPSJ.78.063704.

[153] E. Colombier, S. L. Bud'ko, N. Ni, and P. C. Canfield. Complete pressure-dependent phase diagrams for SrFe$_2$As$_2$ and BaFe$_2$As$_2$. *Phys. Rev. B*, 79:224518, Jun 2009. doi: 10.1103/PhysRevB.79.224518.

[154] T. M. McQueen, Q. Huang, V. Ksenofontov, C. Felser, Q. Xu, H. Zandbergen, Y. S. Hor, J. Allred, A. J. Williams, D. Qu, J. Checkelsky, N. P. Ong, and R. J. Cava. Extreme sensitivity of superconductivity to stoichiometry in Fe$_{1+\delta}$Se. *Phys. Rev. B*, 79:014522, Jan 2009. doi: 10.1103/PhysRevB.79.014522.

[155] C.W. Chu, F. Chen, M. Gooch, A.M. Guloy, B. Lorenz, B. Lv, K. Sasmal, Z.J. Tang, J.H. Tapp, and Y.Y. Xue. The synthesis and characterization of LiFeAs and NaFeAs. *Physica C: Superconductivity*, 469(9–12):326–331, 2009. ISSN 0921-4534. doi: 10.1016/j.physc.2009.03.016.

[156] P. Jeglič, A. Potočnik, M. Klanjšek, M. Bobnar, M. Jagodič, K. Koch, H. Rosner, S. Margadonna, B. Lv, A. M. Guloy, and D. Arčon. ^{75}as nuclear magnetic resonance study of antiferromagnetic fluctuations in the normal state of LiFeAs. *Phys. Rev. B*, 81:140511, Apr 2010. doi: 10.1103/PhysRevB.81.140511.

[157] L. Ma, J. Zhang, G. F. Chen, and Weiqiang Yu. NMR evidence of strongly correlated superconductivity in LiFeAs: Tuning toward a spin-density-wave ordering. *Phys. Rev. B*, 82:180501, Nov 2010. doi: 10.1103/PhysRevB.82.180501.

[158] K. Cho, H. Kim, M. A. Tanatar, Y. J. Song, Y. S. Kwon, W. A. Coniglio, C. C. Agosta, A. Gurevich, and R. Prozorov. Anisotropic upper critical field and possible Fulde-Ferrel-Larkin-Ovchinnikov state in the stoichiometric pnictide superconductor LiFeAs. *Phys. Rev. B*, 83:060502, Feb 2011. doi: 10.1103/PhysRevB.83.060502.

[159] Y. J. Um, J. T. Park, B. H. Min, Y. J. Song, Y. S. Kwon, B. Keimer, and M. Le Tacon. Raman scattering study of the lattice dynamics of superconducting LiFeAs. *Phys. Rev. B*, 85:012501, Jan 2012. doi: 10.1103/PhysRevB.85.012501.

[160] H. Okamoto. The FeSe (iron-selenium) system. *Journal of Phase Equilibria*, 12 (3):383–389, 1991. ISSN 1054-9714. doi: 10.1007/BF02649932.

[161] M. H. Fang, H. M. Pham, B. Qian, T. J. Liu, E. K. Vehstedt, Y. Liu, L. Spinu, and Z. Q. Mao. Superconductivity close to magnetic instability in $\mathrm{Fe(Se_{1-x}Te_x)_{0.82}}$. *Phys. Rev. B*, 78:224503, Dec 2008. doi: 10.1103/PhysRevB.78.224503.

[162] Yoshikazu Mizuguchi, Fumiaki Tomioka, Shunsuke Tsuda, Takahide Yamaguchi, and Yoshihiko Takano. Substitution effects on FeSe superconductor. *Journal of the Physical Society of Japan*, 78(7):074712, 2009. doi: 10.1143/JPSJ.78.074712.

[163] Jiangang Guo, Shifeng Jin, Gang Wang, Shunchong Wang, Kaixing Zhu, Tingting Zhou, Meng He, and Xiaolong Chen. Superconductivity in the iron selenide $\mathrm{K_xFe_2Se_2}$ $(0 \leq x \leq 1.0)$. *Phys. Rev. B*, 82:180520, Nov 2010. doi: 10.1103/PhysRevB.82.180520.

[164] A. F. Wang, J. J. Ying, Y. J. Yan, R. H. Liu, X. G. Luo, Z. Y. Li, X. F. Wang, M. Zhang, G. J. Ye, P. Cheng, Z. J. Xiang, and X. H. Chen. Superconductivity at 32 K in single-crystalline $\mathrm{Rb_xFe_{2-y}Se_2}$. *Phys. Rev. B*, 83:060512, Feb 2011. doi: 10.1103/PhysRevB.83.060512.

[165] A. Krzton-Maziopa, Z. Shermadini, E. Pomjakushina, V. Pomjakushin, M. Bendele, A. Amato, R. Khasanov, H. Luetkens, and K. Conder. Synthesis and crystal growth of $\mathrm{Cs_{0.8}(FeSe_{0.98})_2}$: A new iron-based superconductor with $T_c = 27$ K. *Journal of Physics: Condensed Matter*, 23(5):052203, 2011.

[166] J. Bacsa, A. Y. Ganin, Y. Takabayashi, K. E. Christensen, K. Prassides, M. J. Rosseinsky, and J. B. Claridge. Cation vacancy order in the $\mathrm{K_{0.8+x}Fe_{1.6-y}Se_2}$ system: Five-fold cell expansion accommodates 20% tetrahedral vacancies. *Chem. Sci.*, 2:1054–1058, 2011. doi: 10.1039/C1SC00070E.

[167] Bao Wei, Huang Qing-Zhen, Chen Gen-Fu, M. A. Green, Wang Du-Ming, He Jun-Bao, and Qiu Yi-Ming. A novel large moment antiferromagnetic order in $\mathrm{K_{0.8}Fe_{1.6}Se_2}$ superconductor. *Chinese Physics Letters*, 28(8):086104, 2011.

[168] Y. Texier, J. Deisenhofer, V. Tsurkan, A. Loidl, D. S. Inosov, G. Friemel, and J. Bobroff. NMR study in the iron-selenide $\mathrm{Rb_{0.74}Fe_{1.6}Se_2}$: Determination of the superconducting phase as iron vacancy-free $\mathrm{Rb_{0.3}Fe_2Se_2}$. *Phys. Rev. Lett.*, 108: 237002, Jun 2012. doi: 10.1103/PhysRevLett.108.237002.

[169] T. P. Ying, X. L. Chen, G. Wang, S. F. Jin, T. T. Zhou, X. F. Lai, H. Zhang, and W. Y. Wang. Observation of superconductivity at 30–46 K in $\mathrm{A_xFe_2Se_2}$ (A = Li, Na, Ba, Sr, Ca, Yb, and Eu). *Sci. Rep.*, 2(426), 2012. doi: 10.1038/srep00426.

[170] A. Carrington and F. Manzano. Magnetic penetration depth of MgB_2. *Physica C: Superconductivity*, 385(1–2):205–214, 2003. ISSN 0921-4534. doi: http://dx.doi.org/10.1016/S0921-4534(02)02319-5.

[171] A Krzton-Maziopa, E. V. Pomjakushina, V. Yu Pomjakushin, F. von Rohr, A. Schilling, and K. Conder. Synthesis of a new alkali metalorganic solvent intercalated iron selenide superconductor with $T_c \simeq 45\,K$. *Journal of Physics: Condensed Matter*, 24(38):382202, 2012.

[172] P. J. Baker, I. Franke, F. L. Pratt, T. Lancaster, D. Prabhakaran, W. Hayes, and S. J. Blundell. Probing magnetic order in $LiMPO_4$ (M = Ni, Co, Fe) and lithium diffusion in Li_xFePO_4. *Phys. Rev. B*, 84:174403, Nov 2011. doi: 10.1103/PhysRevB.84.174403.

[173] Z. Shermadini, A. Krzton-Maziopa, M. Bendele, R. Khasanov, H. Luetkens, K. Conder, E. Pomjakushina, S. Weyeneth, V. Pomjakushin, O. Bossen, and A. Amato. Coexistence of magnetism and superconductivity in the iron-based compound $Cs_{0.8}(FeSe_{0.98})_2$. *Phys. Rev. Lett.*, 106:117602, Mar 2011. doi: 10.1103/PhysRevLett.106.117602.

[174] M.K. Kubo and K. Nishiyama. Positive muons in condensed phase ammonia. *Journal of Radioanalytical and Nuclear Chemistry*, 255(1):175–178, 2003. ISSN 0236-5731. doi: 10.1023/A:1022212705537.

[175] Yiming Qiu, Wei Bao, Y. Zhao, Collin Broholm, V. Stanev, Z. Tesanovic, Y. C. Gasparovic, S. Chang, Jin Hu, Bin Qian, Minghu Fang, and Zhiqiang Mao. Spin gap and resonance at the nesting wave vector in superconducting $FeSe_{0.4}Te_{0.6}$. *Phys. Rev. Lett.*, 103:067008, Aug 2009. doi: 10.1103/PhysRevLett.103.067008.

[176] T. A. Maier and D. J. Scalapino. Theory of neutron scattering as a probe of the superconducting gap in the iron pnictides. *Phys. Rev. B*, 78:020514, Jul 2008. doi: 10.1103/PhysRevB.78.020514.

[177] T. A. Maier, S. Graser, D. J. Scalapino, and P. Hirschfeld. Neutron scattering resonance and the iron-pnictide superconducting gap. *Phys. Rev. B*, 79:134520, Apr 2009. doi: 10.1103/PhysRevB.79.134520.

[178] M. M. Korshunov and I. Eremin. Theory of magnetic excitations in iron-based layered superconductors. *Phys. Rev. B*, 78:140509, Oct 2008. doi: 10.1103/PhysRevB.78.140509.

[179] J. T. Park, G. Friemel, Yuan Li, J.-H. Kim, V. Tsurkan, J. Deisenhofer, H.-A. Krug von Nidda, A. Loidl, A. Ivanov, B. Keimer, and D. S. Inosov. Magnetic resonant mode in the low-energy spin-excitation spectrum of superconducting $Rb_2Fe_4Se_5$ single crystals. *Phys. Rev. Lett.*, 107:177005, Oct 2011. doi: 10.1103/PhysRevLett.107.177005.

[180] A. E. Taylor, R. A. Ewings, T. G. Perring, J. S. White, P. Babkevich, A. Krzton-Maziopa, E. Pomjakushina, K. Conder, and A. T. Boothroyd. Spin-wave excitations and superconducting resonant mode in $Cs_xFe_{2-y}Se_2$. *Phys. Rev. B*, 86: 094528, Sep 2012. doi: 10.1103/PhysRevB.86.094528.

[181] G. Friemel, J. T. Park, T. A. Maier, V. Tsurkan, Yuan Li, J. Deisenhofer, H.-A. Krug von Nidda, A. Loidl, A. Ivanov, B. Keimer, and D. S. Inosov. Reciprocal-space structure and dispersion of the magnetic resonant mode in the superconducting phase of $Rb_xFe_{2-y}Se_2$ single crystals. *Phys. Rev. B*, 85:140511, Apr 2012. doi: 10.1103/PhysRevB.85.140511.

[182] A. E. Taylor, S. J. Sedlmaier, S. J. Cassidy, E. A. Goremychkin, R. A. Ewings, T. G. Perring, S. J. Clarke, and A. T. Boothroyd. Spin fluctuations away from (π,0) in the superconducting phase of molecular-intercalated FeSe. *ArXiv e-prints*, May 2013.

[183] D. S. Inosov, J. T. Park, A. Charnukha, Yuan Li, A. V. Boris, B. Keimer, and V. Hinkov. Crossover from weak to strong pairing in unconventional superconductors. *Phys. Rev. B*, 83:214520, Jun 2011. doi: 10.1103/PhysRevB.83.214520.

[184] K. Sasmal, B. Lv, Z. Tang, F. Y. Wei, Y. Y. Xue, A. M. Guloy, and C. W. Chu. Lower critical field, anisotropy, and two-gap features of lifeas. *Phys. Rev. B*, 81: 144512, Apr 2010. doi: 10.1103/PhysRevB.81.144512.

[185] Hyun-Sook Lee, Marek Bartkowiak, Jae-Hyun Park, Jae-Yeap Lee, Ju-Young Kim, Nak-Heon Sung, B. K. Cho, Chang-Uk Jung, Jun Sung Kim, and Hu-Jong Lee. Effects of two gaps and paramagnetic pair breaking on the upper critical field of $SmFeAsO_{0.85}$ and $SmFeAsO_{0.8}F_{0.2}$ single crystals. *Phys. Rev. B*, 80:144512, Oct 2009. doi: 10.1103/PhysRevB.80.144512.

[186] Mika Kano, Yoshimitsu Kohama, David Graf, Fedor Balakirev, Athena S. Sefat, Michael A. Mcguire, Brian C. Sales, David Mandrus, and Stanley W. Tozer. Anisotropy of the upper critical field in a Co-doped $BaFe_2As_2$ single crystal. *Journal of the Physical Society of Japan*, 78(8):084719, 2009. doi: 10.1143/JPSJ.78.084719.

[187] S. Ghannadzadeh, J. D. Wright, P. A. Goddard, and S. J. Blundell. (*in preparation*).

[188] N. R. Werthamer, E. Helfand, and P. C. Hohenberg. Temperature and purity dependence of the superconducting critical field, H_{c2}. III. Electron spin and spin-orbit effects. *Phys. Rev.*, 147:295–302, Jul 1966. doi: 10.1103/PhysRev.147.295.

[189] Z.-H. Liu, P. Richard, K. Nakayama, G.-F. Chen, S. Dong, J.-B. He, D.-M. Wang, T.-L. Xia, K. Umezawa, T. Kawahara, S. Souma, T. Sato, T. Takahashi, T. Qian, Yaobo Huang, Nan Xu, Yingbo Shi, H. Ding, and S.-C. Wang. Unconventional superconducting gap in $NaFe_{0.95}Co_{0.05}As$ observed by angle-resolved photoemission spectroscopy. *Phys. Rev. B*, 84:064519, Aug 2011. doi: 10.1103/PhysRevB.84.064519. URL `http://link.aps.org/doi/10.1103/PhysRevB.84.064519`.

[190] Lan Luan, Thomas M. Lippman, Clifford W. Hicks, Julie A. Bert, Ophir M. Auslaender, Jiun-Haw Chu, James G. Analytis, Ian R. Fisher, and Kathryn A. Moler. Local measurement of the superfluid density in the pnictide superconductor $Ba(Fe_{1-x}Co_x)_2As_2$ across the superconducting dome. *Phys. Rev. Lett.*, 106:067001, Feb 2011. doi: 10.1103/PhysRevLett.106.067001.

[191] A. F. Wang, Z. J. Xiang, J. J. Ying, Y. J. Yan, P. Cheng, G. J. Ye, X. G. Luo, and X. H. Chen. Pressure effects on the superconducting properties of single-crystalline Co-doped NaFeAs. *New Journal of Physics*, 14(11):113043, 2012.

[192] Roberto De Renzi, Pietro Bonf, Marcello Mazzani, Samuele Sanna, Giacomo Prando, Pietro Carretta, Rustem Khasanov, Alex Amato, Hubertus Luetkens, Markus Bendele, Fabio Bernardini, Sandro Massidda, Andrea Palenzona, Matteo Tropeano, and Maurizio Vignolo. Effect of external pressure on the magnetic properties of LnFeAsO (Ln = La, Ce, Pr, Sm). *Superconductor Science and Technology*, 25(8):084009, 2012.

[193] D. Graf, R. Stillwell, T. P. Murphy, J.-H. Park, E. C. Palm, P. Schlottmann, R. D. McDonald, J. G. Analytis, I. R. Fisher, and S. W. Tozer. Pressure dependence of the $BaFe_2As_2$ fermi surface within the spin density wave state. *Phys. Rev. B*, 85:134503, Apr 2012. doi: 10.1103/PhysRevB.85.134503.

[194] J. Singleton. *Band Theory and Electronic Properties of Solids*. Oxford Master Series in Condensed Matter Physics. OUP Oxford, 2001. ISBN 9780198506447.

[195] G. S. Pawley. Unit-cell refinement from powder diffraction scans. *Journal of Applied Crystallography*, 14(6):357–361, Dec 1981. doi: 10.1107/S0021889881009618.

[196] D. V. Evtushinsky, D. S. Inosov, V. B. Zabolotnyy, M. S. Viazovska, R. Khasanov, A. Amato, H.-H. Klauss, H. Luetkens, Ch. Niedermayer, G. L. Sun, V. Hinkov,

C. T. Lin, A. Varykhalov, A. Koitzsch, M. Knupfer, B. Büchner, A. A. Kordyuk, and S. V. Borisenko. Momentum-resolved superconducting gap in the bulk of $Ba_{1x}K_xFe_2As_2$ from combined ARPES and μSR measurements. *New Journal of Physics*, 11(5):055069, 2009.